RADIOGENIC ISOTOPES AND LATE PLEISTOCENE CLIMATE CHANGES IN THE CENTRAL EQUATORIAL PACIFIC

A Dissertation

by

MARIA ALEJANDRA REIMI SIPALA

Submitted to the Office of Graduate and Professional Studies of
Texas A&M University
in partial fulfillment of the requirements for the degree of

DOCTOR OF PHILOSOPHY

Chair of Committee, Franco Marcantonio
Committee Members, Christina Belanger
Ethan Grossman
Deborah Thomas
Head of Department, Michael Pope

May 2018

Major Subject: Geology

ABSTRACT

This work focuses on reconstructing changes in atmospheric and bottom water circulation in the Central Equatorial Pacific (CEP) through the last 150 000 years, to examine how atmospheric and oceanic system respond to changes in global temperature in glacial-interglacial timescales. This work is part of a larger conversation in paleoclimate and paleoceanography that investigates the link between changes in northern hemisphere insolation and ocean-atmosphere interactions in the Southern Ocean. These focus in these relationship from two different perspectives. Section 2 and 3 examine dust provenance to reconstruct changes in tropical hydroclimate, in particular the changes in the position of the Intertropical Convergence Zone (ITCZ) the zone of maximum precipitation.

I study a 7° north-south transect in the CEP at 160° W, across the annual latitudinal range of the modern ITCZ. This dust provenance work relies on measuring the changes in lead (Pb) and neodymium (Nd) isotopes in the chemically isolated dust fraction of marine sediments. First, I look at ITCZ changes from the last 30 kyr to the mid-Holocene, in order to examine the difference between glacial and interglacial conditions. I suggest that the ITCZ reached its southernmost position during glacial times. I identify this shift in the ITCZ by noting an increase in dust of Asian provenance in the more southern cores. During warmer global climate periods, the ITCZ migrates farther north. I also examine the changes in the ITCZ across the penultimate deglaciations by examining samples from 110 to 150 kyr. I found that the southernmost position of the ITCZ occurred during the peak deglaciation (between 136 and 131 kyr), with a subsequent interglacial movement of more than 7° north.

I also investigate the changes in deep-water circulation in the CEP over the last two glacial cycles (from the mid-Holocene to 150 kyr ago) using the Nd isotopic composition of fossil fish debris as a water mass tracer. I discovered an interesting response of Nd in fish debris to low oxygen conditions, a critical contribution to the field, as it complicates the paleoceanographic reconstructions that have been published using Nd isotopes as a conservative tracer. By taking a holistic multi-proxy approach, I was able to constrain the sources that affect Nd in fish debris and improve our current understanding of the respired carbon pool that is argued to be ventilated by the Southern Ocean during deglaciations.

DEDICATION

To my family and to the Caracas of my childhood.

Para mi familia y para la Caracas de mi niñez

ACKNOWLEDGEMENTS

This work would not have been possible without the continued support and encouragement from my advisor, Dr. Franco Marcantonio. I am grateful beyond words that I have had Franco in my life for the past five years. He has been an outstanding mentor, a brilliant scientist and a kind friend. He has help me become a better scientist and a more resilient person.

I am also grateful to my dissertation committee, Dr. Ethan Grossman, Dr. Debbie Thomas and Dr. Christina Belanger, for their guidance and support, and to Dr. Mike Tice who provided feedback through my proposal and preliminary exams. My deepest thanks also to Luz Romero, who has been indispensable in the lab and a true friend, and to Dr. Brent Miller for all the help wrangling the TIMS.

I'm also grateful to the College of Geoscience and the G&G faculty and staff for their support, and for the financial support of the ConocoPhillips fellowship my first year at Texas A&M and the Pipes Scholarship in 2017-2018.

My higher education journey started with the incredible generosity of philanthropists and optimists across the world, and I would be incredibly remiss to not express gratitude to all of the benefactors who have made this long journey possible: Avemundo, United World College Costa Rica, the Grieg Foundation, the Davis Foundation, and Washington and Lee University.

My most sincere thanks also to the Washington and Lee Geology Department, they inspired my love of rocks and Earth systems. I am especially indebted to Dr. Lisa Greer for picking my enthusiasm in the first row of class and convincing me to switch majors and spend more time outdoors; to Dr. Paul Low for letting me set up experiments in the back of the minerology classroom, helping me write my undergraduate thesis and letting me tell jokes during

my defense; to Dr. Jeff Rahl for teaching me to not be overwhelmed by the big picture, to Chris Connors for his kind and welcoming leadership; and to David Harbor for teaching me to think outside of the box and leading me through Iceland with unending enthusiasm and no regard for dinner-time. I would also like to thank Dr. Jessica Morrison for teaching me to love lab time and not being too hard on my when I messed up and Dr. Peter Burns for inviting me to his lab despite having no previous experience or obvious qualifications.

My time at Texas A&M would have been much different without the love and support of my friends and the community of caring people that took me in. There have been countless people who have stood by me, fed me, listened to me, and found little and big ways to support me during the past five years. Through the hardest times of my life, my friends have been there to lift me up, and I would like to give my sincerest thanks to Grecia Lopez, Matthew Loveley, Caitlin Kelly, Claire McKinley, Monica Barbery, Maria Antonieta Gutierrez, Lauren Holder, Angie Van Boening, Michelle Chrpa, Maya Morales McDevitt, Luz Zarate, Ali Snell, Tanner Mills, Ryan Elmore, Rachel Scudder, Ann Le, and Scout Whitaker.

Lastly, I would also like to thank my family for their love, support and patience. I am especially grateful to my siblings, who supported me from afar when I needed them the most and to my parents, who modelled strength and determinations and inspired me to be a better person.

CONTRIBUTORS AND FUNDING SOURCES

Contributors

This work was supervised by a dissertation committee consisting of Professor Franco Marcantonio (advisor) and Professors Ethan Grossman and Christina Belanger of the Department of Geology and Geophysics and Professor Deborah Thomas of the Department of Oceanography.

This work was designed by Maya Reimi and Franco Marcantonio. Marine sediment samples were provided by the Lamont-Doherty Core Repository. Sample preparation was done in part by students from Geology 489: Team Research in Geochemistry and Thinh Nguyen. Maya Reimi preformed all sample digestions and all detrital Nd and Pb isotope analyses, Nd isotopes measured on fish debris for core ML1208-17PC, as well as the new U-Th presented for cores ML1208-20BB and 28BB (section 3) with the help of Luz Romero. This dissertation has greatly benefited from comments by all committee members.

The oxygen isotope data provided in section 3 was provided by Jean Lynch-Stieglitz at Georgia Tech. The analysis for section 3 written by Maya Reimi and Franco Marcantonio, with additional comments and edits from Jean Lynch-Stieglitz, Allison Jacobel, Jerry McManus and Gisela Winckler at Columbia University and the Lamont-Doherty Earth Observatory.

The Ba concentration data analyzed in section 4 was measured by Seyi Oliyani-Sholenke with the help of Luz Romero. Fish debris samples for core 17PC were picked with the help of Rafael Adriano, John Tye and Emily Whitaker. The core-top fish debris samples were picked and Nd isotopes measured by Stella Woodard at Texas A&M University.

Funding Sources

This research was funded in part by NSF grant OCE-1502889 to Franco Marcantonio and a graduate research fellowship from ConocoPhillips to Maya Reimi. Additional financial support was provided by Franco Marcantonio through the Jane and R. Ken Williams Chair in Ocean Drilling Science, Technology, and Education.

TABLE OF CONTENTS

Page

LIST OF FIGURES

Page

LIST OF TABLES

Page

1. INTRODUCTION

1.1 Rationale and Background

The purpose of this research is to investigate some of the changes in atmospheric and ocean circulation that affect the Central Equatorial Pacific (CEP), in particular as archived in marine sediments near the Line Islands. This work includes changes in the Late Pleistocene and the Holocene extending to the past 150 000 years. Through that time period we focus on times of rapid climate change with the aim to gain a better understanding of the mechanism that affect global climate change.

The past 150 000 years encompass the last two climate transitions from full glacial to interglacial conditions, known as climate terminations. These critical moments include Termination II, the coldest termination during the Quaternary (Lisiecki and Raymo, 2005), the last Glacial Maximum, the deglacial to Holocene transition, and the Holocene thermal maximum.

This research is primary concern with how the CEP reflects the links between northern hemisphere cooling and the Southern Ocean. In section 2 and 3 we will expand on whether the Intertropical Convergence Zone (ITCZ) migrates in response to global temperature variations, and in particular whether during periods of strong northern hemisphere cooling there is a southward shift in the ITCZ which is responsible for agitating the surface waters in the Southern Ocean and plays a role in triggering peak interglacial conditions. (e.g. Chiang and Bitz, 2005). Section 4 will continue to look at the role of the Southern Ocean in global climate transitions by examining changes in deep-water conditions throughout the last two glacial cycles.

1.2 The role of the Intertropical Convergence Zone

The Intertropical Convergence Zone (ITCZ) is a key component of the atmospheric circulation; it lies just north of the equator and is a zone of permanent low atmospheric pressure. As part of the wider circulation system it corresponds to the ascending arm of the Hadley circulation, which controls the spatial distribution of tropical precipitation as well as the atmospheric meridional heat transport (Waliser and Gautier, 1993). Otherwise known as the thermal equator or the meteorological equator, the ITCZ represents the zone of convergence of the trade winds leading to increased convection, cloudiness, and precipitation (Waliser and Gautier, 1993, Philander et al., 1996).

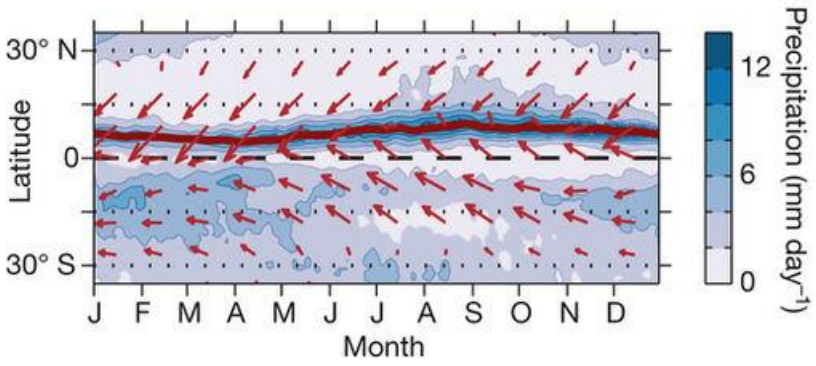

Figure 1.1 Position of the ITCZ over the eastern Pacific. The position of the ITCZ as a function of time of year in the Pacific Ocean is marked by the red line, which reflect the precipitation maximum. Mean precipitation is shown in the color scale surface winds in vectors. Reprinted from Schneider et al. (2014).

The zonal average position of the ITCZ over the eastern Pacific (Fig. 1.1) is at 9°N during the boreal summer and 2°N during the boreal winter (Fig, 1,1) (Schneider et al., 2014). But locally at 160°W, the ITCZ is more narrowly defined, with an annual variability between 7°N and 5°N (Adler et al., 2003). In this study (sections 2 and 3), the location of the most northern core (MGL1208-37BB) coincides with the northern extent of the ITCZ in boreal summer (at

7°N) and our most southern core (MGL1208-17PC) is below the boreal winter position of the ITCZ (at 0.5°N). The ITCZ behaves quite differently over land surfaces and adjacent oceans. Over the Indian Ocean, the migration of the ITCZ causes the rainfall variation of the South Asian monsoon and the total range of the position of the ITCZ varies annually over 28 degrees (between 20°N and 8°S) (Gadgil, 2003). The meridional overturning circulation of the Hadley cells straddles half of the area of the globe (Lu et al., 2007), including some of the most populous places on Earth. Climate variability within the Hadley system can affect the lives of billions of people by changing the amount and location of precipitation (Diaz and Bradley, 2004). The migration of the ITCZ is correlated with changes in atmospheric heat distribution, which can trigger global changes in surface winds and precipitation acting like a catalyst to global atmospheric circulation changes (Seager et al., 2005). As the ITCZ is an expression of the global thermal balance (Schneider et al., 2014), the paleo position of the ITCZ can be used to monitor the changes in the interhemispheric thermal gradient (Chiang and Friedman, 2012).

Convection associated with the ITCZ can also impact regional climate. The ITCZ is a region of increased cloudiness and precipitation that follows the relatively warmer location of the sea surface temperatures (Tomas and Holton, 1999). Thus, the location of the ITCZ is associated with a region of high water vapor. A contraction in the meridional extent in tropical convection (i.e. a diminished ITCZ) can cool the tropics as a whole through a simple reduction of humidity in the non-convective regions. Similarly an expansion in the convective region associated with the ITCZ can cause a regional increase in tropical temperature by increasing the overall tropical humidity (Ivanochko et al., 2005).

1.2.1 The ITCZ and Paleoclimate

Paleo-ITCZ reconstructions can provide insights into the degree of asymmetry in past climate changes. ITCZ position, and thus the position of maximum tropical precipitation, influences the hydrological cycle and global wind fields. The location of the ITCZ can have overarching ramifications throughout Earth's atmospheric circulation system including influencing a) greenhouse gas concentrations, b) poleward heat and moisture transport, c) the strength of ENSO, d) thermohaline circulation sensitivity, e) marine productivity, and f) terrestrial aridity (Koutavas and Lynch-Stieglitz, 2004). However, current general circulation models often have large degrees of uncertainty associated with atmospheric changes due to asymmetric climate forcings (Li and Xie, 2014), and uncertainties in the mechanism that cause ITCZ shifts (Clark et al., 2018). Studying paleo-ITCZ as it responds to rapid climate change can lead to a better understanding about the mechanism that cause ITCZ migrations.

Independent lines of evidence – modelling (Chiang and Bitz, 2005, Broccoli et al., 2006) and paleoclimate observations (Peterson et al., 2000, Koutavas and Lynch-Stieglitz, 2004) - have shown a link between northern hemisphere cooling and a southward shift of the ITCZ. However, the mechanism of this connection is not properly understood.

Paleo-records indicate that the annual mean position of the ITCZ migrates towards the hemisphere experiencing relative warming, which is consistent with the migration of the ITCZ seasonally (Schneider et al., 2014). The migration towards the relatively warming hemisphere is a feature of the ITCZ which seems relatively consistent in both models (Broccoli et al., 2006, Donohoe et al., 2013) and paleodata (McGee et al., 2014, Haug et al., 2001, Sachs et al., 2009, Koutavas and Lynch-Stieglitz, 2004) .

Most studies of the paleo position of the ITCZ are based on proxy records that either reflect changes in the location of maximum precipitation (Wang et al., 2001, Peterson and Haug, 2006, Fleitmann et al., 2003) or sea surface temperature (Koutavas and Lynch-Stieglitz, 2004). Paleo precipitation records are often land based. For example, Wang et al.'s (2001) outstanding record from the Hulu Cave speleothems, in eastern China, correlates the predicted changes in precipitation with a migration of the ITCZ. Off the coast of Venezuela, Huag et al. (2001) used changes titanium concentrations in the Cariaco Basin sediments in the Pleistocene as a proxy for increased riverine discharge, itself a symptom of an ITCZ migration. However, measured changes in precipitation can be due to a shift in the position of the ITCZ or to a change in its rainfall intensity within the ITCZ (Schneider et al., 2014). Furthermore, land-based proxies are subpar analogues for mean-annual changes in the position of the ITCZ, as the ITCZ shows a larger range of variability closer to continental masses (Schneider et al., 2014). In contrast, the ITCZ near the Line Islands exhibits a narrow range as described above.

Studies of the past 30000 years from different regions tend to agree with a more southern ITCZ during glacial periods, showing reduced precipitation, weakened summer monsoon and increased winter trade winds in the Northern hemisphere, and increased precipitation in central South America and Northern Australia (McGee et al., 2014 and references therein). However, the magnitude of the shift of the ITCZ tends to be poorly constrained and proxy based estimates vary widely –from a 7° N change between the LGM and the Holocene in the Atlantic Ocean (Arbuszewski et al., 2013) to estimates of a 5° change in the position of the ITCZ during the past 400 years (Sachs et al., 2009). McGee et al. (2014), however, modeled the position of the ITCZ based on SST gradient, and suggested only a very small change (less than 1°) in the ITCZ position globally between the LGM and the Holocene. They attributed this discrepancy to a

decoupling of precipitation records from the ITCZ position or to zonal heterogeneity. The latter allows for very large local changes in the ITCZ along some longitudes, as long as changes at other longitudes are near zero.

Few studies have looked at the changes in the mean position of the ITCZ in the Pacific Ocean. And within the Pacific, most studies have focused on the variability over the Eastern Equatorial Pacific, based on changes in the sea surface temperature gradient. These studies, as summarized by Koutavas and Lynch-Stieglitz (2004), have found that there is a link between increased Northern Hemisphere cooling and a southward displacement of the ITCZ at the EEP during the Last Glacial Maximum.

More Pacific Ocean records of paleo-ITCZ position are needed in order to solve the discrepancy between models and observations. Ideal records would depend solely in atmospheric conditions, unlike SST records which are also affected by surface currents.

1.2.1 Using Dust as a Proxy for Wind

Given the challenges in reconstructing paleo-atmospheric conditions using SST, we must explore the use of more direct surface wind proxies. The only archive of paleo-winds is dust (Prospero, 1981, Rea, 1994). Hence, atmospheric circulation reconstructions must look at which characteristics of dust change through time and space that reflect changes in atmospheric circulation. Eolian dust accumulated in pelagic sediments provides direct information about paleoatmospheric circulation, and both the intensity of wind and the availability of dust in past climates (Rea et al., 1985).

Atmospheric dust plays a dual role as both a driver and a recorder of climate change. Dust concentrations impact the Earth's radiative balance by affecting the scattering and absorption of radiation, both incoming and outgoing (Tegen and Schepanski, 2009, Mahowald et

al., 2006). Increases in dust may cause either cooling or warming depending on dust concentration, vertical distribution and mineralogy, and other independent variables such as albedo and temperature of the underlying surface (Harrison et al., 2001). Atmospheric dust is also linked to the increased removal of carbon dioxide from the atmospheric system in episodes of large oceanic productivity and export that can be caused by atmospheric dust iron seeding (Jickells et al., 2005).

Atmospheric dust is mostly sourced from the world's deserts and arid areas, mostly located around the tropics, in the high pressure regions in the Hadley cell system (Prospero, 1981). The geochemical composition of atmospheric dust depends on the geochemical composition of the original source area, as eolian deposits are the result of the weathering of rocks and soils. However, finding an adequate tracer of dust requires finding a tracer that is always transported with dust and is characteristic of a specific source area, thus allowing differentiation between sources (Grousset and Biscaye, 2005).

Traditional methods of tracing dust provenance involved using differences in grain-size distributions, but this can be affected by transport dynamics, i.e., variable distance, altitude, and wind strength (Rea, 1994). Many elemental tracers, remain relatively unaltered through transport, but are often not very useful in adequately distinguishing source areas, or experience large-scale fractionation either through transport of during post depositional dissolution (Sholkovitz et al., 1993). Similarly, the mineralogical composition of dust particles can be used as a tracer, but these are often not substantially different globally, or the differences cannot be measured accurately enough to distinguish source regions (Biscaye, 1965).

Changes in the lead and neodymium isotopic signature of the dust fraction of marine sediments reflect the original heterogeneity of the source rocks from where the dust was eroded

(Grousset and Biscaye, 2005). These signatures are not impacted by transport and are relatively constant in the fine fraction of dust (Grousset and Biscaye, 2005). If dust provenance changes through time indicate changes in the hemispheric origin of dust, we can interpret these changes as a change in the position of the ITCZ (Xie and Marcantonio, 2012), see section 2 and 3.

1.3 Changes in deep-water conditions

Another way to look at the teleconnection between northern hemisphere cooling and the changes in the conditions at the CEP is through the changes in deep-water conditions in glacial-interglacial scales. Section 4 examines the changes in the fossil fish debris neodymium (Nd) isotope record at the CEP over the last 150 000 years. It explores the deep-water mechanism that affect the Nd isotope record and how this reflects back to global climate, as well as local effects on the authigenic Nd isotope record.

In modern seawater, the Nd isotope composition of deep-water reflects changes in deep-water mixing and the heterogenous inputs of Nd into the ocean (van de Flierdt et al., 2016). Modern overturning ocean circulation is driven by the sinking of cold saline water masses at high latitudes. This thermohaline circulation causes the ocean to act as a "great ocean conveyor" Broecker (1991). Most of the world's deepwater formation occurs in the north Atlantic (as North Atlantic Deep Water, NADW) and in the Southern Ocean (Antarctic Bottom Water, AABW). NADW and AABW mix in the circumpolar system and flow northward in the Pacific in the form of Circumpolar Deepwater (CDW) (Ganachaud and Wunsch, 2000). CDW splits into an upper and lower portion which flow equatorward in the Pacific eventually advecting in the form of North Pacific Deep Water (NPDW) (Kawabe and Fujio, 2010).

NPDW is the dominant bottom water at 3000 m in the Line Islands archipelago, characterize by lower salinity than CDW but a lower dissolved oxygen (Garcia et al., 2014,

Zweng et al., 2013). Section 4 explores whether the Nd isotope of fossil fish debris reflect changes in the CDW to NPDW mixing due to changes in climate or whether there are other effects that alter the NPDW signal recorded in Nd fossil fish debris and how this related to Southern Ocean ventilation changes and the triggering of climate terminations.

1.3.1 Southern Ocean ventilation and Climate Terminations

The CO_2 changes recorded in ice cores have shown that there is a rapid release of CO_2 in the transitions between glacial and interglacial climate, with cyclical drawdown and release of CO_2 in orbital timescale (Barnola et al., 1987, Augustin et al., 2004). Changes in Southern Ocean ventilation have been long hypothesized to be key drivers of this cycle, since the Southern Ocean is the largest reservoir of carbon readily available to exchange with the atmosphere (Sigman and Boyle, 2001, Sigman et al., 2010).

During glacial times, Antarctic water stratification lead to a limited supply of CO_2 and nutrients from the Southern Ocean to the rest of the Pacific (Sigman and Boyle, 2001). This isolation meant that CO_2 is increasingly sequestered in the Southern Ocean until a shock to the stratification leads to increase ventilation and triggers a climate termination (Broecker and Denton, 1989). Changes in the equatorial Pacific have been suggested as a major component of carbon drawdown and release, with the implication that the ITCZ plays a role in agitating the Sothern ocean surface waters (Anderson et al., 2009).

More recent work has suggest that the equatorial Pacific also plays a role in the storage of respired carbon during glacial stages, as changes in authigenic uranium have been reasons to occur when increased Southern Ocean CO_2 changes the oxygenation levels in the equatorial Pacific (Jacobel et al., 2017, Loveley et al., 2017). By investigating the Nd isotopic composition in fossil fish debris in the central equatorial pacific, we hope to better understand the degree of

ocean stratification during the deglacial and shed light on the mechanisms that are in play during a climate termination.

1.4 Radiogenic Isotopes

1.4.1 Nd, Pb isotope systems

Samarium and Neodymium are both rare-earth elements (REEs) that occur in many rock-forming silicates, phosphate, and carbonate minerals. ^{147}Sm is a long-lived radioactive isotope that decays to ^{143}Nd via alpha decay, with a constant of $6.54x10^{-12}$ yr^{-1}, a 106 Gyr half-life *(Lugmair, 1974)*. The abundances of Sm/Nd are often reported solely based on the isotopic composition of Nd, using the radiogenic ^{143}Nd to the non-radiogenic ^{144}Nd ratio ($^{143}Nd/^{144}Nd$). This ratio slowly increases as a function of time because of the decay of ^{147}Sm into ^{143}Nd, but based on the half-life of ^{147}Sm this increase is negligible in modern timescales.

As light REEs, the chemistry of Sm and Nd is very similar, both have a charge of +3 and similar ionic radii. The concentration of Sm and Nd in igneous rocks ranges from less than 1-8 ppm Sm and 45 ppm Nd in granitic rocks. Even though the ionic radii difference between Nd and Sm is small (Nd^{+3} = 1.08 Å; Sm^{+3} = 1.04 Å), Nd is preferentially concentrated in the liquid phase during partial melting of silicates, whereas Sm remains in the residual solids. Therefore basalt magmas have lower Sm/Nd ratios than their source rock, and continental rocks are enriched in Nd relative to Sm (Jacobsen and Wasserburg, 1980).

During nebula condensation, Sm and Nd rapidly partition into solids at high temperatures. Thus, Whole Earth Sm/Nd and the isotopic composition of Nd can be obtained from that of chondritic meteorites. Specifically, the mantle evolution of Nd isotopes can be described using CHUR evolution, "chondritic uniform reservoir" (DePaolo and Wasserburg, 1976a). The accepted values for the present day ratio of $^{147}Sm/^{143}Nd$ is 0.1966, the $^{143}Nd/^{144}Nd$ is

0.512638 (Jacobsen and Wasserburg, 1980). Nd isotopic values are expressed in deviations on the order of parts per 10^4 from bulk Earth values or ε_{Nd} values. The mathematical expression that defines ε_{Nd} with respect to Bulk Earth (CHUR) is:

$$\varepsilon_{Nd} = \left\{ \left[\frac{\left({}^{143}Nd/_{144}Nd \right)_{Sample}}{\left({}^{143}Nd/_{144}Nd \right)_{Bulk\ Earth}} - 1 \right] \right\} \times 10^4$$

(Equation 1)

Igneous materials have varying ε_{Nd} ratios based on their age and composition -degree of differentiation from the mantle (Figure 1.2). An undifferentiated mantle rock would have Bulk Earth Nd-isotope ratios and its $\varepsilon_{Nd} = 0$. An old continental crust rock has negative ε_{Nd} values; while a depleted-mantle rock (like Mid-Ocean Ridge Basalts) would have evolved from a higher Sm/Nd ratio and has positive ε_{Nd} values.

Like in the Nd isotope system, variations in Pb isotope ratios reflect heterogeneity in crustal rocks, due to the different behavior of the parent isotopes and daughter products in melt/solid and the age of the sediment. However, the Pb isotope system relies in three different isotope ratios. Radiogenic lead (Pb) isotopes –^{208}Pb, ^{207}Pb, ^{206}Pb– are the final product of the decay series of long-lived uranium (U) and thorium (Th) isotopes. ^{206}Pb is a product of the decay of ^{238}U, with a half-life of 4.47 Ga, while ^{207}Pb is a daughter of ^{235}U with a half-life of 704 M, and ^{208}Pb is the product of the decay of ^{232}Th with a half-life of 14.05 Ga (Faure and Mensing, 2005). In this work Pb isotopes are expressed in ratios of radiogenic Pb over the non-radiogenic Pb isotope ^{204}Pb. Higher values are thus more enriched in radiogenic Pb and lower values are less radiogenic.

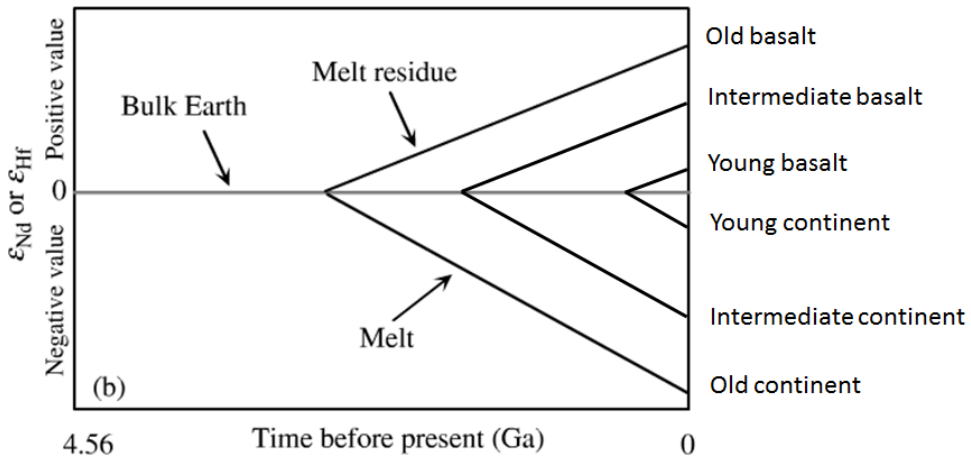

Figure 1.2 Systematics of Nd evolution from Bulk Earth (CHUR). Nd is more incompatible during mantle melting (more likely to go into a partial melt of mantle rocks) than Sm, As a result the continental crust has a lower Sm/Nd ratio and thus more negative εNd values. Young continental crust has isotope ratios similar to the mantle, and the older the continental terrain the more negative the εNd. Modified from Faure and Mensing (2005).

In short timescales, Pb isotopes acquire an "industrial contamination" signature. As there is an increased in environmental lead with a unique Pb-ore isotope signature which causes modern anthropogenic disturbances of radiogenic signatures (Grousset and Biscaye, 2005). However, even the youngest sample used in the work (mid-Holocene age) is much older than the post-industrial area, and we do not expect any significant anthropogenic Pb contamination.

1.5 Nd and Pb isotopes as paleoclimate tools in the CEP

Using a combination of different isotopic systems has been shown to be useful in differentiating between different dust source areas, because the heterogeneities in exposed rocks within drainage basins are magnified in eolian dust (Grousset and Biscaye, 2005). The isotopic composition of the radiogenic isotopes of Nd ($^{143}Nd/^{144}Nd$ isotope ratio) and Pb ($^{206}Pb/^{204}Pb$, $^{207}Pb/^{204}Pb$, and $^{208}Pb/^{204}Pb$ isotope ratios) vary significantly across the globe, based on both lithology (crustal- versus mantle-derived rocks) and age of sediments (DePaolo and Wasserburg, 1976b). As a consequence, the Nd and Pb isotopic composition of dust reflects the continental

heterogeneity of the rocks from where it is weathered, and many studies have investigated the sources of eolian fluxes to the oceans, and the North Pacific in particular (e.g. Grousset et al., 1988, Biscaye et al., 1997, Jones et al., 2000, Nakai et al., 1993).

Studies using dust provenance in the EEP Pacific have found conflicting information regarding the magnitude of the migration of the ITCZ. A Nd isotope study of dust provenance by Xie and Marcantonio (2012) did not find evidence for a significant displacement of the ITCZ between the LGM and the Holocene, contradicting the SST data for a similar location (e.g. Koutavas and Lynch-Stieglitz, 2003). However, a similar study in the EEP using both Pb and Nd isotope ratios by Pichat et al. (2014) did associate changes in the dust provenance in the EEP to a latitudinal displacement of the South Westerlies – with a southward retreat of the South Westerlies during southern hemisphere warming. This might be concurrent with a southward migration of the ITCZ.

For this study marine sediment samples were collected from several core sites in the Line Islands ridge. They represent a 7° north-south transect across the modern position of the ITCZ near 160° W. In section 2 we reconstruct the changes across three sites and in section 3 we used two additional cores between 3° N and 0° N for a total of five cores. We show that relying on both Nd and Pb isotopes can successfully differentiate the dust sources to the CEP over the last two deglaciations. Additionally, in section 3 we show a simple mixing model which can be used to quantify the relative sources of dust to the CEP or the absolute sources when combined with dust fluxes proxies. We also evaluate how the changes in dust flux over time and space can reflect changes in the paleo-position of the ITCZ.

As the ITCZ acts as a strong barrier to inter-hemispheric dust transport, we can interpret changes in hemispheric provenance as displacement of the ITCZ. Near the Line Islands region,

the ITCZ is well defined (Tomas and Webster, 1997, Philander et al., 1996) far from possible continental influences (Tomas and Holton, 1999) and outside of the main region affected by El Niño-Southern Oscillation (ENSO) (Dai and Wigley, 2000), therefore dust provenance changes reflect annual mean changes and not changes in the strength of seasonality or ENSO.

In section 4, we use Nd isotope ratios in fossil fish debris to investigate the role of deep water circulation changes associated with changing bottom water oxygen conditions in the CEP over the past 125 kyrs. We find that through most of the study period the bottom water Nd isotope signal is consistent with that for modern-day North Pacific Deep Water. However, several points across the record show a high level of radiogenic Nd enrichment. This enrichment is not consistent with changes in water mass mixing nor with a particle-driven mechanism related to increased dust fluxes or ocean productivity. We conclude that the Nd enrichment is caused by increased dissolution of ambient volcanic ash at times consistent with the timing of low oxygen in the bottom waters, as suggested by high authigenic uranium concentrations at various sites throughout the Equatorial Pacific. These times during which low-oxygen waters persist, are linked to the timing of reduced Southern Ocean ventilation, and a more isolated deep ocean.

1.6 References

ADLER, R. F., HUFFMAN, G. J., CHANG, A., FERRARO, R., XIE, P.-P., JANOWIAK, J., RUDOLF, B., SCHNEIDER, U., CURTIS, S. & BOLVIN, D. 2003. The version-2 global precipitation climatology project (GPCP) monthly precipitation analysis (1979-present). *Journal of hydrometeorology,* 4.

ANDERSON, R. F., ALI, S., BRADTMILLER, L. I., NIELSEN, S. H. H., FLEISHER, M. Q., ANDERSON, B. E. & BURCKLE, L. H. 2009. Wind-Driven Upwelling in the Southern Ocean and the Deglacial Rise in Atmospheric CO_2. *Science,* 323**,** 1443-1448.

ARBUSZEWSKI, J. A., CLÉROUX, C., BRADTMILLER, L. & MIX, A. 2013. Meridional shifts of the Atlantic intertropical convergence zone since the Last Glacial Maximum. *Nature Geoscience*.

AUGUSTIN, L., BARBANTE, C., BARNES, P. R., BARNOLA, J. M., BIGLER, M., CASTELLANO, E., CATTANI, O., CHAPPELLAZ, J., DAHL-JENSEN, D. &

DELMONTE, B. 2004. Eight glacial cycles from an Antarctic ice core. *Nature,* 429**,** 623-628.

BARNOLA, J.-M., RAYNAUD, D., KOROTKEVICH, Y. S. & LORIUS, C. 1987. Vostok ice core provides 160,000-year record of atmospheric CO2. *Nature,* 329**,** 408.

BISCAYE, P. E. 1965. Mineralogy and sedimentation of recent deep-sea clay in the Atlantic Ocean and adjacent seas and oceans. *Geological Society of America Bulletin,* 76**,** 803-832.

BISCAYE, P. E., GROUSSET, F. E., REVEL, M., GAAST, S. V. D., ZIELINSKI, G. A., VAARS, A. & KUKLA, G. 1997. Asian provenance of glacial dust (stage 2) in the Greenland Ice Sheet Project 2 Ice Core, Summit, Greenland. *Journal of Geophysical Research,* 102.

BROCCOLI, A. J., DAHL, K. A. & STOUFFER, R. J. 2006. Response of the ITCZ to Northern Hemisphere cooling. *Geophysical Research Letters,* 33.

BROECKER, W. S. 1991. The great ocean conveyor. *Oceanography,* 4**,** 79-89.

BROECKER, W. S. & DENTON, G. H. 1989. The role of ocean-atmosphere reorganizations in glacial cycles. *Geochimica et Cosmochimica Acta,* 53.

CHIANG, J. C. & BITZ, C. M. 2005. Influence of high latitude ice cover on the marine Intertropical Convergence Zone. *Climate Dynamics,* 25**,** 477-496.

CHIANG, J. C. & FRIEDMAN, A. R. 2012. Extratropical Cooling, Interhemispheric Thermal Gradients, and Tropical Climate Change. *Annual Review of Earth and Planetary Sciences,* 40**,** 383-412.

CLARK, S. K., MING, Y., HELD, I. M. & PHILLIPPS, P. J. 2018. The role of the water vapor feedback in the ITCZ response to hemispherically asymmetric forcings. *Journal of Climate,* 0**,** null.

DAI, A. & WIGLEY, T. M. L. 2000. Global patterns of ENSO-induced precipitation. *Geophysical Research Letters*.

DEPAOLO, D. J. & WASSERBURG, G. J. 1976a. Inferences about magma sources and mantle structure from variations of 143 Nd/ 144 Nd. *Geophysical Research Letters,* 3.

DEPAOLO, D. J. & WASSERBURG, G. J. 1976b. Nd isotopic variations and petrogenetic models. *Geophysical Research …*.

DIAZ, H. F. & BRADLEY, R. S. 2004. *The Hadley Circulation: Present, Past, and Future*, Springer.

DONOHOE, A., MARSHALL, J., FERREIRA, D. & MCGEE, D. 2013. The relationship between ITCZ location and cross-equatorial atmospheric heat transport: From the seasonal cycle to the Last Glacial Maximum. *Journal of Climate*, 26.

FAURE, G. & MENSING, T. M. 2005. *Isotopes: principles and applications*, Wiley Hoboken, NJ.

FLEITMANN, D., BURNS, S. J., MUDELSEE, M., NEFF, U. & KRAMERS, J. 2003. Holocene forcing of the Indian monsoon recorded in a stalagmite from southern Oman. *Science*.

GADGIL, S. 2003. T HE I NDIAN M ONSOON AND I TS V ARIABILITY. *Annual Review of Earth and Planetary Sciences,* 31**,** 429-467.

GANACHAUD, A. & WUNSCH, C. 2000. Improved estimates of global ocean circulation, heat transport and mixing from hydrographic data. *Nature,* 408**,** 453-457.

GARCIA, H. E., LOCARNINI, R. A., BOYER, T. P., ANTONOV, J. I., BARANOVA, O. K., ZWENG, M. M., REAGAN, J. R. & JOHNSON, D. R. 2014. World Ocean Atlas 2013, Volume 3: Dissolved Oxygen, Apparent Oxygen Utilization, and Oxygen Saturation. *In:* LEVITUS, S. & MISHONOV, A. (eds.) *NOAA Atlas NESDIS.*

GROUSSET, F. E. & BISCAYE, P. E. 2005. Tracing dust sources and transport patterns using Sr, Nd and Pb isotopes. *Chemical Geology*.

GROUSSET, F. E., BISCAYE, P. E., ZINDLER, A., PROSPERO, J. & CHESTER, R. 1988. Neodymium isotopes as tracers in marine sediments and aerosols: North Atlantic. *Earth and Planetary Science Letters,* 87**,** 367378.

HARRISON, S. P., KOHFELD, K. E., ROELANDT, C. & CLAQUIN, T. 2001. The role of dust in climate changes today, at the last glacial maximum and in the future. *Earth-Science Reviews,* 54.

HAUG, G. H., HUGHEN, K. A., SIGMAN, D. M., PETERSON, L. C. & RÖHL, U. 2001. Southward migration of the intertropical convergence zone through the Holocene. *Science (New York, N.Y.),* 293**,** 1304-1308.

IVANOCHKO, T. S., GANESHRAM, R. S. & BRUMMER, G. J. A. 2005. Variations in tropical convection as an amplifier of global climate change at the millennial scale. *Earth and Planetary …*.

JACOBEL, A. W., WINCKLER, G., MCMANUS, J. & ANDERSON, R. 2017. Repeated storage of respired carbon in the equatorial Pacific Ocean over the last three glacial cycles. *Nature communications,* 8**,** 1727.

JACOBSEN, S. B. & WASSERBURG, G. 1980. Sm-Nd isotopic evolution of chondrites. *Earth and Planetary Science Letters,* 50**,** 139-155.

JICKELLS, T. D., AN, Z. S., ANDERSEN, K. K., BAKER, A. R., BERGAMETTI, G., BROOKS, N., CAO, J. J., BOYD, P. W., DUCE, R. A., HUNTER, K. A., KAWAHATA, H., KUBILAY, N., LISS, P. S., MAHOWALD, N., PROSPERO, J., RIDGWELL, A. J., TEGEN, I. & TORRES, R. 2005. Global iron connections between desert dust, ocean biogeochemistry, and climate. *Science*.

JONES, C. E., HALLIDAY, A. N., REA, D. K. & OWEN, R. M. 2000. Eolian inputs of lead to the North Pacific. *Eolian inputs of lead to the North Pacific*.

KAWABE, M. & FUJIO, S. 2010. Pacific ocean circulation based on observation. *Journal of Oceanography*, 66**,** 389-403.

KOUTAVAS, A. & LYNCH-STIEGLITZ, J. 2004. Variability of the marine ITCZ over the eastern Pacific during the past 30,000 years. *The Hadley Circulation: Present, Past and Future*. Springer.

KOUTAVAS, A. & LYNCH-STIEGLITZ, J. 2003. Glacial-interglacial dynamics of the eastern equatorial Pacific cold tongue-Intertropical Convergence Zone system reconstructed from oxygen isotope records. *Paleoceanography,* 18.

LI, G. & XIE, S.-P. 2014. Tropical Biases in CMIP5 Multimodel Ensemble: The Excessive Equatorial Pacific Cold Tongue and Double ITCZ Problems. *Journal of Climate,* 27**,** 1765-1780.

LISIECKI, L. E. & RAYMO, M. E. 2005. A Pliocene-Pleistocene stack of 57 globally distributed benthic δ18O records. *Paleoceanography,* 20.

LOVELEY, M., MARCANTONIO, F., WISLER, M., HERTZBERG, J., SCHMIDT, M. & LYLE, M. 2017. Millenial-scale iron fertilization of the eastern equatorial Pacific over the past 100,000 years. *Nature Geoscience*.

LU, J., VECCHI, G. A. & REICHLER, T. 2007. Expansion of the Hadley cell under global warming. *Geophysical Research Letters,* 34**,** n/a-n/a.

LUGMAIR, G. 1974. Sm-Nd ages: a new dating method. *Meteoritics,* 9**,** 369.

MAHOWALD, N. M., YOSHIOKA, M., COLLINS, W. D., CONLEY, A. J., FILLMORE, D. W. & COLEMAN, D. B. 2006. Climate response and radiative forcing from mineral aerosols during the last glacial maximum, pre-industrial, current and doubled-carbon dioxide climates. *Geophysical Research Letters,* 33.

MCGEE, D., DONOHOE, A., MARSHALL, J. & FERREIRA, D. 2014. Changes in ITCZ location and cross-equatorial heat transport at the Last Glacial Maximum, Heinrich Stadial 1, and the mid-Holocene. *Earth and Planetary Science …*.

NAKAI, S. I., HALLIDAY, A. N. & REA, D. K. 1993. Provenance of dust in the Pacific Ocean. *Earth and Planetary Science Letters,* 119.

PETERSON, L. C. & HAUG, G. H. 2006. Variability in the mean latitude of the Atlantic Intertropical Convergence Zone as recorded by riverine input of sediments to the Cariaco Basin (Venezuela). *Palaeogeography*.

PETERSON, L. C., HAUG, G. H., HUGHEN, K. A. & RÖHL, U. 2000. Rapid changes in the hydrologic cycle of the tropical Atlantic during the last glacial. *Science,* 290**,** 1947-1951.

PHILANDER, S. G. H., GU, D., LAMBERT, G. & LI, T. 1996. Why the ITCZ is mostly north of the equator. *Journal of …*.

PICHAT, S., ABOUCHAMI, W. & GALER, S. 2014. Lead isotopes in the Eastern Equatorial Pacific record Quaternary migration of the South Westerlies. *Earth and Planetary Science Letters,* 388.

PROSPERO, J. M. 1981. Eolian transport to the World Ocean. *In:* EMILIANI, C. (ed.) *The Oceanic Lithosphere, The Sea.* New York: Wiley Interscience.

REA, D. K. 1994. The paleoclimatic record provided by eolian deposition in the deep sea: The geologic history of wind. *Reviews of Geophysics,* 32.

REA, D. K., LEINEN, M. & JANECEK, T. R. 1985. Geologic approach to the long-term history of atmospheric circulation. *Science*.

SACHS, J. P., SACHSE, D., SMITTENBERG, R. H. & ZHANG, Z. 2009. Southward movement of the Pacific intertropical convergence zone AD 1400–1850. *Nature …*.

SCHNEIDER, T., BISCHOFF, T. & HAUG, G. H. 2014. Migrations and dynamics of the intertropical convergence zone. *Nature,* 513.

SEAGER, R., KUSHNIR, Y., HERWEIJER, C. & NAIK, N. 2005. Modeling of Tropical Forcing of Persistent Droughts and Pluvials over Western North America: 1856-2000*. *Journal of …*.

SHOLKOVITZ, E. R., CHURCH, T. M. & ARIMOTO, R. 1993. Rare earth element composition of precipitation, precipitation particles, and aerosols. *Journal of Geophysical Research: Atmospheres (1984–2012),* 98**,** 20587-20599.

SIGMAN, D. M. & BOYLE, E. A. 2001. Palaeoceanography: Antarctic stratification and glacial CO 2. *Nature,* 412**,** 606.

SIGMAN, D. M., HAIN, M. P. & HAUG, G. H. 2010. The polar ocean and glacial cycles in atmospheric CO2 concentration. *Nature,* 466**,** 47.

TEGEN, I. & SCHEPANSKI, K. 2009. The global distribution of mineral dust. *The global distribution of mineral dust*.

TOMAS, R. A. & HOLTON, J. R. 1999. The influence of cross-equatorial pressure gradients on the location of near-equatorial convection. *Quarterly Journal of the …*.

TOMAS, R. A. & WEBSTER, P. J. 1997. The role of inertial instability in determining the location and strength of near-equatorial convection. *Quarterly Journal of the Royal …*.

VAN DE FLIERDT, T., GRIFFITHS, A. M., LAMBELET, M., LITTLE, S. H., STICHEL, T. & WILSON, D. J. 2016. Neodymium in the oceans: a global database, a regional comparison and implications for palaeoceanographic research. *Philosophical Transactions of the Royal Society A: Mathematical, Physical and Engineering Sciences*, 374.

WALISER, D. E. & GAUTIER, C. 1993. A satellite-derived climatology of the ITCZ. *Journal of Climate*.

WANG, Y. J., CHENG, H., EDWARDS, R. L., AN, Z. S. & WU, J. Y. 2001. A high-resolution absolute-dated late Pleistocene monsoon record from Hulu Cave, China. *Science*.

XIE, R. C. & MARCANTONIO, F. 2012. Deglacial dust provenance changes in the Eastern Equatorial Pacific and implications for ITCZ movement. *Earth and Planetary Science Letters*.

ZWENG, M. M., REAGAN, J. R., ANTONOV, J. I., LOCARNINI, R. A., MISHONOV, A. V., BOYER, T. P., GARCIA, H. E., BARANOVA, O. K., JOHNSON, D. R., SEIDOV, D. & BIDDLE, M. M. 2013. World Ocean Atlas 2013, Volume 2: Salinity. *In:* LEVITUS, S. & MISHONOV, A. (eds.) *NOAA Atlas NESDIS*.

2. CONSTRAINTS ON THE MAGNITUDE OF THE DEGLACIAL MIGRATION OF THE ITCZ IN THE CENTRAL EQUATORIAL PACIFIC OCEAN[1]

2.1 Introduction

The Intertropical Convergence Zone (ITCZ) is a key component of the Hadley Cell circulation; in the Pacific Ocean it lies north of the Equator. The ITCZ is a zone of low atmospheric pressure dominated by convective storm systems where trade winds converge (Philander et al., 1996). Given that dust is effectively scavenged by precipitation, the precipitation maximum associated with the ITCZ acts as a strong barrier to inter-hemispheric dust transport (Rea, 1994). ITCZ paleo-latitude can be used to monitor the extent of the interhemispheric thermal gradient (Chiang and Friedman, 2012), and provides insights into the degree of inter-hemispheric thermal asymmetry in the past. Studying ITCZ paleo-latitude and the sensitivity of the ITCZ to global temperature changes is critical since half the global population resides in tropical hydroclimates which are dominated by the Hadley cell circulation and impacted by changes in tropical precipitation (Schneider et al., 2014).

Paleo-records indicate that the paleo-ITCZ migrates towards the hemisphere experiencing relative warming (Schneider et al., 2014). The development of an interhemispheric thermal gradient is part of a teleconnection of extra-tropical cooling in the tropical rainfall climate (Chiang and Friedman, 2012). Independent lines of evidence – modelling (Chiang and Bitz, 2005, Broccoli et al., 2006) and paleoclimate observations (Koutavas and Lynch-Stieglitz, 2004)

[1] Reprinted from *Earth and Planetary Science Letters*, 453, Maria A. Reimi and Franco Marcantonio, Constraints on the magnitude of the deglacial migration of the ITCZ in the Central Equatorial Pacific Ocean, 1-8, 2016, with permission from Elsevier.

– have shown a link between northern hemisphere cooling and a global southward shift of the ITCZ. However, the mechanism of this connection is not properly understood.

Over the Pacific Ocean the location of the ITCZ varies seasonally between 9°N during the boreal summer and 2°N during the boreal winter (Schneider et al., 2014). Locally, at 160°W, the ITCZ is more narrowly defined, with an annual range between 8°N and 5°N (Adler et al., 2003). The modern location of the zonally averaged annual maximum precipitation more closely follows the maximum precipitation during July-August-September (Adler et al., 2003), when the ITCZ is near its northernmost position. Only a few studies have looked at the changes in the mean position of the ITCZ in the Pacific Ocean, with most focused on the Eastern Equatorial Pacific (EEP). These studies, as summarized by Koutavas and Lynch-Stieglitz (2004), have found that there is a link between increased Northern Hemisphere cooling and a southward displacement of the ITCZ at the EEP during the Last Glacial Maximum.

The direction of migration of the average position of the ITCZ, i.e., a southward shift during Northern hemisphere cooling, seems relatively consistent in both models (Broccoli et al., 2006, Donohoe et al., 2013) and paleodata (McGee et al., 2014, Haug et al., 2001, Koutavas and Lynch-Stieglitz, 2004). The magnitude of the variations, however, can vary substantially. McGee et al. (2014) calculated a less than 1° shift in ITCZ position over glacial-interglacial transitions, while a more recent study using ^{230}Th fluxes, found as much as a 7° shift at Heinrich stage 11 during the penultimate deglaciation within the Central Equatorial Pacific (CEP) (Jacobel et al., 2016).

Continental mineral dust which accumulates in pelagic sediments provides the only direct information about paleo-atmospheric circulation (Rea, 1994). This dust is mostly sourced from the world's deserts and arid areas, which are located at lower latitudes in the descending

branch of the Hadley circulation (Grousset and Biscaye, 2005). In addition to being a recorder of climate change, atmospheric dust directly impacts the Earth's radiative balance by affecting the scattering and absorption of solar radiation (Mahowald et al., 2006).

A combination of different radiogenic isotopic signatures can be used to differentiate between dust source areas because the heterogeneities in exposed rocks can be highlighted in eolian material (Grousset and Biscaye, 2005). Radiogenic isotopic compositions of dust may vary with particle size, but are not altered during transport. Specifically, although Sr isotope ratios can be biased within varying grain size fractions of dust, the isotope ratios of Nd and Pb do not seem to be sensitive to grain size fractionation processes (Grousset and Biscaye, 2005). The $^{143}Nd/^{144}Nd$ and $^{206}Pb/^{204}Pb$, $^{207}Pb/^{204}Pb$, and $^{208}Pb/^{204}Pb$ isotope ratios vary significantly in dust source areas based on crustal lithology and age (see summary in Grousset and Biscaye, 2005).

The purpose of this research is to investigate the possible changes in the position of the Intertropical Convergence Zone (ITCZ) in response to climate during the past 30 kyr. This time period includes critical moments in Earth's recent climate history including the Last Glacial Maximum (LGM), the deglacial to Holocene transition, and the Holocene thermal maximum. Here, we combine Nd and Pb isotope ratios in an attempt to robustly interpret changes in dust provenance through time in sediment cores retrieved across a central equatorial Pacific transect that covers the modern extent of the ITCZ. Given that dust is effectively scavenged by precipitation, we interpret changes in hemispheric provenance as displacement of the ITCZ through time. Samples were collected from three piston cores recovered from near the Line Islands ridge. They represent a seven-degree-latitude north-south transect across the modern position of the ITCZ near 160°W. The Line Islands are an ideal location for this study because at this longitude the ITCZ is well defined and has little deflection due to continental masses.

2.2 Methodology

2.2.1 Site and sampling

In May 2012, cruise MGL1208 aboard the R/V Marcus Langseth investigated a portion of the Line Islands dominated by a relatively broad volcanic ridge (100–300 km in length; Lynch-Stieglitz et al., 2015) . Here, we have selected sediment samples retrieved during that cruise from three piston cores along a North-South Transect, ML1208-37BB (37BB) at 7.04°N, 161.63°W, ML1208-31BB (31BB) at 4.68°N, 160.05°W, ML1208-18GC at 0.59°N, 156.66°W, and ML1208-17PC (17PC) at 0.48°N, 156.45°W, and (Fig. 2.1). Detailed descriptions of the core sites are available in Lynch-Stieglitz et al. (2015), as well as in a cruise report (Lynch Stieglitz et al., 2012). The most northern core (MGL1208-37BB) coincides with the northern extent of the ITCZ in boreal summer (at 7°N) and our most southern core (MGL1208-17PC) is below the boreal winter position of the ITCZ (at 0.5°N).

The cores record low sedimentation rates, but these cores were chosen because they had some of the highest sedimentation rates from the Line Island transect cores collected. MGL1208-17PC (0.48°N, 2926 m water depth) has an estimated sedimentation rate at the MIS 3/4 boundary of about 3.0 cm/kyr (Lynch-Stieglitz et al., 2015). MGL1208-31BB (4.68°N, 2857 m water depth) has an average sedimentation rate of about 3.7 cm/kyr (Lynch-Stieglitz et al., 2015). Lastly, the northernmost core MGL1208-37BB (7.04°N, 2798 m water depth) has the lowest sedimentation rate of 1.54 cm/kyr (Lynch-Stieglitz et al., 2015).

The cores were sampled at 4-cm and 5-cm intervals, allowing for a maximum temporal resolution of approximately one sample every 1000 years for the two southern cores, and one sample every 2500 years for the northernmost core. The identification of the age-depth

relationships was developed based on planktonic foraminifera oxygen isotope stratigraphy, as well as carbon-14 dated samples (Lynch-Stieglitz et al., 2015).

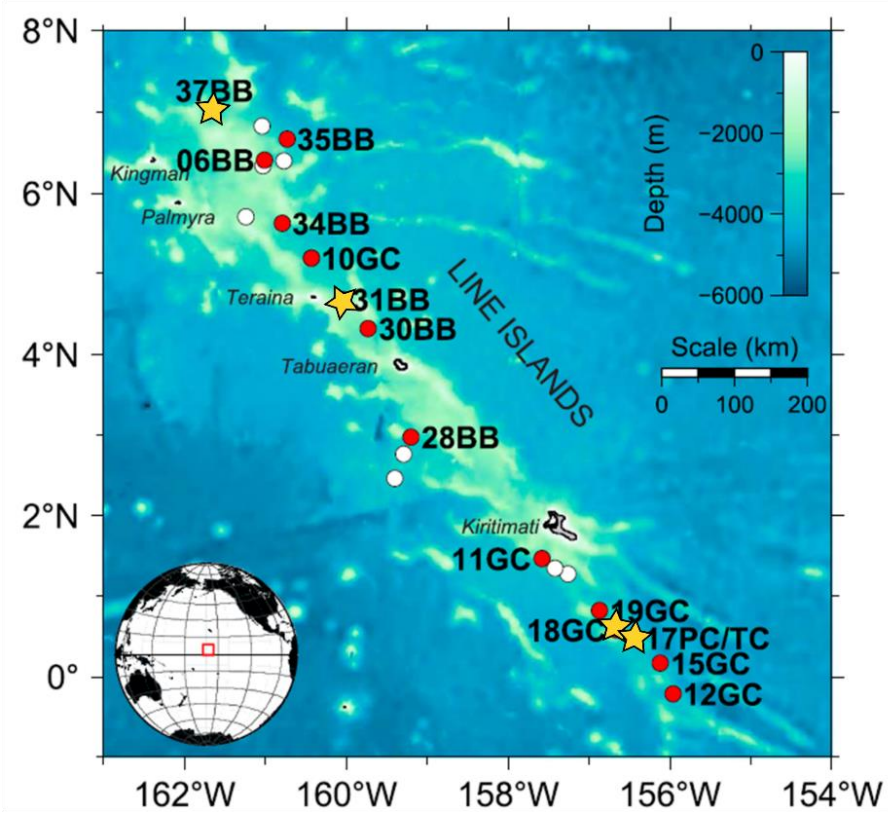

Figure 2.1 Bathymetric map with the location sediment cores from cruise MGL-1208. The yellow stars are the cores used in this study: 17PC--0.5° N, 18GC--0.6°N, 31BB--4.5° N, and 37BB--7° N. The red dots mark cores with oxygen isotope data discussed in Lynch-Stieglitz et al. (2015) while the white dots are cores with multi-sensor track (MST) data only. Modified from Lynch-Stieglitz et al. (2015).

2.2.2 Radiogenic isotope analysis

All work was performed in the clean laboratory of the Williams Radiogenic Isotope Geosciences Facility at Texas A&M University. In order to analyze Pb and Nd isotopes, we first isolated the operationally-defined detrital fraction of the sediment. The first step was to wet-sieve the sediments and isolate the <63µm size fraction. The sieved sediments were then treated to

chemically separate the detrital portion based on a sequential extraction procedure presented in (Xie and Marcantonio, 2012) and outlined as follows. The carbonate fraction was digested with buffered acetic acid to avoid leaching the clay. Ten percent acetic acid buffered with sodium acetate was added to the sample until no more visible fizzing occurred upon addition of acid. After this step, we leached the authigenic Fe-Mn oxyhydroxide portion of the samples using 0.02 M hydroxylamine hydrochloride with 25% acetic acid. Finally, the samples were placed overnight in a water bath at 80°C with 2M KOH to remove biogenic opal. Once the operationally-defined aluminosilicate fraction was isolated, the samples were dried at 60°C and weighed before being fully digested.

Detrital fractions of the sediment were digested with high-purity concentrated acids. First the samples were placed in a mixture of HF-HNO_3 (5:2) at 120°C for two days. This step was repeated once. Then, the samples were digested with aqua regia at 80°C until dry.

The dissolved samples were first run through an anion exchange (AG1X8, 200-400 mesh), hydrobromic acid column to separate Pb. The Rare Earth Elements (REEs) were collected during the rinse step of the Pb columns and additionally passed through RE Spec (Eichrom) columns to purify the REE fraction. The REE fraction was then loaded onto Ln Spec (Eichrom) columns to purify and separate the Nd from the rest of the REEs. Finally, the isotopic composition of the samples was analyzed for Nd and Pb by Thermal Ionization Mass Spectrometry (TIMS) at Texas A&M University.

Pb was loaded onto rhenium filaments with silica gel and was measured in static mode. Pb isotopes, expressed as the ratio of the radiogenic isotope ($^{206, 207, \text{or } 208}$Pb) to the non-radiogenic isotope (^{204}Pb), were corrected for mass fractionation (0.1%/amu) based on multiple runs of the

NIST981 Pb standard. The procedural Pb blank, analyzed with a ^{205}Pb spike, was found to be less than 50 pg, and no blank corrections on the measured ratios were necessary.

Nd was loaded onto rhenium filaments and measured in static mode as the Nd^+ ion. $^{143}Nd/^{144}Nd$ ratios were corrected for any Sm interference on mass 144 by monitoring mass 147. $^{143}Nd/^{144}Nd$ ratios were normalized to $^{146}Nd/^{144}Nd = 0.7219$. Standard JNdi-1 was run throughout this study and gave a mean value of $^{143}Nd/^{144}Nd = 0.512101 \pm 4$ ppm (1σ, n= 34). No further corrections were made to the Nd data in this study. $^{143}Nd/^{144}Nd$ ratios in this study are expressed as ε_{Nd} values (Equation 1), where $(^{143}Nd/^{144}Nd)_{CHUR} = 0.512638$ is the $^{143}Nd/^{144}Nd$ ratio of the Chondritic Uniform Reservoir (i.e. Bulk Earth).

2.3 Results

2.3.1 Isotope results

The overall range in the $^{208}Pb/^{204}Pb$ ratio for all of the samples analyzed is between 37.8 a 39.2, while that for the $^{206}Pb/^{204}Pb$ ratio is between 17.8 and 18.9 (Fig. 2.2; Table S1, supplementary information). The widest range in Pb isotope values is seen at site 31BB (4.5°N). At 31BB, the greatest difference in Pb isotope values is found between the glacial samples at MIS2 (Marine Oxygen Isotope Stage 2) and the Holocene samples. Samples from sites 17PC and 37BB have narrower ranges of Pb isotope values as well as smaller differences between the Holocene and Glacial samples. There is a difference in the amplitude of the $^{206}Pb/^{204}Pb$ and the $^{208}Pb/^{204}Pb$ ranges; however, the trends with time are similar (Fig. 2). $^{207}Pb/^{204}Pb$ ratios have the smallest range (Table S1) and, yet, mimic the temporal trend in both $^{206}Pb/^{204}Pb$ and the $^{208}Pb/^{204}Pb$ ratios. Due to the strong consistency of the Pb isotope ratios between samples from site 18GC and 17PC, figures 2 and 3 present the equatorial Pb data as a single composite (Supplemental section S2).

Nd isotope ratios, expressed throughout this study as ε_{Nd}, range from -0.2 to -13.3 (Fig. 2, Table S1, APPENDIX A). Most of the variation is related to location of the core. 17PC, the equatorial core, has the most positive Nd isotope ratios (ε_{Nd} = -7.4 to ε_{Nd} = -0.2), while the northern cores, 31BB (ε_{Nd} = -12.1 to ε_{Nd} -5.1) and 37BB (ε_{Nd} = -13.3 to ε_{Nd} -8.3) have Nd isotope ratios that are more negative. We do not include the three data points closest to the top of core 31BB, because there is evidence that this part of the core is reworked (Lynch-Stieglitz et al.) Table S1, Appendix A). We, therefore, only include points from 15 cm and below for this core.

2.4 Discussion

2.4.1 Dust sources to the CEP

In order to trace ITCZ migration we differentiated between possible southern and northern hemisphere sources, based on published Nd and Pb isotope ranges in regional studies (potential source ranges shown in Figures 2.2 and 2.3). We can sort our data into four different dominant dust source regions, three southern hemisphere South American regions and one northern hemisphere East Asian end member. How delivery of material from these sources varies through time is explored in section 4.3.

Recent work has signaled western South America, through circulation of the SE trade winds, as a main source of dust to the Eastern Equatorial Pacific (e.g. Xie and Marcantonio, 2012, Pichat et al., 2014). The detailed characterization of sources within South America is based on the composition of volcanic and basement rocks on the western part of the continent as characterized and compiled by Mamani et al. (2008) and Mamani et al. (2010), as well as analysis of some suspended riverine sediments in Patagonia (Gaeiro et al., 2007). $^{206}Pb/^{204}Pb$ ratios range from 17.5 – 19.0; and ε_{Nd} ranges from 4 to – 12. This approach is appropriate since

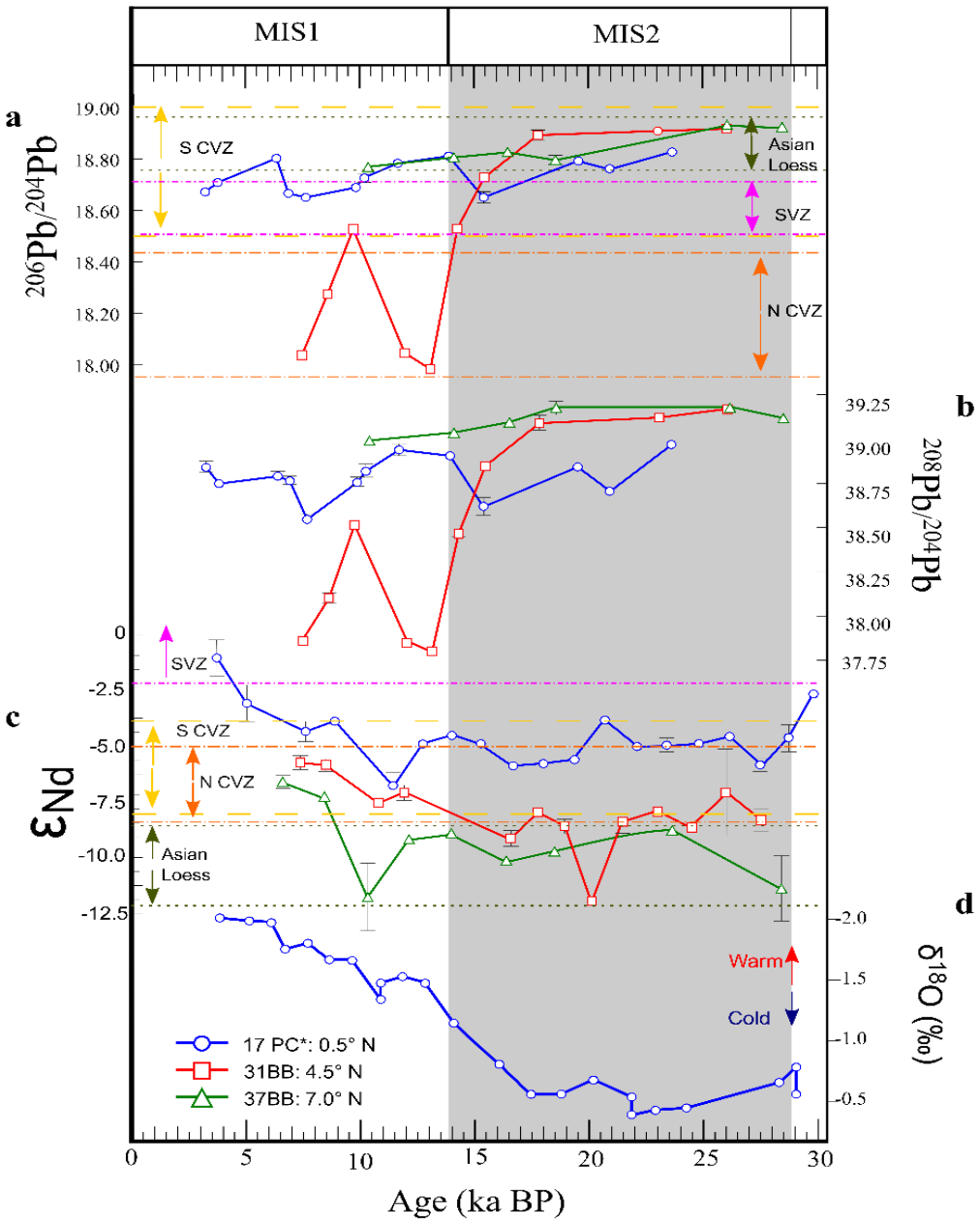

Figure 2.2 CEP Pb ad Nd radiogenic isotope record. a) $^{208}Pb/^{204}Pb$, b) $^{206}Pb/^{204}Pb$, and c) Nd isotope ratios plotted against time for all cores (17PC*, blue; 31BB--4.5° N, red; and 37BB--7° N, green). MIS 1 (Holocene) and MIS 2 (shaded) time periods are based on planktonic foraminifera $\delta^{18}O$ (shown only for core 17PC in panel d) and radiocarbon analyses (Lynch-Stieglitz, 2015). 17PC* is a composite equatorial core consisting of samples from core 17PC at 0.5° N and 18GC at 0.6 ° N (see section S1). The error bars represent standard errors. Possible dust source interpretations are marked by dashed lines. The South Central Volcanic Zone (S-CVZ, yellow) and the North Central Volcanic Zone (N-CVZ, orange) Pb and Nd ranges are from Mamani et al. (2010), and references therein. For the South Volcanic Zone (SVZ, pink) the Pb isotope range is based on Pichat et al. (2014) and references therein, and the Nd isotope range is from Gaiero et al. (2007). The Pb isotope ranges for Asian loess (dark green) are from Sun and Zhu. (2010), while the Nd values for Asian Loess from Zhang et al. (2015).

chemical or physical weathering does not further fractionate the Pb and Nd isotope signatures of detrital sediment (Grousset and Biscaye, 2005). Furthermore, in South America, Nd isotope work conducted on detrital-rich margin sediments shows that the Nd signal is dominated by the crystalline rocks of the continent (Jeandel et al., 2007).

In our data we can see the dominant isotopic signature of two sections of the Andes Cordillera, ranging from 16°S to 43°S, the Central Volcanic Zone and the South Volcanic Zone. The Central Volcanic Zone (CVZ), lying between 16° S and 27° S, can be subdivided into two critical regions, north and south. The *Northern Central Volcanic Zone* (N-CVZ), also known as

the Arequipa Domain extends from 16° S to 21° S and is characterized by the least radiogenic Pb isotope ratios and medium to low ε_{Nd} values ($^{206}Pb/^{204}Pb$ ratios of 17.50 to 18.45; $^{208}Pb/^{204}Pb$ ratios of 37.63 to 38.66; ε_{Nd} values between -5.5 and -8; Mamani et al., 2008, Mamani et al., 2010). We suggest that the northern CVZ is the dominant source of dust to 4.5° N (core 31BB) during MIS2, and to 7° N (core 37BB) during the mid-Holocene (Fig. 2).

The *Southern Central Volcanic Zone* (S-CVZ), also known as the Antofalla domain, ranges from 22° S to 27.5° S and is dominated by more radiogenic Pb isotopes ratios and higher ε_{Nd} values ($^{206}Pb/^{204}Pb$ ratios of 18.50 to 19.00; $^{208}Pb/^{204}Pb$ ratios of 38.86 and 39.00; ε_{Nd} isotope values between -3 and -6; Mamani et al., 2008, Mamani et al., 2010). The southern CVZ is likely the dominant source of dust to the equator (cores 17PC and 18GC) during MIS2 and until the mid-Holocene (Fig. 2).

In contrast the *Southern Volcanic Zone* (SVZ), which was estimated by Pichat et al. (2014) to be the main source of dust to the EEP through the deglacial, lies further south and extends from 33° S to 43° S. The SVZ is characterized by $^{206}Pb/^{204}Pb$ ratios of 18.5 to 18.7 and $^{208}Pb/^{204}Pb$ of 38.3 to 38.6 (Pichat et al., 2014), and relatively radiogenic neodymium isotope

values from -2 to +2 (Gaiero et al., 2007). We suggest that the SVZ is the dominant source of dust to the equatorial site (17PC) during the mid-Holocene (Fig. 2).

Our northern hemisphere end member is dominated by an Asian Loess signal, most closely identified with the fine-grained fraction of sediments from the Chinese Loess Plateau ($^{206}Pb/^{204}Pb$ ratios between 18.82 and 18.98, and $^{208}Pb/^{204}Pb$ ratios between 39.04 and 39.20; Sun and Zhu, 2010; ε_{Nd} values that range between -10 and -11.5; Rao et al. 2008, Wang et al. 2007, Zhang et al. 2015). Our Asian end-member is consistent with the findings of Pb isotope ratios in the detrital component of North Pacific sediments (Jones et al., 1994, 2000). Asian Loess is the main source of dust to7° N (37BB) through MIS2 until the mid-Holocene, and to 4.5° N (31BB) during MIS2 (Fig. 2).

Much of the geochemical variation in dust from East Asia is captured in the signature provided by $^{87}Sr/^{86}Sr$ isotope ratios (Zhang et al., 2015). Unfortunately, we could not analyze our samples for $^{87}Sr/^{86}Sr$ isotope ratios because research shows that within 5° of the equator separated detrital material is easily contaminated with detrital barite (Xie and Marcantonio, 2012). This barite, characteristic of high-productivity areas (Paytan et al., 1996), is enriched in seawater Sr, which overwhelms the total detrital Sr isotope signature. In contrast, Xie and Marcantonio (2012) demonstrated that the ε_{Nd} values of detrital material in the EEP was free of barite influence, most likely due to the low relative concentration of neodymium in barite relative to dust (Martin et al., 1995). Similarly, leaching experiments by Pichat et al. (2014) concluded that there is little variation in the isotopes of Pb between different leached phases of the sediment, and that the bulk sediment record of Pb isotopes closely matches that of the eolian input, showing that barite contamination is not a major concern for the isotopic composition of residual Pb. Therefore, the Pb and Nd isotope ratios of our operationally-defined detrital

components are sufficient to differentiate between the two main sources of dust (Asian Loess and South American volcanics) delivered to the CEP (Fig. 3).

2.4.2 Particulate matter from the Pacific Equatorial Undercurrent

Material from Papua New Guinea (PNG) can be carried to the CEP by the Equatorial Undercurrent (EUC). Particulate and dissolved traces have been found as far east as 140°W (Ziegler et al., 2008). The EUC flows eastward along the equator within a narrow latitudinal band of ±2°, weakening dramatically outside of this range (Lukas and Firing, 1984). In this study, the only core that can be potentially influenced by particulate material from the EUC is 17PC (at 0.5°N). PNG materials are very radiogenic with respect to Nd and less radiogenic with respect to Pb (ε_{Nd} = +8 to +9; $^{206}Pb/^{204}Pb$ = 17.5-18.5; $^{208}Pb/^{204}Pb$ = 37.25-38.50; Kennedy et al., 1990, Part et al., 2010) . Work by Costa et al. (2016) on these Line Islands cores, spanning the same time frame studied here, suggests a very limited influence of the EUC in the detrital fraction of sediment from these cores. They base this suggestion on their estimated levels of productivity during the LGM that are low, despite dust fluxes that are 2-3 time higher during the same time period. Costa et al. (2016) suggest that a limited EUC influence, might be attributed to a decreased riverine discharge associated with regionally dry conditions in PNG (Reeves et al., 2013). Here, we offer further evidence for limited influence of EUC particulates on the detrital component of sediments of the CEP, as *both* our Pb and Nd isotope ratios are consistent with a South American provenance and show no evidence for PNG material. More specifically, we attribute the higher ε_{Nd} values in core 17PC during the mid-Holocene, to an increased influenced of dust from the Southern Volcanic Zone (Gaiero et al., 2007). Moreover, for a given $^{206}Pb/^{204}Pb$ isotope ratio, the $^{208}Pb/^{204}Pb$ ratio in our samples is far too radiogenic, and thus inconsistent with a PNG provenance.

2.4.3 Provenance changes over time

Based on both the Pb and the Nd isotope values, the provenance of the dust in the northernmost core (37BB) at 7.04° N is consistent with Asian Loess from the early Holocene throughout MIS2 (Fig. 2.2). While there is some overlap in the Pb isotope range of Asian Loess and the S-CVZ, the ε_{Nd} values in our samples (ε_{Nd} = -8.3 to -11.8) have a clear Asian loess dominance (Zhang et al., 2015). The most recent sample from 37BB, at 6.6 kyr BP has a more radiogenic Nd isotope value (ε_{Nd} = -6.6) suggesting a provenance change to a southern hemisphere source, either the N-CVZ or the S-CVZ (Fig. 2.2).

The core at 4.5° N (31BB) records the most change through time with respect to Pb isotope ratios (Fig. 2.2). Values before the Holocene are consistent with a Northern Hemisphere provenance, interpreted here as derived from Asian Loess (Sun and Zhu, 2010). The Nd isotope values during this period are mostly in the upper range of Asian Loess (Zhang et al., 2015), but are very distinct from either the S-CVZ (Mamani et al., 2008) or the SVZ (Gaiero et al., 2007) (Fig. 2.2). During the Holocene the provenance of the dust has a signature consistent with the Southern Hemisphere, specifically dominated by the N-CVZ in South America (Mamani et al., 2010) (Fig. 2.2).

The provenance of the dust in the equatorial core (17PC) is more consistent with a S-CVZ source through most of the study period. For the same core, during the latter half of the Holocene there is a progressive increase in the neodymium isotope ratios from ε_{Nd} = -3.9 at 8.9 kyr BP to ε_{Nd} = -1.1 at 3.7 kyr BP, and little change in the Pb isotope ratios over the same time period. We suggest this variation is due to an increase in dust that is sourced from the SVZ (Fig. 2.2).

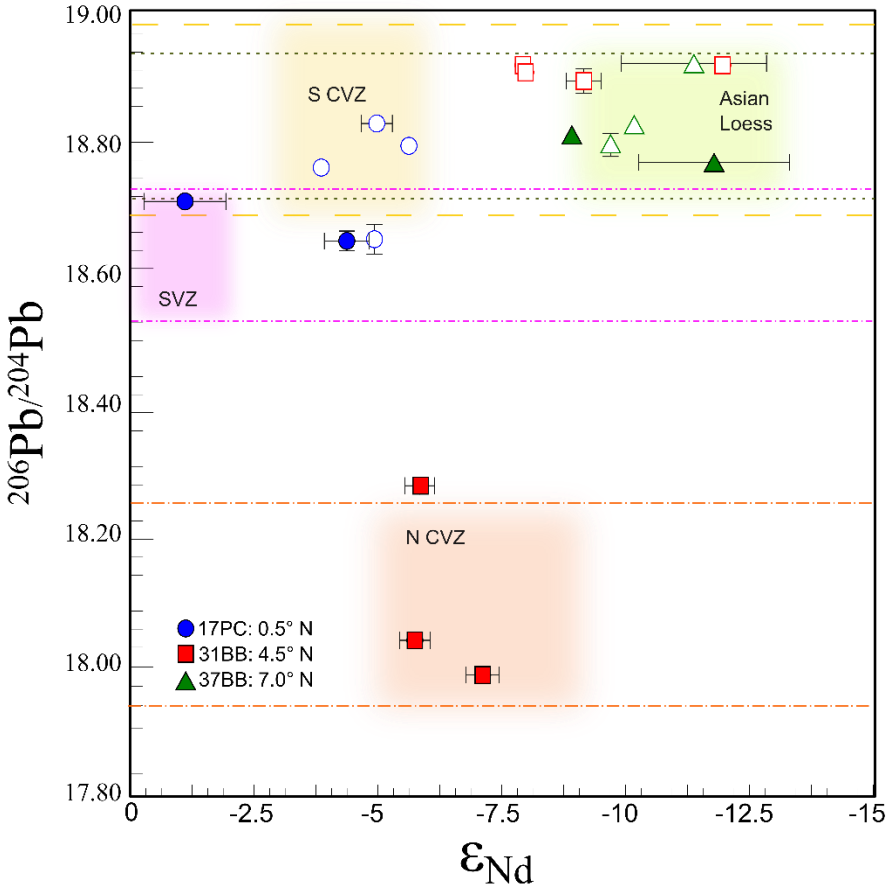

Figure 2.3 Pb vs Nd record in the CEP. $^{206}Pb/^{204}Pb$ versus ε_{Nd} for all three sites (17PC--0.5° N, blue circles; 31BB--4.5° N, red squares; and 37BB--7° N, green triangles). The error bars represent standard errors. Filled shapes are Holocene samples, and open shapes are glacial samples. Possible dust source interpretations are marked by dashed lines and the shaded areas. Note that the largest temporal shift occurs between Holocene and glacial samples in 31BB. The South Central Volcanic Zone (S-CVZ, yellow) and the North Central Volcanic Zone (N-CVZ, orange) Pb and Nd ranges are from Mamani et al. (2010), and references therein. For the South Volcanic Zone (SVZ, pink) the Pb isotope range is based on Pichat et al. (2014) and references therein, and the Nd isotope range is from Gaiero et al. (2007). The Pb isotope ranges for Asian loess (dark green) are from Sun and Zhu. (2010), while the Nd values for Asian Loess from Zhang et al. (2015).

Taking into account both the Pb and Nd isotope ratios, it is possible to group the provenance of the dust at these study sites into four groups (Fig. 2.3). Three are Southern Hemisphere sources in South America (the S-CVZ, the N-CVZ, and the SVZ) and one is a Northern Hemisphere source (Asian Loess). Figure 3 more clearly illustrates the shift in the provenance of dust in core 31BB (4.5° N) between the glacial and the deglacial. More

importantly, our radiogenic isotope data identify changes in source provenance regardless of whether or not there are changes in dust flux. Indeed, along the same 7-degree transect, Costa et al. (2016) found that the variability of dust flux within the Holocene, or the glacial, period across the transect is negligible when compared to the more than doubling of dust fluxes between the same time periods (Costa et al., 2016). One might expect that a transition between northern and southern hemisphere dust delivery would be associated with a sharp decrease in dust flux at varying times and positions within the transect, but these fluxes remain constant across the entire 7-degree transect during the same time slices. On the other hand, in the equator core studied here, Jacobel et al. (2016) argued for displacement of the ITCZ using evidence for changes in dust flux at the penultimate termination, during which differences between northern and southern hemisphere dust fluxes are greater than within the Holocene or the glacial periods.

2.4.4 ITCZ migration

Studies of the past 30 kyr from different regions tend to agree with a southern displacement of the ITCZ at the LGM, providing evidence for reduced precipitation, a weakened summer monsoon and increased winter trade winds in the Northern hemisphere, and increased precipitation in central South America and Northern Australia (McGee et al., 2014and references therein). In the Atlantic Ocean, researchers studying shifts in past sea-surface salinities and temperatures have estimated a 7° meridional southward shift of the ITCZ during the LGM compared to its modern mean position (Arbuszewski et al., 2013).

As the ITCZ acts as a barrier for inter-hemispheric dust deposition, meridional changes in dust provenance help us to locate the paleo-position of ITCZ (Fig. 2.4). Samples from 17PC consistently have a South American provenance throughout the Holocene and the Glacial (mostly S-CVZ, but a hint of SVZ in latest Holocene; Figures 2 and 3). Site 31BB shows the

most heterogeneity in the provenance of dust, with glacial samples having provenance dominated by Asian Loess, and Holocene samples showing dust provenance consistent with the N-CVZ. For site 37BB at 7.04°N there are only nine data points in the studied time period (i.e., past 30 kyr), and this is mostly due to the very low sedimentation rate (1.54 cm/kyr, Lynch-Stieglitz et al., 2015). Between 10 kyr BP and 28.4 kyr BP, the Nd and Pb isotope systematics suggest an Asian Loess provenance (Figures 2 and 4). However, the Nd isotope ratio measured at site 37BB for the most recently deposited sediment (6 kyr BP) suggests a Southern Hemisphere source (ε_{Nd} = -6.6 ± 0.3), consistent with published work hypothesizing that the ITCZ migrated further north during the mid-Holocene, and then migrated south to its modern position (McGee et al., 2014, Arbuszewski et al., 2013, Donohoe et al., 2013). We do not have data for locations between 4.5°N and 0.5°N and, hence, cannot further constrain the ITCZ shift to better than between 2.5° and 7° in the CEP (Fig. 2.4).

Work by Xie and Marcantonio (2012) did not find evidence of Asian Loess dust in the EEP, but these authors did suggest that the ITCZ shifted further north during the deglacial, in agreement with our data. Models suggest that the greatest displacement of the ITCZ happens during Heinrich stadials (Chiang and Bitz, 2005). This interpretation has support from Jacobel et al. (2016) based on ^{232}Th dust fluxes that indicate a displacement of the ITCZ south of the equator during Heinrich 11 at the termination of the penultimate glacial. Unfortunately, we do not have the spatial, nor the temporal, resolution to determine whether the position of the ITCZ was further south during Heinrich 1 (~17 kyr) than that during the Last Glacial Maximum (21 kyr). Nevertheless, we suggest that the ITCZ did not migrate south of 17PC during the past 30 kyr, as we do not see a substantial excursion in the Nd isotope record that would be associated with an influx of dust of Asian provenance if the ITCZ had migrated below 17PC. Given the

robustness of the Nd and Pb isotope tracing capabilities in the CEP, we will focus future work on Heinrich stadial 11, to address and test the intriguing hypothesis put forward by Jacobel et al. (2016) which suggests a southward displacement of the ITCZ during a stadial event of the penultimate deglaciation.

2.4.5 Changes to the Southern Hemisphere Branch of the Hadley Cell

As with the position and changes to the ITCZ, the scientific community has been equally puzzled by the behavior of the Southern Hemisphere westerly winds (SWW) during glacial and interglacial stages (Kohfeld et al., 2013). Like the ITCZ the SWW are an important driver of climate change, and large-scale ocean circulation (Toggweiler and Samuels, 1995). Moreover, changes in the position and strength of the SWW might affect the ventilation of the Southern Ocean and, consequently, have a role in triggering glacial terminations through changes in the global carbon cycle (e.g. Anderson and Carr, 2010, Anderson et al., 2009). Deciphering the relationship between the ITCZ and the SWW could lead to clues that are crucial in determining changes to the southern hemisphere branch of the Hadley Cell through time. There is disagreement among scientists about the behavior of global SWW on glacial-interglacial timescales (Kohfeld et al., 2013), but we believe that contrasting our findings with recent work in the EEP (Pichat et al. 2014) can bring new light to these discussions.

Pichat et al. (2014) interpreted changes in the Pb isotope ratios of the detrital component through time in core ODP849 (at 110° W, 0.1° N) as reflecting changes in the contribution of dust to the EEP by the S-CVZ and the SVZ, with material from the SVZ dominating the Holocene dust flux. These changes suggest that during MIS2 the SWW were further north, thus allowing dust loading from further North in South America, and then migrated further south during the last termination. Our equatorial record from site 17PC similarly shows a S-CVZ

source of South American dust during MIS2. Although there is a migration toward a more southerly provenance for dust from the SVZ later in record, the shift does not occur until the mid-Holocene (Fig. 2.2).

To summarize, during the LGM, the more northerly South American provenance of dust (i.e., S-CVZ) delivered to the equator in the CEP (our work here) and the EEP (Pichat et al., 2014) suggest a scenario in which the SE trade winds are shifted equatorward. In tandem with the northward shift in South American dust sources at equator core during MIS2, there is a southward shift in ITCZ as documented by the Asian dust signals at site 31BB. Taken together, these shifts imply a constriction of the southern hemisphere trade wind belt (and Hadley Cell) towards the equator (from the N and the S).

A poleward migration of trade winds is suggested by the more southerly sources of South American dust (i.e., SVZ) determined during the deglacial in the EEP (Pichat et al., 2014) and the mid-Holocene in the CEP (our work here). In addition, during the Holocene, South American dust is delivered further north to site core 31BB (4.5° N) implying a northward displacement of the ITCZ. Later, during the mid-Holocene, South American dust is implicated even further north at site 37BB (7° N; Fig. 2.4). Taken together, the data for the equatorial Pacific suggest that during the Holocene, there is a northward migration of the ITCZ that is contemporaneous with an expansion of the trade wind belt toward the pole. A contraction (MIS2) and expansion (Holocene) of the Hadley Cell likely coincide with a northward and southward migration, respectively, of the SWW. Researchers studying Holocene sediments from the Atlantic Ocean have also shown a simultaneous poleward displacement of the SWW (Voigt et al., 2015), and a northward shift in the ITCZ (Arbuszewski et al., 2013) from the early to the mid-Holocene. These findings are not in agreement with model results, which suggest that during the LGM, due

to the smaller inter-hemisphere temperature contrast, the Hadley Cell should, in fact, expand, and then contract during the Holocene (Rind and Perlwitz, 2004).

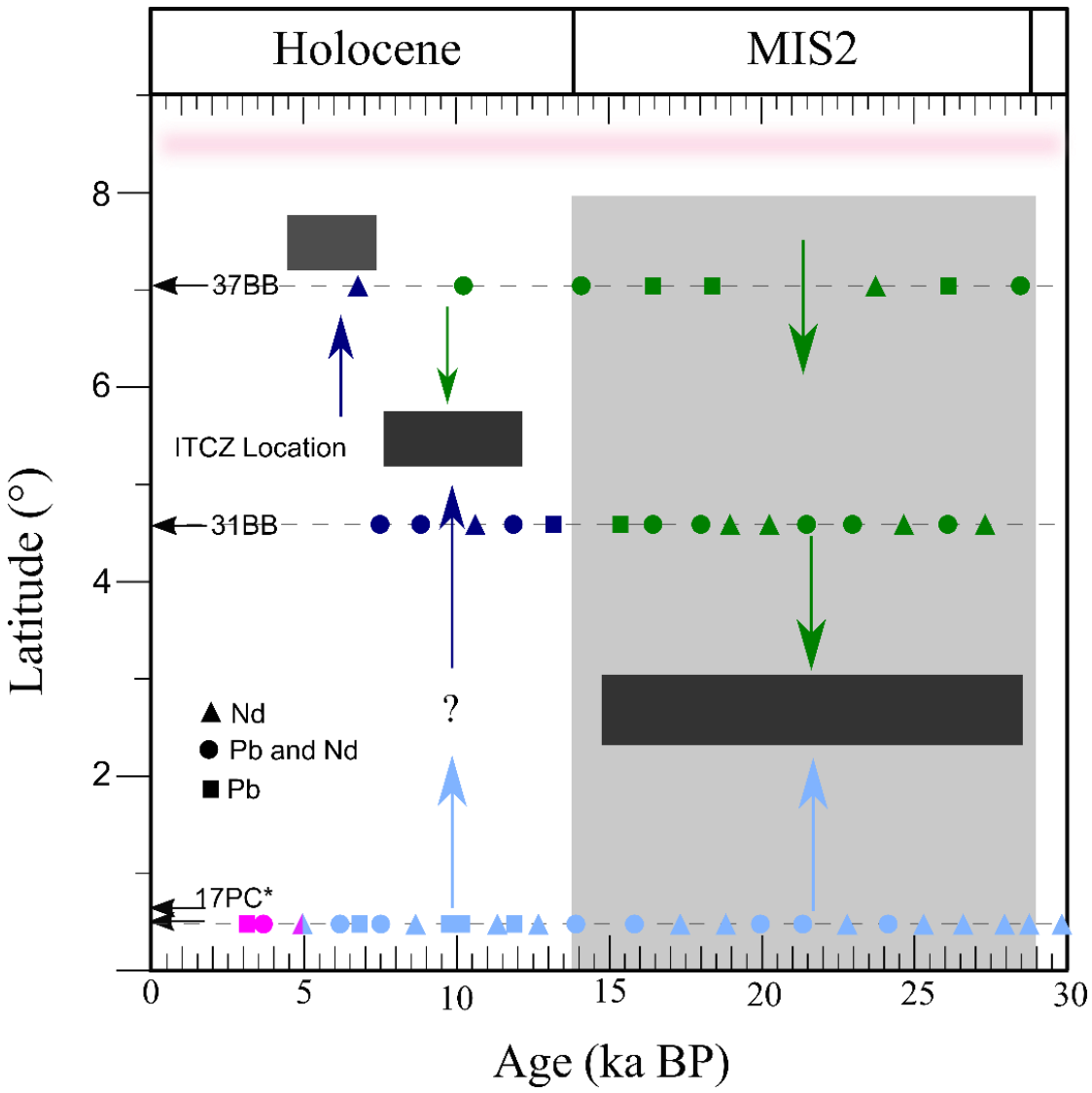

Figure 2.4 ITCZ migration over time. All data points are marked along the dashed lines representing the core latitude. The arrows show the minimum ITCZ displacement (solid line) and the maximum ITCZ displacement (dashed line) for each time period. The blue arrows indicate a southern shift and the red arrow a northern shift (without an upper constraint). The color of each data point indicates the provenance interpretation: Asian Loess (dark green), North Central Volcanic Zone (N-CVZ; orange), South Central Volcanic Zone (S-CVZ; yellow), South Volcanic Zone (SVZ; pink). The pink area shows the boreal summer ITCZ position over the CEP, as recorded by the local annual maximum precipitation, in the global precipitation climatology product (GCP) version 2.2 from NOAA (Adler et al., 2003).

2.4.6 Large meridional displacements of the ITCZ: models versus observations

McGee et al. (2014) estimated that displacements of ITCZ migration larger than 1° can only happen in limited regional settings. Our work suggests that the ITCZ at the CEP was at least 2.5° degrees further south during MIS2 than during the early Holocene– south of core 31BB (4.5° N), but north of core 17PC (0.5° N) during the glacial, and north of core 31BB but south of 37BB (7° N) during the Holocene (Fig. 2.4). Such displacements are significant, although less than those estimated in the Atlantic (range of ± 7°) between the LGM and the Holocene (Arbuszewski et al., 2013).

Most paleo-records that document changes in the position of the ITCZ base their interpretations on proxy records that either reflect changes in the location of maximum precipitation (e. g. Wang et al., 2001) or sea surface temperature (e. g. Koutavas and Lynch-Stieglitz, 2003). These records are often land based. For example, Wang et al.'s (2001) record from Hulu Cave speleothems correlates the predicted changes in precipitation with a migration of the ITCZ. Haug et al. (2001) used titanium concentrations in Cariaco Basin sediments as a proxy for increased riverine discharge, itself a symptom of an ITCZ migration. Importantly, it is not possible to discount the possibility that measured changes in precipitation can be due to a shift in the position of the ITCZ or to a change in its rainfall intensity (Schneider et al., 2014). Our estimates, however, are not based on, or altered by, precipitation amount, and we can therefore decouple the location of the mean ITCZ with potential changes in ITCZ intensity (and thus precipitation amount) between the LGM and the Holocene.

McGee et al. (2014) estimated the position of the ITCZ based on estimates of tropical SST gradients and the modelled relationship between the paleo ITCZ position and SST changes. Their models generally were in agreement with a migration of the ITCZ toward the warmer

hemisphere. However, the model was not consistent with the large ITCZ displacements interpreted by the paleo-record observations (e.g. Arbuszweski et al. 2013). They attributed the discrepancy between their estimates and larger published shifts to a decoupling of precipitation records from the ITCZ position, or to zonal heterogeneity. The latter allows for very large local changes in the ITCZ along some longitudes, as long as changes at other longitudes are near zero. Previous models have argued that changes to the ITCZ position must be zonally homogenous (Frierson and Hwang, 2012), but we suggest that there is indeed some heterogeneity, at least between different oceans, as our estimates of migration at the CEP are smaller than previous observations in the Atlantic during the same time period (~ 7°; Arbuszweski et al., 2013) .

Other studies using dust provenance in the Pacific, but in the EEP, have found conflicting information regarding the magnitude of the migration of the ITCZ. A Nd isotope study of dust provenance by Xie and Marcantonio (2012) did not find evidence for a significant displacement of the ITCZ between the LGM and the Holocene, contradicting the SST data for a similar location (e.g. Koutavas and Lynch-Stieglitz, 2003). However, a similar study in the EEP using Pb isotope ratios by Pichat et al. (2014) did associate changes in the dust provenance in the EEP to a southward retreat of the SWW during the Holocene, which might be concurrent with a northward migration of the ITCZ as suggested in this study.

Work by Donohoe et al. (2013) demonstrates that the relationship between the cross-equatorial heat transport and the position of the ITCZ is robust, as reflected by both models and observations. However, the relationship between the location of maximum precipitation, and the change in the SST gradient is more variable. Modeled work has shown that different climate states have varying relationships between the latitudinal change in the ITCZ position and the change in the tropical SST gradient (Donohoe et al., 2013, McGee et al., 2014). We suggest that

dust provenance records can be used as an independent constraint for ITCZ paleo-position, and together with SST observations, a more precise quantitative relationship between changes in tropical SST gradients and the location of the ITCZ can be calculated for each climate state. This would allow researchers to use SST gradients, for which there is more abundant information, to more accurately calculate the position of the ITCZ. Unfortunately, there are no current estimates for the change in the SST gradient in the CEP between the Holocene and the LGM.

2.5 Conclusion

The ITCZ is an important hydroclimate element that affects the lives of billions of people and understanding its sensitivity to hemispheric temperature gradients is critical to accurately predicting its behavior in the future. This work has shown that it is possible to successfully use radiogenic isotopes (Pb and Nd) to fingerprint the potential sources of dust, and trace ITCZ migration in the CEP during the past 30 kyr. The radiogenic isotope evidence, combined with other literature data (Jones et al., 2000, Jones et al., 1994), as well as robust atmospheric circulation models (e.g., Mahowald et al., 2011), has allowed us to narrow potential dust sources to the CEP as being either from Asia or South America. The most northern core (37BB) reflects a dust signal dominated by Asian loess, as most starkly reflected in the Nd isotope data. The equatorial core (17PC) has a dust provenance dominated by South American sources (S-CVZ and SVZ), while the middle core (31BB) at 4.5°N incorporates dust sources from both Asian and South America (N-CVZ).

These changes in dust provenance that the ITCZ has shifted south of its modern position by least 2.5 °, but less than 7 °, during the last glacial cycle. The direction of this shift is consistent with previous work, both in modelling (Broccoli et al., 2006, Chiang and Bitz, 2005) and observations (Koutavas and Lynch-Stieglitz, 2003, Arbuszewski et al., 2013, McGee et al.,

2014). The magnitude of the shift, however, is much larger than the global estimated change of less than 1° (McGee et al., 2014), and further work is needed to explain the discrepancy between modelled estimates of ITCZ position and observations.

2.6 References

ADLER, R. F., HUFFMAN, G. J., CHANG, A., FERRARO, R., XIE, P.-P., JANOWIAK, J., RUDOLF, B., SCHNEIDER, U., CURTIS, S. & BOLVIN, D. 2003. The version-2 global precipitation climatology project (GPCP) monthly precipitation analysis (1979-present). *Journal of hydrometeorology,* 4.

ANDERSON, R. F., ALI, S., BRADTMILLER, L. I., NIELSEN, S. H. H., FLEISHER, M. Q., ANDERSON, B. E. & BURCKLE, L. H. 2009. Wind-Driven Upwelling in the Southern Ocean and the Deglacial Rise in Atmospheric CO_2. *Science,* 323**,** 1443-1448.

ANDERSON, R. F. & CARR, M.-E. 2010. Uncorking the Southern Ocean's vintage CO2. *Science,* 328**,** 1117-1118.

ARBUSZEWSKI, J. A., CLÉROUX, C., BRADTMILLER, L. & MIX, A. 2013. Meridional shifts of the Atlantic intertropical convergence zone since the Last Glacial Maximum. *Nature Geoscience*.

BROCCOLI, A. J., DAHL, K. A. & STOUFFER, R. J. 2006. Response of the ITCZ to Northern Hemisphere cooling. *Geophysical Research Letters,* 33.

CHIANG, J. C. & BITZ, C. M. 2005. Influence of high latitude ice cover on the marine Intertropical Convergence Zone. *Climate Dynamics,* 25**,** 477-496.

CHIANG, J. C. & FRIEDMAN, A. R. 2012. Extratropical Cooling, Interhemispheric Thermal Gradients, and Tropical Climate Change. *Annual Review of Earth and Planetary Sciences,* 40**,** 383-412.

COSTA, K. M., MCMANUS, J. F., ANDERSON, R., REN, H., SIGMAN, D., WINCKLER, G., FLEISHER, M., MARCANTONIO, F. & RAVELO, A. 2016. No iron fertilization in the equatorial Pacific Ocean during the last ice age. *Nature,* 529**,** 519-522.

DONOHOE, A., MARSHALL, J., FERREIRA, D. & MCGEE, D. 2013. The relationship between ITCZ location and cross-equatorial atmospheric heat transport: From the seasonal cycle to the Last Glacial Maximum. *Journal of Climate,* 26.

FRIERSON, D. M. & HWANG, Y.-T. 2012. Extratropical influence on ITCZ shifts in slab ocean simulations of global warming. *Journal of Climate,* 25**,** 720-733.

GAIERO, D. M., BRUNET, F., PROBST, J.-L. & DEPETRIS, P. J. 2007. A uniform isotopic and chemical signature of dust exported from Patagonia: Rock sources and occurrence in southern environments. *Chemical Geology,* 238**,** 107-120.

GROUSSET, F. E. & BISCAYE, P. E. 2005. Tracing dust sources and transport patterns using Sr, Nd and Pb isotopes. *Chemical Geology*.

HAUG, G. H., HUGHEN, K. A., SIGMAN, D. M., PETERSON, L. C. & RÖHL, U. 2001. Southward migration of the intertropical convergence zone through the Holocene. *Science (New York, N.Y.),* 293**,** 1304-1308.

JACOBEL, A. W., MCMANUS, J., ANDERSON, R. & WINCKLER, G. 2016. Large deglacial shifts of the Pacific Intertropical Convergence Zone. *Nature Communications,* 7.

JEANDEL, C., ARSOUZE, T., LACAN, F., TECHINE, P. & DUTAY, J.-C. 2007. Isotopic Nd compositions and concentrations of the lithogenic inputs into the ocean: A compilation, with an emphasis on the margins. *Chemical Geology,* 239**,** 156-164.

JONES, C. E., HALLIDAY, A. N., REA, D. K. & OWEN, R. M. 1994. Neodymium isotopic variations in North Pacific modern silicate sediment and the insignificance of detrital REE contributions to seawater. *Neodymium isotopic variations in North Pacific modern silicate sediment and the insignificance of detrital REE contributions to seawater*.

JONES, C. E., HALLIDAY, A. N., REA, D. K. & OWEN, R. M. 2000. Eolian inputs of lead to the North Pacific. *Eolian inputs of lead to the North Pacific*.

KENNEDY, A., HART, S. & FREY, F. 1990. Composition and isotopic constraints on the petrogenesis of alkaline arc lavas: Lihir Island, Papua New Guinea. *Journal of Geophysical Research: Solid Earth,* 95**,** 6929-6942.

KOHFELD, K., GRAHAM, R., DE BOER, A., SIME, L., WOLFF, E., LE QUÉRÉ, C. & BOPP, L. 2013. Southern Hemisphere westerly wind changes during the Last Glacial Maximum: paleo-data synthesis. *Quaternary Science Reviews,* 68**,** 76-95.

KOUTAVAS, A. & LYNCH-STIEGLITZ, J. 2004. Variability of the marine ITCZ over the eastern Pacific during the past 30,000 years. *The Hadley Circulation: Present, Past and Future*. Springer.

KOUTAVAS, A. & LYNCH-STIEGLITZ, J. 2003. Glacial-interglacial dynamics of the eastern equatorial Pacific cold tongue-Intertropical Convergence Zone system reconstructed from oxygen isotope records. *Paleoceanography,* 18.

LUKAS, R. & FIRING, E. 1984. The geostrophic balance of the Pacific Equatorial Undercurrent. *Deep Sea Research Part A. Oceanographic Research Papers,* 31**,** 61-66.

LYNCH-STIEGLITZ, J., POLISSAR, P. J., JACOBEL, A. W., HOVAN, S. A., POCKALNY, R. A., LYLE, M., MURRAY, R. W., RAVELO, C. A., BOVA, S. C., DUNLEA, A. G., FORD, H. L., HERTZBERG, J. E., WERTMAN, C. A., MALONEY, A. E., SHACKFORD, J. K., WEJNERT, K. & XIE, R. C. 2015. Glacial-interglacial changes in central tropical Pacific surface seawater property gradients. *Paleoceanography,* 30**,** 423-438.

LYNCH STIEGLITZ, J., POLISSAR, P., POCKALNY, R., LYLE, M., MURRAY, R. & RAVELO, A. C. 2012. *MGL12-08 Line Islands Ridge Survey and Core Collection. Cruise Report* [Online]. Available: http://shadow.eas.gatech.edu/~jean/Line_Islands/MGL1208_Cruise_Report.pdf [Accessed 03/15/2015].

MAHOWALD, N. M., YOSHIOKA, M., COLLINS, W. D., CONLEY, A. J., FILLMORE, D. W. & COLEMAN, D. B. 2006. Climate response and radiative forcing from mineral aerosols during the last glacial maximum, pre-industrial, current and doubled-carbon dioxide climates. *Geophysical Research Letters,* 33.

MAMANI, M., TASSARA, A. & WÖRNER, G. 2008. Composition and structural control of crustal domains in the central Andes. *Geochemistry, Geophysics, Geosystems,* 9.

MAMANI, M., WÖRNER, G. & SEMPERE, T. 2010. Geochemical variations in igneous rocks of the Central Andean orocline (13 S to 18 S): tracing crustal thickening and magma generation through time and space. *Geological Society of America Bulletin,* 122.

MARTIN, E. E., MACDOUGALL, J., HERBERT, T., PAYTAN, A. & KASTNER, M. 1995. Strontium and neodymium isotopic analyses of marine barite separates. *Geochimica et Cosmochimica Acta,* 59**,** 1353-1361.

MCGEE, D., DONOHOE, A., MARSHALL, J. & FERREIRA, D. 2014. Changes in ITCZ location and cross-equatorial heat transport at the Last Glacial Maximum, Heinrich Stadial 1, and the mid-Holocene. *Earth and Planetary Science ….*

PARK, S.-H., LEE, S.-M., KAMENOV, G. D., KWON, S.-T. & LEE, K.-Y. 2010. Tracing the origin of subduction components beneath the South East rift in the Manus Basin, Papua New Guinea. *Chemical Geology,* 269**,** 339-349.

PAYTAN, A., KASTNER, M. & CHAVEZ, F. 1996. Glacial to Interglacial Fluctuations in Productivity in the Equatorial Pacific as Indicated by Marine Barite. *Science (New York, NY),* 274**,** 1355-1357.

PHILANDER, S. G. H., GU, D., LAMBERT, G. & LI, T. 1996. Why the ITCZ is mostly north of the equator. *Journal of ….*

PICHAT, S., ABOUCHAMI, W. & GALER, S. 2014. Lead isotopes in the Eastern Equatorial Pacific record Quaternary migration of the South Westerlies. *Earth and Planetary Science Letters,* 388.

RAO, W., CHEN, J., YANG, J., JI, J., LI, G. & TAN, H. 2008. Sr-Nd isotopic characteristics of eolian deposits in the Erdos Desert and Chinese Loess Plateau: Implications for their provenances. *Geochemical Journal,* 42**,** 273-282.

REA, D. K. 1994. The paleoclimatic record provided by eolian deposition in the deep sea: The geologic history of wind. *Reviews of Geophysics,* 32.

REEVES, J. M., BOSTOCK, H. C., AYLIFFE, L. K., BARROWS, T. T., DE DECKKER, P., DEVRIENDT, L. S., DUNBAR, G. B., DRYSDALE, R. N., FITZSIMMONS, K. E. & GAGAN, M. K. 2013. Palaeoenvironmental change in tropical Australasia over the last 30,000 years–a synthesis by the OZ-INTIMATE group. *Quaternary Science Reviews,* 74**,** 97-114.

RIND, D. & PERLWITZ, J. 2004. The response of the Hadley circulation to climate changes, past and future. *The Hadley Circulation: Present, Past and Future.* Springer.

SCHNEIDER, T., BISCHOFF, T. & HAUG, G. H. 2014. Migrations and dynamics of the intertropical convergence zone. *Nature,* 513.

SUN, J. & ZHU, X. 2010. Temporal variations in Pb isotopes and trace element concentrations within Chinese eolian deposits during the past 8Ma: Implications for provenance change. *Earth and Planetary Science Letters*.

TOGGWEILER, J. & SAMUELS, B. 1995. Effect of Drake Passage on the global thermohaline circulation. *Deep Sea Research Part I: Oceanographic Research Papers,* 42**,** 477-500.

VOIGT, I., CHIESSI, C. M., PRANGE, M., MULITZA, S., GROENEVELD, J., VARMA, V. & HENRICH, R. 2015. Holocene shifts of the southern westerlies across the South Atlantic. *Paleoceanography,* 30**,** 39-51.

WANG, Y. J., CHENG, H., EDWARDS, R. L., AN, Z. S. & WU, J. Y. 2001. A high-resolution absolute-dated late Pleistocene monsoon record from Hulu Cave, China. *Science*.

WANG, Y. X., YANG, J. D., CHEN, J., ZHANG, K. J. & RAO, W. B. 2007. The Sr and Nd isotopic variations of the Chinese Loess Plateau during the past 7 Ma: Implications for the East Asian winter monsoon and source areas of loess. *Palaeogeography Palaeoclimatology Palaeoecology,* 249**,** 351-361.

XIE, R. C. & MARCANTONIO, F. 2012. Deglacial dust provenance changes in the Eastern Equatorial Pacific and implications for ITCZ movement. *Earth and Planetary Science Letters.*

ZHANG, W. F., CHEN, J. & LI, G. J. 2015. Shifting material source of Chinese loess since similar to 2.7 Ma reflected by Sr isotopic composition. *Scientific Reports,* 5**,** 7.

ZIEGLER, C. L., MURRAY, R. W., PLANK, T. & HEMMING, S. R. 2008. Sources of Fe to the equatorial Pacific Ocean from the Holocene to Miocene. *Earth and Planetary Science Letters,* 270**,** 258-270.

3. THE PENULTIMATE GLACIAL TERMINATION AND LARGE MIGRATIONS OF THE PACIFIC INTERTROPICAL CONVERGENCE ZONE

3.1 Introduction

The Intertropical Convergence Zone (ITCZ) is a key component of tropical hydroclimate. It is associated with a zonally heterogeneous tropical precipitation maximum that affects the lives of billions across the globe. Knowing how the ITCZ responds to abrupt climate change is essential for reconstructing atmospheric circulation across climate transitions, as well as the role of the atmosphere in Southern Ocean ventilation. Here, we track the changes in the position of the ITCZ during the penultimate deglaciation by examining the Pb and Nd radiogenic isotope records of dust deposited in the central equatorial Pacific (CEP). Additionally, we quantify the relative contribution of potential dust source endmembers. We also extend the geographic sensitivity of previous work in CEP, using 5 cores across a seven-degree north-south transect. We find the southernmost position of the ITCZ during Termination II (between 136 and 131 kyr), with a subsequent interglacial movement of more than 7° north.

The annual mean position of the ITCZ changes depending on the location of maximum insolation and the thermal equator (McGee et al., 2014, Schneider et al., 2014). Both models and paleoclimate reconstructions (Reimi and Marcantonio, 2016, Arbuszewski et al., 2013, Jacobel et al., 2016) agree that the ITCZ migrates on climate timescales, but without much agreement about the magnitude of the migration. This model-observation disparity could be due to proxies that have varying sensitivities to different aspects of the ITCZ system (McGee et al., 2018). The response of the ITCZ to changes in latitudinal thermal gradient, either due to insolation changes or anthropogenic climate change, is critical to our understanding of atmosphere-ocean couplings

and tropical hydrosphere dynamics. A southern ITCZ shift is part of the hypothesized mechanism that translates the collapse of the northern hemisphere ice sheets into a global climate termination (Chiang and Bitz, 2005, Chiang and Friedman, 2012). The ITCZ is connected to the southern hemisphere subtropical jets and westerly winds, which may exert control on Southern Ocean upwelling and ventilation during the deglaciation (Anderson and Carr, 2010).

Traditionally, the paleo-ITCZ migration has been tracked by looking at precipitation reconstructions in the speleothem record (Wang et al., 2001), changes in river discharge (Peterson and Haug, 2006), or changing oceanic salinity and temperature gradients (Koutavas and Lynch-Stieglitz, 2004). Tracking the ITCZ by constraining dust provenance changes allows us to isolate the unique effect of atmospheric circulation. We can track the changes in ITCZ position by looking at spatial variations in the dust provenance over time. Here, we rely on the Pb and Nd isotope ratios of the dust-containing-fraction of the sediments (Fig. S1), which capture the heterogeneity of northern and southern hemisphere derived dust (Mamani et al., 2008, Wang et al., 2007, Gaiero et al., 2007). This approach was previously successfully applied to ITCZ migration changes in the CEP during the last 30kyr BP (Reimi and Marcantonio, 2016) at Termination I, but this study is the first to be able to resolve the provenance changes during a stadial event at Termination II.

Other studies have looked at latitudinal changes in dust provenance (Xie and Marcantonio, 2012, Pichat et al., 2014) or flux (McGee et al., 2014) in the Pacific Ocean, but little work has focused on the CEP, with the current literature centered around the LGM (Reimi and Marcantonio, 2016) or only the dust flux (Jacobel et al., 2017). Here, we attempt to extend our understanding of ITCZ behavior to the penultimate deglaciation. We find that these changes

in provenance are linked to shifts in the ITCZ that are coincident with changes in global climate at Termination II and, likely, northern hemisphere Heinrich Stadial event 11 (HS11).

3.2 Abrupt changes in dust provenance and ITCZ shifts

Boreal summer insolation changes do not account for the full range of temperatures across glacial/interglacial boundaries during late Pleistocene climate transitions. Rather, orbital changes in precession lead to enhanced Northern Hemisphere summer insolation which, under the right conditions, start a series of positive feedbacks that culminate in a climate termination (Denton et al., 2010). The migration of the ITCZ is a potentially strong mechanism for translating high-latitude climate change into the tropics. Thus, reconstructing paleo-ITCZ shifts can provide significant information about changes in hemispheric symmetry, and the strength of the thermal gradient (Schneider et al., 2014).

The Sanbao cave record from ~110 to 160 kyr BP shows that the strength of the Asian Monsoon tracks northern hemisphere summer insolation (Cheng et al., 2009). However, around termination II, the northern hemisphere summer insolation begins to rise and the Asian Monsoon weakens abruptly during the so-called Weak Monson Interval (WMI-II) (Cheng et al., 2006) (Fig. 3.1a). The WMI-II (~136 to 129 kyr) is consistent with the timing of North Atlantic cooling during HS11. During the WMI-II, the Nd isotope ratios of the dust component of sediments in core 17PC (at 0.48°N) show a pronounced change of more than 2 ε_{Nd} units to a more negative Nd isotopic composition (more unradiogenic), which we interpret as a significant increase in northern hemisphere dust sources. Specifically, this -2.5 ε_{Nd} unit shift suggests a shift of the ITCZ to its southernmost position (i.e., south of 0.48°N) between 136 and 131 kyr, consistent with the timing of HS11 (Fig. 3.1d). In the North Atlantic, during HS11 (~136 to 129 kyr),

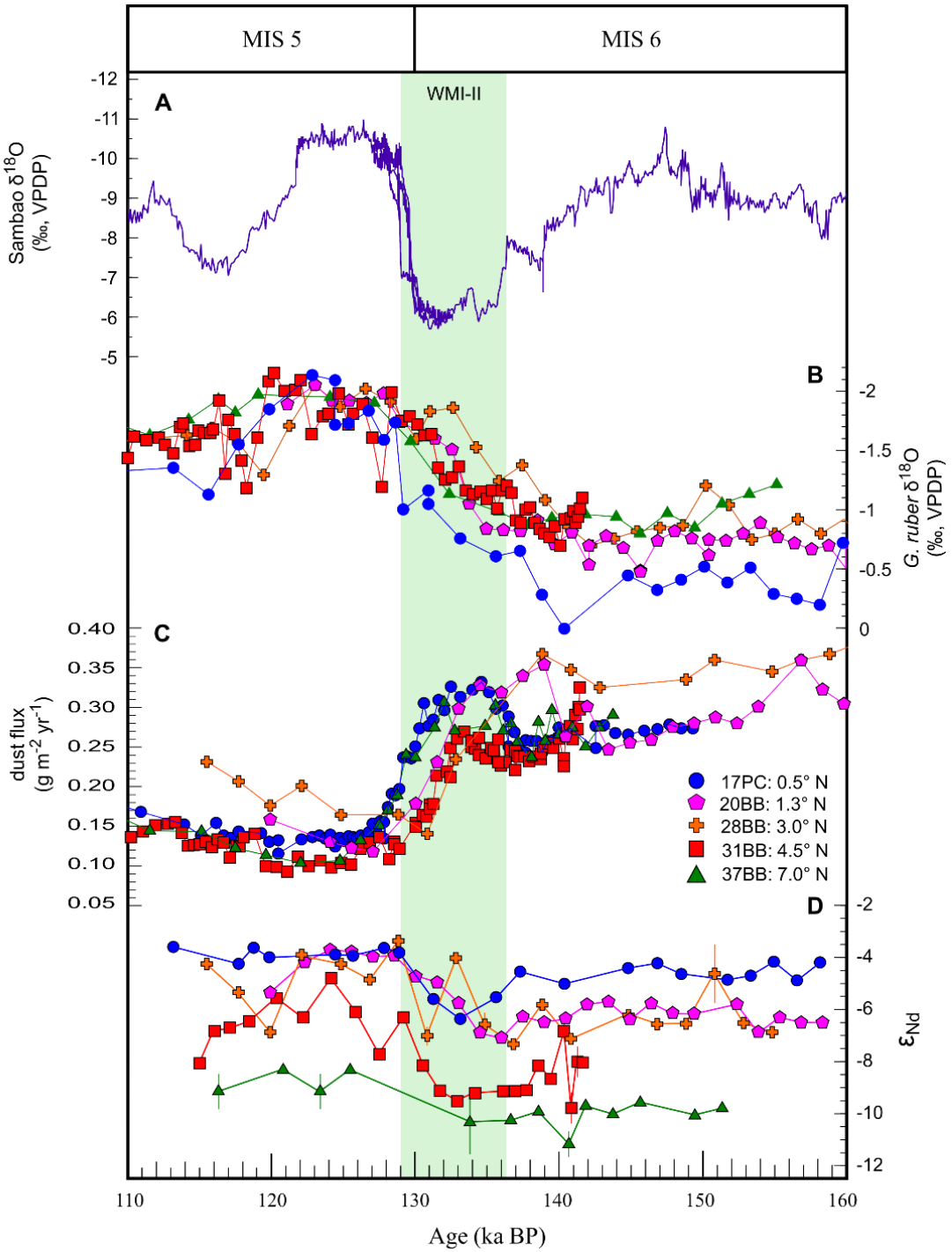

Figure 3.1 Dust provenance, flux and precipitation. The oxygen isotope data for cores 17PC, 31BB and 37BB are from ref. 31, while the dust flux for those same cores are from ref. 5. **a.** Sanbao cave $\delta^{18}O$ time series (light purple)(Wang et al., 2008, Cheng et al., 2009) **b.** *G. ruber* $\delta^{18}O$ stratigraphy (17PC--0.5° N, blue circles; 20BB--1.3° N, pink pentagons; 28BB--3.0 ° N, orange crosses; 31BB--4.5° N, red squares; and 37BB--7° N, green triangles). **c.** ^{230}Th-normalized-^{232}Th flux, a proxy for dust flux. Symbols as in panel b. **d**. Nd isotope ratios, expressed as ε_{Nd}. Symbols as in panel b. Green shading represents Weak Monsoon Interval II (WMI-II)(Denton et al., 2010) correlated with HS11 in the North Atlantic.

a freshwater pulse from the initial breakup of the Laurentide Ice Sheet (McManus et al., 2004, Broecker et al., 1992) may have caused the Atlantic Overturning Meridional Circulation (AMOC) to slow down which, in turn, reduces the heat flux into the Northern Hemisphere. At the same time, there is evidence from Antarctica's Epica Dome C (Lambert et al., 2008) core that the SH experienced a temperature rise.

The anti-phasing of NH-SH temperature during glacial and deglacial periods is a also knows as the bipolar seesaw (Marino et al., 2015). Our interpretation of the Nd isotope record of dust in equatorial core 17PC suggests that an abrupt stadial climate change event during the penultimate termination (i.e., HS11), which is linked to changes in global ocean circulation (i.e., AMOC reduction), is also connected to changes in atmospheric circulation (i.e., migration of the ITCZ southwards by at least 7°).

Despite its tropical location, the CEP also experiences large glacial-interglacial temperature differences, as indicated by the *G. ruber* $\delta^{18}O$ record which shows steadily lower $\delta^{18}O$ values beginning during MIS 6 and more pronounced in all cores across HS11 (Fig. 3.1b). Dust flux to all sites almost halved between glacial and interglacial periods (Fig. 3.1c), with the site closest to the equator (17PC) experiencing the largest increase in dust flux during HS11 (Jacobel et al., 2016). This dust flux increase is distinct from the EPICA Dome C dust flux (Lambert et al., 2008), which suggests a decoupling between dust fluxes to Antarctica (i.e., southern hemisphere sources) and those to the CEP at this time (Jacobel et al., 2016).

3.3 Possible dust sources to the CEP

The combined Pb and Nd isotope data provide an opportunity to quantify the changes in dust provenance and assigning possible endmembers associated with northern hemisphere (Asian Loess; Nakai et al., 1993) or southern hemisphere sources (i.e. South American volcanics; Pichat

et al., 2014) (Fig. 2). At the CEP sites, around Termination II, we can see a clear meridional gradient in the Nd isotopes (Fig. 3.1d, Fig. 3.2): the most northern core, 37BB (at 7.04° N), has the most radiogenic Nd values with an average εNd value of -9.5. The three middle cores (31BB, 4.5°N; 28BB, 3.0°N; and 20BB, 1.3°N) all reflect intermediate εNd (average values of -7.7, -5.7, and –5.6, respectively). The southernmost core, 17PC (at 0.48° N), has an average εNd value of -4.4. At a first approximation, this reflects a consistent latitudinal change in dust provenance between the northern hemisphere source (Asian loess, ε_{Nd} from ~-10 to -12 value) (Zhang et al., Wang et al., 2007) and the southern hemisphere source (South American volcanics, ε_{Nd} range from ~ 0 to -8) (Mamani et al., 2008, Gaiero et al., 2007). However, there is some ambiguity in deciphering dust source using only Nd isotopes because the N CVZ source has relatively negative Nd isotope ratios that approach those of Asian Loess (Fig. 3.1d). A two isotope plot (Nd in conjunction with Pb isotope ratios) reduces the ambiguity and allows us to account for the relative contribution of dust from variable southern hemisphere sources (Gaiero et al., 2007) and the Asian source (Fig. 3.2).

We have built a semi-quantitative mixing model to determine the percentages of dust contributions from different sources. We have created two independent ternary diagrams based on four assumed endmember (EM) sources (EM 1 to EM 4). (For a discussion of these endmembers, please see methods section). These endmembers are helpful in parsing the temporal and spatial variations within our data, and they were selected to maximize the number of data points inside the ternary system. EM 1-3 are within the range of the three most likely South American sources, SVZ, S CVZ and N CVZ, respectively (Mamani et al., 2008, Mamani et al., 2010, Pichat et al., 2014, Gaiero et al., 2007). EM 4 is closely linked to Asian Loess, more

radiogenic with respect to Pb than the average Asian Loess values (Fig. 3), but within the range of published Asian Loess data (Wang et al., 2007, Zhang et al., 2015)(Fig. 3).

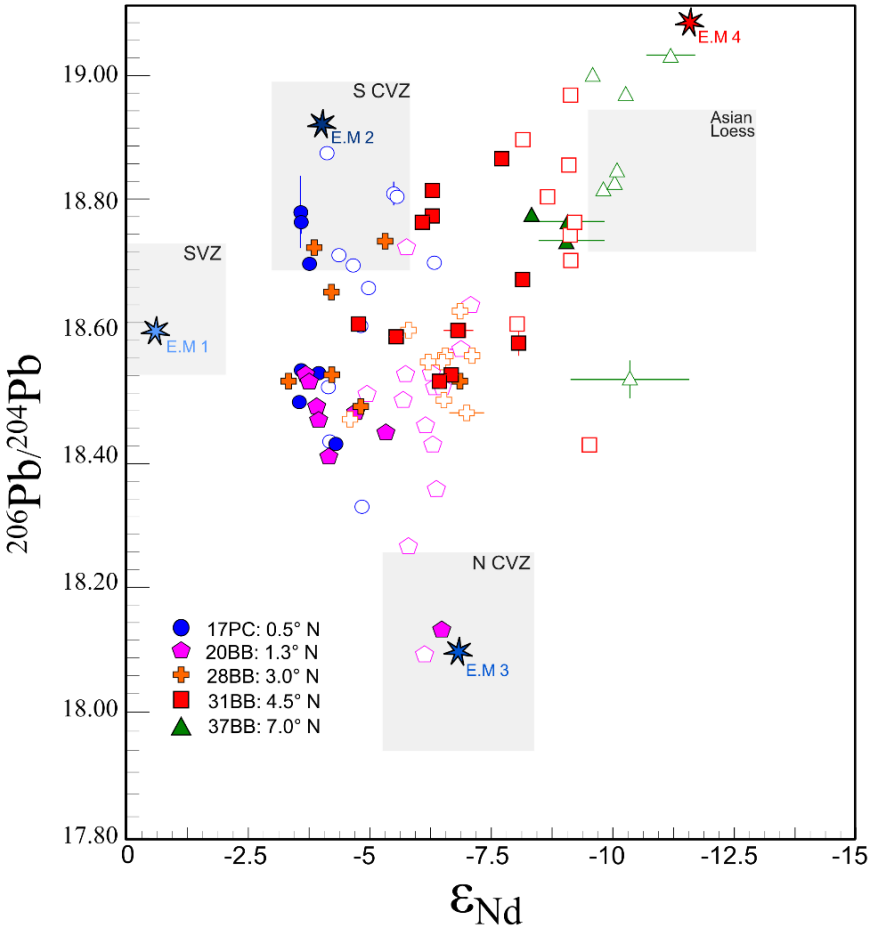

Figure 3.2 Pb vs Nd record at MIS 6 and MIS 5. $^{206}Pb/^{204}Pb$ versus εNd for all sites (17PC--0.5° N, blue circles; 20BB--1.3° N, pink pentagons; 28BB--3.0 ° N, orange crosses; 31BB--4.5° N, red squares; and 37BB--7° N, green triangles). The error bars represent standard errors. Filled symbols are interglacial samples (MIS 5), and open symbols are glacial samples (MIS 6). Relevant possible dust sources are marked by shaded grey areas. The S-CVZ and N-CVZ Pb and Nd isotope ranges are from ref. 28, the SVZ Pb isotope range is based on ref. 17, SVZ Nd range is from ref. 15; the Pb isotope range for Asian loess is from ref. 27, Nd isotope range for Asian Loess is from ref. 14. Endmembers 1-4 are shown with colored stars, E.M 1 (light blue) is most like SVZ, E.M 2 is most like S CVZ (dark blue), E.M 3 is most like N CVZ (blue), E.M (red) is most like Asian Loess.

The more southern cores (28BB, 3.0°N; 20BB, 1.3°N; and 17PC, 0.48°N) have variable Nd and Pb isotope ratios that are consistent with a mostly South American dust provenance (Fig. 3.2). The range of Nd and Pb isotope values can be largely explained by a three-component mixing system of dust from different South American sources, ranging from Northern Peru to Patagonia (northern central volcanic zone, N CVZ; southern central volcanic zone, S CVZ; and southern volcanic zone, SVZ (Mamani et al., 2008, Mamani et al., 2010, Pichat et al., 2014)). The isotope ratios of the northernmost core (37BB, 7.0°N) and the glacial component of 31BB, on the other hand, seem to be dominated by a dust fraction with an Asian loess provenance. Furthermore, it appears that during interglacial MIS 5, a significant fraction of dust from southern hemisphere sources also reaches site 31BB (4.5°N).

3.4 Beyond provenance: Quantifying dust fluxes

Glacial times are globally more dusty than interglacial times, but this increased dustiness is not distributed homogenously around the globe (Mahowald et al., 2006). It is therefore not possible to make inferences about dust provenance using dust flux proxies alone without independently constraining the dust flux within each hemisphere (Jacobel et al., 2016). However, this requires the assumption of a relatively uniform transport within each hemisphere. In particular, ice-core-derived dust fluxes do not necessarily translate directly to low latitude sites, because there is sub-continental heterogeneity in dust sources, even on continental scales (Pichat et al., 2014). Using dust provenance, however, it is possible to quantify the contributions of different regions, while also decoupling dust flux from dust provenance. The importance of this decoupling is clear once we combine our dust provenance interpretations with the dust flux record (Jacobel et al., 2016) (Fig. 3.3).

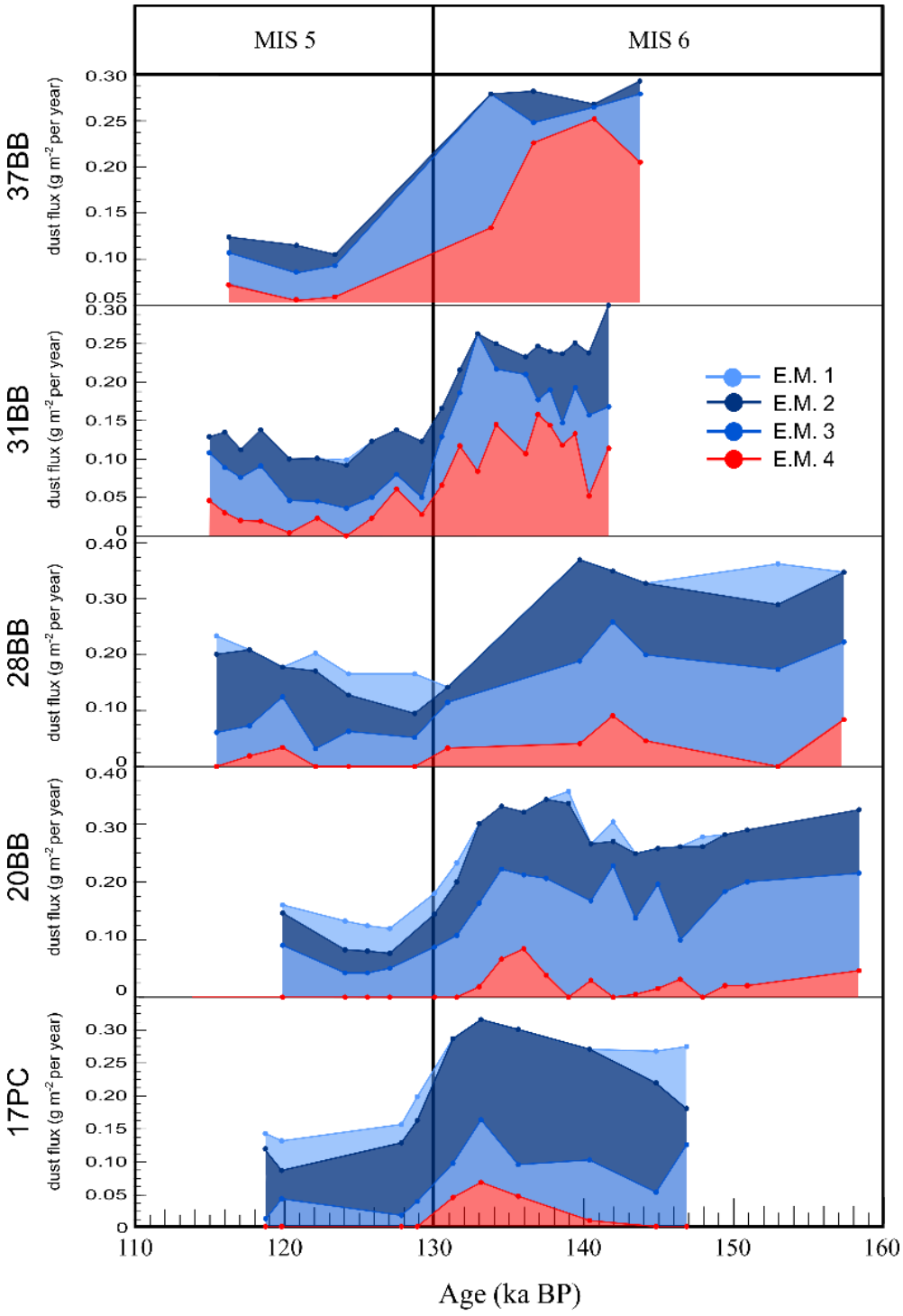

Figure 3.3 End-member contributions to dust flux. ^{230}Th-normalized-^{232}Th flux over time, as shaded by the percentage endmember characterization for each sample containing both Pb and Nd isotope data (see supplementary table 1). E.M 1 (light blue) is most like SVZ, E.M 2 is most like S CVZ (dark blue), E.M 3 is most like N CVZ (blue), E.M (red) is most like Asian Loess (see also Fig. 3.2).

Our ^{230}Th-derived ^{232}Th fluxes (^{232}Th is a proxy for dust flux in the CEP[17]) for 5 CEP cores are shown in Fig. 3.1c. In addition to the high-resolution dust flux profiles already published for 17PC, 31BB, 37BB (Reimi and Marcantonio, 2016), we present new dust flux data for 20BB and 28BB (Fig. 3.1c). By combining measured dust flux with the quantitative estimates of each endmember, we can determine the dust flux contribution of each endmember (Fig. 3.3). This allows us to isolate and examine both changes in dust flux and dust provenance. There is a remarkable similarity in the dust fluxes across all five cores, where MIS 6 is nearly two times dustier than MIS 5 (Fig. 3.1c), which agrees with model estimates (Mahowald et al., 2011).

However, the increase in dust flux during MIS 6 is not a consequence, exclusively, of northern-sourced dust. The three most southern sites (17PC-28BB), show that most of the increase in dust flux is linked to an increase in southern hemisphere endmembers. In addition, site 37BB shows an increase in the relative proportion of southern hemisphere dust sources shortly before TII (Fig. 3.3). Attributing the increased dust flux solely to an increase in dust delivered from a northern source to the southern cores would overestimate the northern hemisphere contribution, and risks overestimating the southern migration of the ITCZ.

3.5 Tracking the changes in ITCZ position over time

Analysis of Nd and Pb isotopes, $^{230}Th_{xs,o}$-normalized ^{232}Th fluxes, planktonic oxygen isotope data (Fig. 3.1, Fig. S1), and previously published work on these sites (Jacobel et al., 2016, Lynch-Stieglitz et al., 2015) allow us to interpret ITCZ movements during the penultimate transition from full glacial to interglacial conditions. We suggest a total ITCZ migration of 3° south during HS11, with the total glacial-interglacial range between 5-7° between MIS 6 and MIS 5. This exceeds the modeled estimates (McGee et al., 2014, Donohoe et al., 2013), but agrees with similar data-driven estimates for the glacial/interglacial changes observed during

termination I and shorter timescales (Reimi and Marcantonio, 2016, Arbuszewski et al., 2013, Sachs et al., 2009).

A close examination of the spatial and temporal changes in radiogenic isotopes at all sites between 110 and 160 kyrs shows that the ITCZ is migrating actively at glacial-interglacial timescales, but also responds to shorter stadial events such as HS11 (Fig. 3.4). During MIS6 (~155 kyr) we attribute the radiogenic Pb and the non-radiogenic Nd signal at site 37BB as being dominated by dust derived from an Asian loess source (Zhang et al., 2015), suggesting an ITCZ position south of 7.04 °N (Fig. 3.4). At ~146 kyr the planktonic foram oxygen isotope data suggest possible lower salinity conditions north of 17PC. Core 28BB shows the lowest $\delta^{18}O$ signal, potentially narrowing down the position of the ITCZ to near 2.97 °N, as the ITCZ is associated with increased precipitation (though it is difficult to separate oxygen-isotope salinity from temperature effects; Fig. 3.1b). Between ~146 and 136 kyr, site 28BB shows an increase to more radiogenic Pb isotope ratios and a decrease in ε_{Nd} values, which we interpret as an increase in the amount of Asian dust at this time. Quantitatively, EM 4 (Asian source) can explain only about 26% of this signal (Fig. 3), but in light of an increase in dust flux across all cores, we interpret this as a southern migration of the ITCZ to between 2.97 and 1.27 °N (Fig. 3.4).

At the onset of HS11 (between ~136 and 135 kyr), a pronounced increased in dust flux to site 17PC, as well as the lack of similar dust increases in the EDC core (Fig. 3.1d-f), was interpreted as an increase in northern hemisphere dust to site 17PC (Jacobel et al., 2016). Our radiogenic isotope data concur with this interpretation, such that during the same time interval, the detrital material at 17PC (at 0.48 °N) shows more nonradiogenic Nd and radiogenic Pb isotope ratios (ε_{Nd} = -6.34, $^{206}Pb/^{208}Pb$ = 18.810 at 131 kyr). The ε_{Nd} values are 2.5 ε_{Nd} units more

non-radiogenic than the interglacial average for 17PC, suggesting that there is a significant increase in northern-sourced (Asian loess) dust.

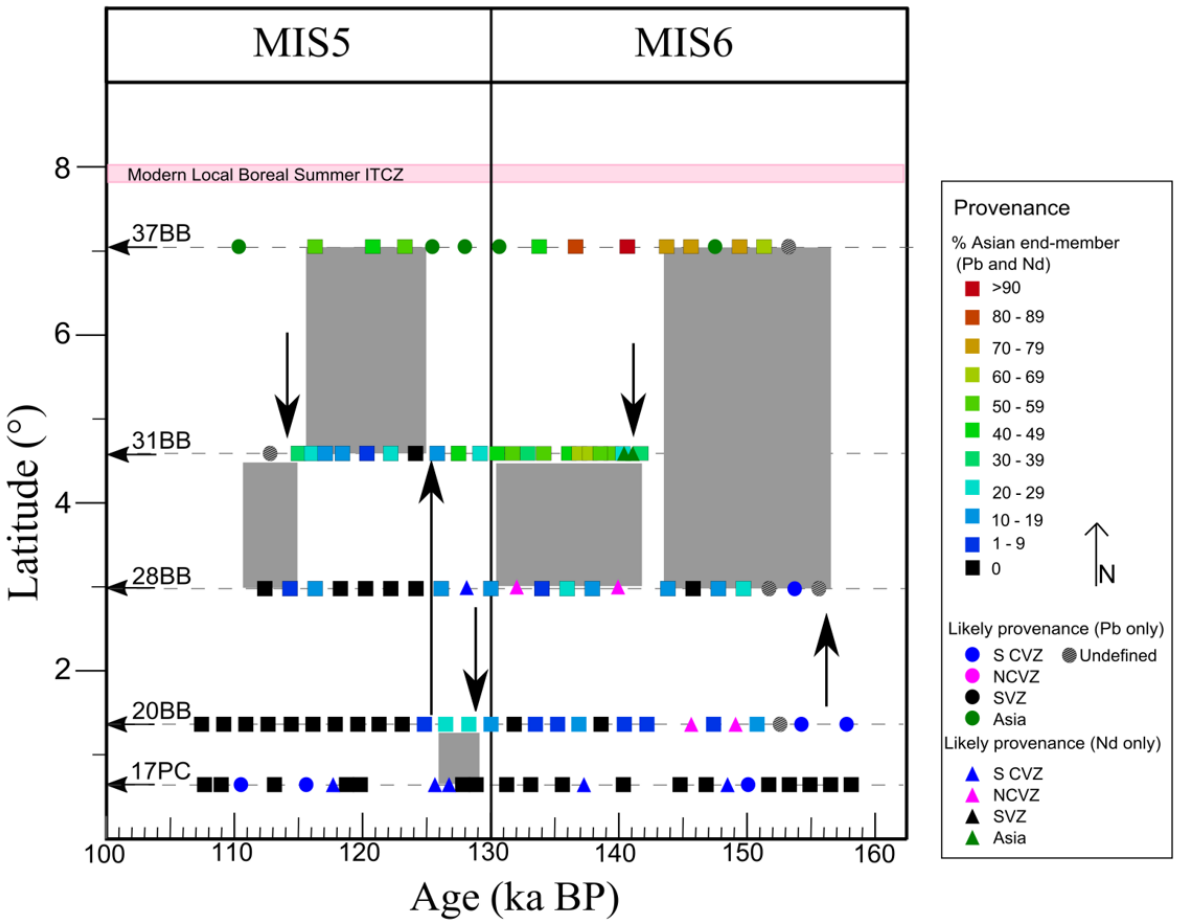

Figure 3.4 Interpretation of ITCZ migration over time. Interpretation of ITCZ location over time. All data points are marked along the dashed lines representing the core latitude. Samples for which there are only Nd data are represented by triangles. Samples for which there are only Pb data are represented by circles. Samples for which there is both Pb and Nd data is represented by squares. Each square is shaded on a gradient depending on the percentage contribution of E.M. 4 (Asian-like provenance) as seen in the figure "Provenance" legend. When only one isotope system is available (either Nd or Pb), data has been shaded according to the most likely provenance as follows: Asian Loess (green), N-CVZ (pink), S-CVZ (blue), SVZ (black). If the most likely provenance could not be determined (due to overlapping signals of potential source areas), the data was marked as undefined (shaded graded grey). The top pink line indicates the modern annual mean location of modern ITCZ over the CEP, as recorded by the local annual maximum precipitation in the global precipitation climatology product (GCP) version 2.2 from NOAA. Shaded grey rectangles are schematic representations of the location of the ITCZ through time. Arrows represent relative displacement of the ITCZ during various climatic periods.

This southern migration represents a 5° shift in the position of the ITCZ from glacial to interglacial times, and nearly 8° relative to its modern boreal summer position (Adler et al., 2003). This ITCZ shift is also coincident with a southern migration of southern hemisphere westerlies seen in the EEP (Pichat et al., 2014). Indeed, based on our radiogenic isotope data, we see an increase in northern-sourced (EM 4) dust to the equator (17PC), suggesting that at times at least 18% of the dust at the equator was sourced from Asia. In core 20BB the increase in EM 4 dust happens earlier than in 17PC. This offset could be due to an increase in the influence of bioturbation in core 20BB, due to its slower sedimentation rate(Lynch-Stieglitz et al., 2015). Not all of the increase dust flux in 17PC can be attributed to northern hemisphere sources, and we suggest that during HS11 dust from South American sources was also supplied to this site in significantly higher amounts than during the preceding glacial or proceeding interglacial (Fig. 3.3). This agrees with work done farther east at the equator at site ODP849, in which Pichat et al.[16] argued that the large increase in dust flux at the equator during HS11 was evidence for an increased delivery of dust from a southern hemisphere source.

By 123 kyr, the ITCZ migrated rapidly to north of site 31BB (4.68 °N) (Fig. 3.4). During the interglacial period, the Nd signal for all cores is more radiogenic. However, the samples at core 37BB still carry a more dominant Asian loess signal (average $\varepsilon_{Nd} =$ -8.74, $^{206}Pb/^{204}Pb$ = 18.84), in agreement with published records that suggest a more northerly ITCZ position during interglacials (Reimi and Marcantonio, 2016, Arbuszewski et al., 2013, Yarincik et al., 2000). We suggest that the ITCZ remained between 7.04 and 4.68 °N from ~123 to 118 kyr, coinciding with the end of MIS 5e(Shackleton et al., 2003). At the start of MIS 5d (between ~118 and 114kyr), the ITCZ migrated further south to between 4.68 and 2.97 °N, as suggested by an increase in the

relative contribution of EM 4 seen in core 28BB (Fig. 3.3, Fig. 3.4). The ITCZ remains north of site 28BB (at 1.27 °N) until at least 110 kyr.

3.6 Methods

Stable isotopes. Stable isotope analyses of oxygen in *G. ruber* (white) specimens (250-355μm) were performed using a Thermo MAT253 with a Kiel IV individual acid bath device, housed at the Georgia Institute of Technology. Values were converted to Vienna Peedee belemnite (VPDB) via NBS-19 and an in-house standard, and NBS-18 values were monitored in each run. Replicate analyses of the in-house standard mixed in the sample runs yielded a 1 sigma standard deviation of 0.09‰ for $\delta^{18}O$.

Radiogenic isotope analysis. All work was performed in the clean laboratory of the Williams Radiogenic Isotope Geosciences Facility at Texas A&M University. The operationally-defined detrital fraction of the sediment was isolated by sequential leaching (Reimi and Marcantonio, 2016, Xie and Marcantonio, 2012). Sediments (<63μm) were dried down, then sequentially leached with 10% buffered acetic acid to a pH of 5 (carbonate removal), 0.02 M hydroxylamine hydrochloride with 25% acetic acid (authigenic mineral removal), and at 80°C in a water bath with 2M KOH (opal removal). The detrital fraction was digested twice in a mixture of concentrated HF:HNO_3 (5:2) at 120°C for two days, and dried down with aqua regia at 80°C once.

Pb was eluted on anion exchange (AG1X8, 200-400 mesh) columns. Nd was eluted, after being washed off of the Pb columns, through additional RE Spec (Eichrom) and Ln Spec (Eichrom) columns. Pb and Nd isotopes were analyzed by Thermal Ionization Mass Spectrometry (TIMS) at Texas A&M University.

Pb was loaded onto rhenium filaments with silica gel and was measured in static mode. The data has been corrected with a 0.1%/amu linear fractionation correction based on multiple runs of NIST981 Pb standard. The procedural Pb blank, analyzed with a ^{205}Pb spike, was found to be less than 50 pg, and no blank corrections on the measured ratios were necessary.

Nd was loaded onto rhenium filaments and measured in static mode as the Nd^+ ion. $^{143}Nd/^{144}Nd$ ratios were corrected for any Sm interference on mass 144 by monitoring mass 147. $^{143}Nd/^{144}Nd$ ratios were normalized to $^{146}Nd/^{144}Nd = 0.7219$. Standard JNdi-1 was run throughout this study and gave a mean value of $^{143}Nd/^{144}Nd = 0.5121009 \pm 6.6$ ppm (1σ, n= 67). No further corrections were made to the Nd data in this study. $^{143}Nd/^{144}Nd$ ratios in this study are expressed as ε_{Nd} values by normalizing to $(^{143}Nd/^{144}Nd)_{CHUR} = 0.512638$.

Age models. Age-depth relationships for cores MGL1208-20BB and 20BB were developed on the basis of planktonic oxygen isotope stratigraphy, with a linear interpolation between MIS boundary tie points based on the dates in the LR04 stack (Lisiecki and Raymo, 2005). The MGL1208-17PC, 31BB, 37BB age model followed previous work (Jacobel et al., 2016). Though they have independent time constraints, the timing for the increases in ^{232}Th flux for all the Line Island cores is coincidental, which suggests reasonably accurate age models.

Thorium analysis. Sediment samples from ML1208-20BB and 28BB were analyzed for uranium and thorium isotopes by isotope dilution and inductively coupled plasma mass spectrometry (ICP-MS) at Texas A&M University. We added a ^{236}U and ^{229}Th spike to each sediment sample (between 300 and 400 mg) prior to sediment dissolution and digestion with HNO_3, $HClO_4$ and HF. Anion-exchange column chemistry was also used to isolate the U and Th fractions.

Reproducibilities of uranium, ^{230}Th, and ^{232}Th analyses were 6% during the course of this study. We ran procedural blanks in each batch and yielding ^{238}U blanks (0.3 ng), ^{230}Th blanks (0.08 ng) and ^{232}Th blanks (3.6 ng), and no blank corrections were made. Our U and Th concentrations data are in agreement with respect to those produced for cores 17PC, 31BB, and 37BB previously (Jacobel et al., 2016) from another laboratory, and suggest accuracy of our results.

^{230}Th normalization. ^{232}Th fluxes were determined by normalizing to excess ^{230}Th concentrations(Francois et al., 2004, Anderson et al., 2006, Loveley et al., 2017, McGee et al., 2007). ^{232}Th is contained in terrestrial sediments at concentrations between 10-15 ppm over a wide range of provenance (McGee et al., 2007). Due to the isolation of our sites, we expect the detrital ^{232}Th to be entirely eolian in origin.

Quantitative Analysis of Potential Dust Sources. In order to represent the relative temporal variability of the dust provenance within our dataset we used multiple mixing lines between theorized potential end members. Each endmember is defined by their ^{206}Pb/^{204}Pb vs. ε_{Nd} values, as follows: Endmember 1, ^{206}Pb/^{204}Pb = 18.59 and ε_{Nd} = -0.63; endmember 2, ^{206}Pb/^{204}Pb = 18.91 and ε_{Nd} = -4.18; endmember 3, ^{206}Pb/^{204}Pb = 18.08=9 and ε_{Nd} = -7.13; endmember 4, ^{206}Pb/^{204}Pb = 19.07 and ε_{Nd} = -12.08. We created two separate tertiary mixing systems: one system included EM 1, EM 2, and EM 3, while the other included EM 2, EM 3, and EM 4. Each endmember is most closely associated with one of the four potential dust sources previously determined as the most likely contributors to CEP dust (Reimi and Marcantonio, 2016). The most relevant South American volcanic zones (Pichat et al., 2014) are the Central Volcanic Zone (CVZ), and the South Volcanic Zone (SVZ). Endmember 1 is most closely linked to the SVZ. The SVZ, which ranges in latitude from 33° S to 43° S, contains volcanics with the

following isotope systematics: $^{206}Pb/^{204}Pb$ = 18.5–18.7, $^{208}Pb/^{204}Pb$ = 38.3–38.6 (Mamani et al., 2008, Mamani et al., 2010), and ε_{Nd} -2–+2 (Gaiero et al., 2007). Endmember 2 is most closely linked to the S-CVZ, also known as the Antofalla domain. It lies between 22° S and 27.5° S, and has $^{206}Pb/^{204}Pb$ = 18.5–19.0, $^{208}Pb/^{204}Pb$ = 38.9–39.0, and ε_{Nd} -8–-2 (Mamani et al., 2008, Mamani et al., 2010). Endmember 3 is most linked to the N-CVZ and ranges in latitude from 16° S to 21 °S, with volcanics that have the following isotope characteristics: $^{206}Pb/^{204}Pb$ = 17.5–18.5, $^{208}Pb/^{204}Pb$ = 37.6–38.7, and ε_{Nd} -8.0–-5.5 (Mamani et al., 2008, Mamani et al., 2010). Endmember 4 is the only northern hemisphere endmember and linked to a radiogenic variant of Asian Loess that has $^{206}Pb/^{204}Pb$ = 18.8–19.1, $^{208}Pb/^{204}Pb$ = 39–39.2 (Sun and Zhu, 2010), and ε_{Nd} = -12 to -8 (Wang et al., 2007, Rao et al., 2008, Zhang et al., 2015).

3.7 References

ADLER, R. F., HUFFMAN, G. J., CHANG, A., FERRARO, R., XIE, P.-P., JANOWIAK, J., RUDOLF, B., SCHNEIDER, U., CURTIS, S. & BOLVIN, D. 2003. The version-2 global precipitation climatology project (GPCP) monthly precipitation analysis (1979-present). *Journal of hydrometeorology,* 4.

ANDERSON, R., FLEISHER, M. & LAO, Y. 2006. Glacial–interglacial variability in the delivery of dust to the central equatorial Pacific Ocean. *Earth and Planetary Science Letters,* 242**,** 406-414.

ANDERSON, R. F. & CARR, M.-E. 2010. Uncorking the Southern Ocean's vintage CO2. *Science,* 328**,** 1117-1118.

ARBUSZEWSKI, J. A., CLÉROUX, C., BRADTMILLER, L. & MIX, A. 2013. Meridional shifts of the Atlantic intertropical convergence zone since the Last Glacial Maximum. *Nature Geoscience*.

BROECKER, W., BOND, G., KLAS, M., CLARK, E. & MCMANUS, J. 1992. Origin of the northern Atlantic's Heinrich events. *Climate Dynamics,* 6**,** 265-273.

CHENG, H., EDWARDS, R. L., BROECKER, W. S., DENTON, G. H., KONG, X., WANG, Y., ZHANG, R. & WANG, X. 2009. Ice age terminations. *science,* 326**,** 248-252.

CHENG, H., EDWARDS, R. L., WANG, Y., KONG, X., MING, Y., KELLY, M. J., WANG, X., GALLUP, C. D. & LIU, W. 2006. A penultimate glacial monsoon record from Hulu Cave and two-phase glacial terminations. *Geology,* 34**,** 217-220.

CHIANG, J. C. & BITZ, C. M. 2005. Influence of high latitude ice cover on the marine Intertropical Convergence Zone. *Climate Dynamics,* 25**,** 477-496.

CHIANG, J. C. & FRIEDMAN, A. R. 2012. Extratropical Cooling, Interhemispheric Thermal Gradients, and Tropical Climate Change. *Annual Review of Earth and Planetary Sciences,* 40**,** 383-412.

DENTON, G. H., ANDERSON, R. F., TOGGWEILER, J., EDWARDS, R., SCHAEFER, J. & PUTNAM, A. 2010. The last glacial termination. *Science,* 328**,** 1652-1656.

DONOHOE, A., MARSHALL, J., FERREIRA, D. & MCGEE, D. 2013. The relationship between ITCZ location and cross-equatorial atmospheric heat transport: From the seasonal cycle to the Last Glacial Maximum. *Journal of Climate,* 26.

FRANCOIS, R., FRANK, M., VAN DER LOEFF, M. M. & BACON, M. P. 2004. 230Th normalization: An essential tool for interpreting sedimentary fluxes during the late Quaternary. *Paleoceanography,* 19.

GAIERO, D. M., BRUNET, F., PROBST, J.-L. & DEPETRIS, P. J. 2007. A uniform isotopic and chemical signature of dust exported from Patagonia: Rock sources and occurrence in southern environments. *Chemical Geology,* 238**,** 107-120.

JACOBEL, A. W., MCMANUS, J., ANDERSON, R. & WINCKLER, G. 2016. Large deglacial shifts of the Pacific Intertropical Convergence Zone. *Nature Communications,* 7.

JACOBEL, A. W., MCMANUS, J. F., ANDERSON, R. F. & WINCKLER, G. 2017. Climate-related response of dust flux to the central equatorial Pacific over the past 150 kyr. *Earth and Planetary Science Letters,* 457**,** 160-172.

KOUTAVAS, A. & LYNCH-STIEGLITZ, J. 2004. Variability of the marine ITCZ over the eastern Pacific during the past 30,000 years. *The Hadley Circulation: Present, Past and Future.* Springer.

LAMBERT, F., DELMONTE, B., PETIT, J.-R., BIGLER, M., KAUFMANN, P. R., HUTTERLI, M. A., STOCKER, T. F., RUTH, U., STEFFENSEN, J. P. & MAGGI, V. 2008. Dust-climate couplings over the past 800,000 years from the EPICA Dome C ice core. *Nature,* 452**,** 616-619.

LISIECKI, L. E. & RAYMO, M. E. 2005. A Pliocene-Pleistocene stack of 57 globally distributed benthic δ18O records. *Paleoceanography,* 20.

LOVELEY, M., MARCANTONIO, F., WISLER, M., HERTZBERG, J., SCHMIDT, M. & LYLE, M. 2017. Millenial-scale iron fertilization of the eastern equatorial Pacific over the past 100,000 years. *Nature Geoscience*.

LYNCH-STIEGLITZ, J., POLISSAR, P. J., JACOBEL, A. W., HOVAN, S. A., POCKALNY, R. A., LYLE, M., MURRAY, R. W., RAVELO, C. A., BOVA, S. C., DUNLEA, A. G., FORD, H. L., HERTZBERG, J. E., WERTMAN, C. A., MALONEY, A. E.,

SHACKFORD, J. K., WEJNERT, K. & XIE, R. C. 2015. Glacial-interglacial changes in central tropical Pacific surface seawater property gradients. *Paleoceanography,* 30**,** 423-438.

MAHOWALD, N., ALBANI, S., ENGELSTAEDTER, S., WINCKLER, G. & GOMAN, M. 2011. Model insight into glacial–interglacial paleodust records. *Quaternary Science Reviews,* 30**,** 832-854.

MAHOWALD, N. M., YOSHIOKA, M., COLLINS, W. D., CONLEY, A. J., FILLMORE, D. W. & COLEMAN, D. B. 2006. Climate response and radiative forcing from mineral aerosols during the last glacial maximum, pre-industrial, current and doubled-carbon dioxide climates. *Geophysical Research Letters,* 33.

MAMANI, M., TASSARA, A. & WÖRNER, G. 2008. Composition and structural control of crustal domains in the central Andes. *Geochemistry, Geophysics, Geosystems,* 9.

MAMANI, M., WÖRNER, G. & SEMPERE, T. 2010. Geochemical variations in igneous rocks of the Central Andean orocline (13 S to 18 S): tracing crustal thickening and magma generation through time and space. *Geological Society of America Bulletin,* 122.

MARINO, G., ROHLING, E., RODRÍGUEZ-SANZ, L., GRANT, K., HESLOP, D., ROBERTS, A., STANFORD, J. & YU, J. 2015. Bipolar seesaw control on last interglacial sea level. *Nature,* 522**,** 197-201.

MCGEE, D., DONOHOE, A., MARSHALL, J. & FERREIRA, D. 2014. Changes in ITCZ location and cross-equatorial heat transport at the Last Glacial Maximum, Heinrich Stadial 1, and the mid-Holocene. *Earth and Planetary Science ….*

MCGEE, D., MARCANTONIO, F. & LYNCH-STIEGLITZ, J. 2007. Deglacial changes in dust flux in the eastern equatorial Pacific. *Earth and Planetary Science Letters,* 257.

MCGEE, D., MORENO-CHAMARRO, E., GREEN, B., MARSHALL, J., GALBRAITH, E. & BRADTMILLER, L. 2018. Hemispherically asymmetric trade wind changes as signatures of past ITCZ shifts. *Quaternary Science Reviews,* 180**,** 214-228.

MCMANUS, J. F., FRANCOIS, R., GHERARDI, J. M. M., KEIGWIN, L. D. & BROWN-LEGER, S. 2004. Collapse and rapid resumption of Atlantic meridional circulation linked to deglacial climate changes. *Nature,* 428**,** 834-837.

NAKAI, S. I., HALLIDAY, A. N. & REA, D. K. 1993. Provenance of dust in the Pacific Ocean. *Earth and Planetary Science Letters,* 119.

PETERSON, L. C. & HAUG, G. H. 2006. Variability in the mean latitude of the Atlantic Intertropical Convergence Zone as recorded by riverine input of sediments to the Cariaco Basin (Venezuela). *Palaeogeography*.

PICHAT, S., ABOUCHAMI, W. & GALER, S. 2014. Lead isotopes in the Eastern Equatorial Pacific record Quaternary migration of the South Westerlies. *Earth and Planetary Science Letters,* 388.

RAO, W., CHEN, J., YANG, J., JI, J., LI, G. & TAN, H. 2008. Sr-Nd isotopic characteristics of eolian deposits in the Erdos Desert and Chinese Loess Plateau: Implications for their provenances. *Geochemical Journal,* 42**,** 273-282.

REIMI, M. A. & MARCANTONIO, F. 2016. Constraints on the magnitude of the deglacial migration of the ITCZ in the Central Equatorial Pacific Ocean. *Earth and Planetary Science Letters,* 453**,** 1-8.

SACHS, J. P., SACHSE, D., SMITTENBERG, R. H. & ZHANG, Z. 2009. Southward movement of the Pacific intertropical convergence zone AD 1400–1850. *Nature …*.

SCHNEIDER, T., BISCHOFF, T. & HAUG, G. H. 2014. Migrations and dynamics of the intertropical convergence zone. *Nature,* 513.

SHACKLETON, N. J., SÁNCHEZ-GOÑI, M. F., PAILLER, D. & LANCELOT, Y. 2003. Marine isotope substage 5e and the Eemian interglacial. *Global and Planetary change,* 36**,** 151-155.

SUN, J. & ZHU, X. 2010. Temporal variations in Pb isotopes and trace element concentrations within Chinese eolian deposits during the past 8Ma: Implications for provenance change. *Earth and Planetary Science Letters*.

WANG, Y., CHENG, H., EDWARDS, R. L., KONG, X., SHAO, X., CHEN, S., WU, J., JIANG, X., WANG, X. & AN, Z. 2008. Millennial-and orbital-scale changes in the East Asian monsoon over the past 224,000 years. *nature,* 451**,** 1090.

WANG, Y. J., CHENG, H., EDWARDS, R. L., AN, Z. S. & WU, J. Y. 2001. A high-resolution absolute-dated late Pleistocene monsoon record from Hulu Cave, China. *Science*.

WANG, Y. X., YANG, J. D., CHEN, J., ZHANG, K. J. & RAO, W. B. 2007. The Sr and Nd isotopic variations of the Chinese Loess Plateau during the past 7 Ma: Implications for the East Asian winter monsoon and source areas of loess. *Palaeogeography Palaeoclimatology Palaeoecology,* 249**,** 351-361.

XIE, R. C. & MARCANTONIO, F. 2012. Deglacial dust provenance changes in the Eastern Equatorial Pacific and implications for ITCZ movement. *Earth and Planetary Science Letters*.

YARINCIK, K., MURRAY, R. & PETERSON, L. C. 2000. Climatically sensitive eolian and hemipelagic deposition in the Cariaco Basin, Venezuela, over the past 578,000 years: Results from Al/Ti and K/Al. *Paleoceanography,* 15**,** 210-228.

ZHANG, W. F., CHEN, J. & LI, G. J. 2015. Shifting material source of Chinese loess since similar to 2.7 Ma reflected by Sr isotopic composition. *Scientific Reports,* 5**,** 7.

4. NEODYMIUM ISOTOPE RADIOGENIC ENRICHMENT IN AUTHIGENIC PHASES AS A FUNCTION OF BOTTOM WATER VENTILATION STRENGTH IN THE CENTRAL EQUATORIAL PACIFIC OCEAN

4.1 Introduction

The Nd isotopic composition of modern seawater reflects the quasi-conservative behavior of Nd during the mixing of large water masses (Tachikawa et al., 2017, van de Flierdt et al., 2016, Lacan et al., 2012). Heterogenous inputs of Nd into the ocean and the relatively short residence time of Nd in water (500-700 years; Tachikawa et al. 2017, Tachikawa et al., 2003), relative to the ocean mixing time (1500 years; Broecker and Peng 1982), have supported the use of Nd isotopes as a water mass tracer (Frank, 2002, Goldstein and Hemming, 2003, Lacan et al., 2012). The ocean's Nd isotope signature is generally derived from the heterogenous weathering inputs of the surrounding continents, transferred via rivers and wind (Tachikawa et al., 2017, Lacan et al., 2012), which can be subsequently modified by non-conservative behaviors (Lacan and Jeandel, 2005, Haley et al., 2017, Johannesson and Burdige, 2007). The $^{143}Nd/^{144}Nd$ signature of continental material depends on its crystallization history and age. Essentially older crystalline rocks have the lowest $^{143}Nd/^{144}Nd$ ratios (unradiogenic values), and younger volcanic rocks have higher, more radiogenic, $^{143}Nd/^{144}Nd$ ratios (Jacobsen and Wasserburg, 1980). Neodymium isotopes are expressed as ε_{Nd} (parts per ten thousand deviations from the bulk Earth values $^{143}Nd/^{144}Nd = 0.512638$; (Jacobsen and Wasserburg, 1980).

ε_{Nd} ratios in modern ocean water appear to behave quasi-conservatively (Tachikawa et al., 2003), even though Nd concentrations increase with depth in water column, exhibiting a "nutrient-like" profile. This decoupling between the behavior of Nd isotope composition and

concentration is known as the "Nd paradox" (Goldstein and Hemming, 2003, Arsouze et al., 2009, Jones et al., 2008). Modelled reconstructions of the oceanic Nd cycle, cannot reproduce modern distributions of oceanic ε_{Nd} ratios without additional inputs of Nd to the ocean, and suggest that as much as 95% of the ocean Nd is unaccounted for (Arsouze et al., 2009, Jones et al., 2008). A possible Nd source is particle dissolution in the water column, as the particulate Nd flux to the ocean is much larger than the dissolved Nd inputs (Oelkers et al., 2011). Indeed, only a small percentage of this particulate load is needed to account for the "missing" Nd in the ocean (Jeandel and Oelkers, 2015). Some of the mechanisms that have been proposed to account for the disparities between ε_{Nd} ratios and dissolved Nd concentrations are: boundary exchange of Nd at the continental margins (Lacan and Jeandel, 2005, Jeandel, 2016), submarine groundwater discharge of Nd at the continental margins (Johannesson and Burdige, 2007), or a benthic Nd flux to ocean bottom waters (Abbott et al., 2015a). These mechanisms, though different in delivery, reflect the modification of the signature of bottom water through sediment-water processes at boundaries, without changes in water mass mixing (Haley et al., 2017).

For accurate paleoceanographic reconstructions, ε_{Nd} ratios have to behave quasi-conservatively at a minimum, and proxy archives need to reflect the ε_{Nd} values of bottom water. Traditionally, the ε_{Nd} ratios of past bottom waters have been reconstructed using various sedimentary archives: fish teeth/debris (Martin and Scher, 2004), oxic coatings of foraminifera (Piotrowski et al., 2005), leaching of the Fe-Mn authigenic coatings of sediments (Frank, 2002), or corals (van de Flierdt et al., 2010). The variations in ε_{Nd} in these archives over time have been used successfully to trace changes in paleoceanographic circulation (Goldstein and Hemming, 2003, Piotrowski et al., 2012, Frank, 2002, Thomas et al., 2014). Unfortunately, several studies have recorded an offset between the ε_{Nd} ratios measured in modern bottom waters and those

recorded in two archives, Fe-Mn coatings (Du et al., 2016) and biogenic apatite (Horikawa et al., 2011). This feature is global, but Pacific basin studies tend to show the greatest bottom water to core-top ε_{Nd} offsets (Tachikawa et al., 2017, Haley et al., 2017). Additionally, recent work suggests that in locations with a high terrigenous input the recorded seawater signal in fish debris can be modified under varying redox conditions (Huck et al., 2016).

While only trace amounts of Nd are incorporated into living fish teeth (Shaw and Wasserburg, 1985), post-mortem uptake increases the concentrations from 100 to 1000 ppm (Elderfield and Pagett, 1986, Martin and Haley, 2000, Wright et al., 1984, Shaw and Wasserburg, 1985). Early work highlighted that the rare earth elements (REEs) in biogenic phosphates are derived from pore waters (Toyoda and Tokonami, 1990), and that diagenetic alteration of (REEs) in fossil biogenic apatites is common (Zhang et al., 2016). While fish debris have been shown to acquire their enhanced Nd concentrations during early diagenesis (Reynard et al., 1999, Staudigel et al., 1985), porewater alteration of the Nd isotope signal after burial is unlikely due to the extremely low concentration of Nd^{3+} in pore fluids (Martin and Haley, 2000, Martin and Scher, 2004). However, some sources of dissolved Nd to bottom waters and consequently porewaters may not reflect changes in water mass (Abbott et al., 2015a, Du et al., 2016, Jeandel, 2016), While this diagenetic alteration is complex, there are consistent rules that can aid in the interpretation of ε_{Nd} values as water mass tracers. Furthermore, the discrepancy between archival and expected bottom water ε_{Nd} ratios can be used to obtain new information about paleoceanographic conditions, such as exposure ages and current velocities (Haley et al., 2017).

Here, we compare reconstructions of the ε_{Nd} value of fossil fish debris and biogenic particle flux (Ba_{xs} flux) in the Central Equatorial Pacific (CEP) to a suite of other paleoclimate

proxy reconstructions determined in equatorial Line Islands cores (Jacobel et al., 2016, Jacobel et al., 2017a, Jacobel et al., 2017b, Costa et al., 2017, Reimi and Marcantonio, 2016, Reimi et al., in prep, Lynch-Stieglitz et al., 2015) over the past 125 kyrs. Our aim is to isolate the causes of the changes in ε_{Nd} ratios on glacial/interglacial scales to gain a better understanding of the geochemical cycling of Nd in the oceans which, in turn, is necessary for improved interpretations of past global climate and ocean circulation changes.

4.2 Distribution of Nd isotopes in the modern ocean

Globally, the Nd isotopic composition of ocean basins acts as a semi-quantitative tracer. The main cause for the distinct Nd isotope signal of each water mass is the global thermohaline overturning circulation. There is a general increase of deep-water ε_{Nd} along global circulation pathways that is caused by the mixing between young North Atlantic water with low εNd values (εNd = -10 to -14) and old Pacific water with more radiogenic εNd values (εNd = 0 to -5) (Tachikawa et al., 2017). The Indian and Southern Ocean reflect intermediate values as a result of the mixing of these two main sources (ε_{Nd} = -7 to -10) (Goldstein and Hemming, 2003). More locally, the lowest observed isotopic values are ε_{Nd} = -26.6 in Baffin Bay (Stordal and Wasserburg, 1986). The most radiogenic values have been measured in the Eastern Equatorial Pacific ε_{Nd} = + 2.7 (Grasse et al., 2012), due to its abundant and young volcanic material. These regional offsets are due to local or regional detrital inputs, which can complicate global Nd isotope interpretations, but can provide valuable information about local processes.

In the Pacific Ocean, deep-water ε_{Nd} trends can be broken down further, i.e., the South Pacific is less radiogenic than the North Pacific. The average ε_{Nd} ratio in the South Pacific is about -8 (between 60° S and 20° S), while the average of values in the North Pacific is about -4 (between 0 and 70° N). This reflects a mixing envelope between two endmembers, colder and

more oxygen-rich Southern Ocean water with an ε_{Nd} of -8, and an older and more oxygen-poor northern- and equatorial-sourced waters with an ε_{Nd} of -4. In the Central Equatorial Pacific, waters near Hawaii have been identified as a radiogenic outlier from the wider Pacific basin (Tachikawa et al., 2017).

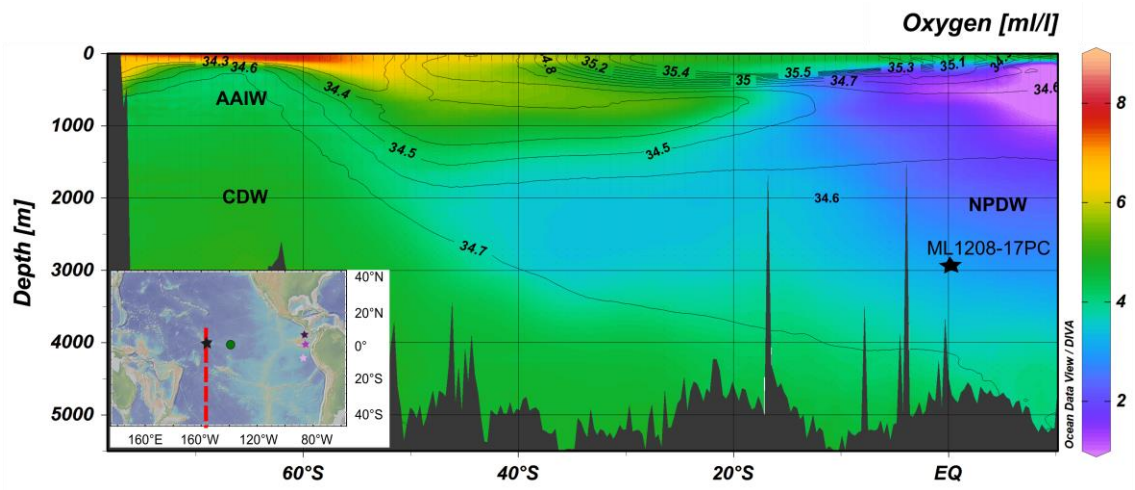

Figure 4.1 Dissolved oxygen and salinity at 160 °W. Distribution of modern dissolved oxygen in ml/L (Garcia et al., 2014) and salinity (Zweng et al., 2013) vs. depth along a meridional transect at 160° W (red dashed line). Basemap made with Ocean Data View (Schlitzer, 2015). Inset map made with GeoMapApp (Ryan et al., 2009), showing the location of sites in this study. Black star: ML1208-17PC (this study). Green circle: TT013-PC72 (green circle -- Winckler et al., 2016, Murray et al., 2000). Dark purple star: MV1014-1MC and 6MC (This study). Purple star: 09MC, 16MC (this study), and MV1014-02-17JC (Loveley et al., 2017). Light purple star: MV1014-20MC (this study). Sites ML1208-13BB and ML1208-20BB (Costa et al., 2017), also mentioned in this study, are near the black star. See Table 4.1 and appendix C for location and water depth details of all sites mentioned here.

At site ML1208-17PC (Fig. 4.1, Table 4.1), the main source of bottom water at 2900 m is the oxygen-poor North Pacific Deep Water (NPDW). NPDW is a modified Lower Circumpolar Deep Water (LCDW) diffusively upwelled in the North Pacific and modified by an admixture of Upper Circumpolar Water (UCDW) near the Hawaiian Islands. NPDW can be readily recognized from LCDW because of its lower oxygen concentrations (Kawabe and Fujio, 2010). The average ε_{Nd} value of NPDW is -4.3 ± 1.2 (n=82) (Tachikawa et al., 2017). Circumpolar

Deep Water (CDW), which is younger and more oxygenated, flows to the central Pacific from the south (Kawabe and Fujio, 2010), and has an average ε_{Nd} of -7.8 ± 1.2 and a salinity of 34.7‰ (Tachikawa et al., 2017).

4.3 Materials and Methods

4.3.1 Site and sampling

This study uses samples from cores collected in May 2012 during cruise MGL1208 aboard the R/V Margus G. Langseth. Sediment cores were collected from the central section of the Line Islands volcanic archipelago of the central equatorial Pacific Ocean, located south of the Hawaiian Islands (Lynch-Stieglitz et al., 2015). We focused on sediment samples for core ML1208-17PC (0.48 °M, 156° W; 2960m; hereafter 17PC). The estimated sedimentation rate at this site at the MIS 3/4 boundary is 3.0 cm/kyr. The core was sampled at 4-cm intervals allowing for a maximum temporal resolution of approximately one sample every 1000 years for Ba flux, and a varying temporal resolution between 1000 and 5000 years for fish debris ε_{Nd} ratios. Sediments consisted of foraminiferal oozes with low quantities of organic and terrigenous material. The age model used in this study is from Jacobel et al (2017). It was tuned to the LR04 benthic stack (Lisiecki and Raymo, 2005).

4.3.2 Nd isotopes measurements

Fish debris (bones and teeth) fragments were hand-picked from the >63 μm sediment fraction. Between ~20 and 30 fragments per sample were picked depending on sample size and availability. Fish debris samples were then sonicated in ethanol and cleaned using Milli-Q water three times before being digested. A reductive cleaning step was not used as oxide coatings record the same Nd isotopic as biogenic apatite (Huck et al., 2016, Thomas et al., 2014, Hague et al., 2012, Martin et al., 2010). The dissolved samples were run through RE Spec cation exchange

columns to separate the rare earth elements, followed by LN-Spec columns to isolate the neodymium (e.g. Reimi and Marcantonio, 2015, Xie et al. 2014).

Fifteen sequentially leached bulk sediments samples (<63μm fraction) were analyzed for their Nd isotope ratios. This leaching method followed the method outlined in Reimi and Marcantonio (2016), Reimi et al. (in prep) and Xie and Marcantonio (2012). In short, the <63μm of sediment was sieved with MQ water. The sediments were then subjected to sequential acetic acid, hydroxylamine hydroxide, and potassium hydroxide leaches. The residual material was fully digested in a mix of HNO_3:HF (2:5 v/v). The dissolved samples were run through Eichrom Pb spec columns, followed by RE spec and Ln Spec to isolate the Nd fraction.

Neodymium isotope ratios were analyzed as Nd^+ on a Triton Thermal Ionization Mass Spec (TIMS) in the R. Ken Williams Radiogenic Isotope Geosciences Laboratory at Texas A&M University. $^{143}Nd/^{144}Nd$ ratios were corrected for Sm interference and normalized to $^{146}Nd/^{144}Nd = 0.7219$ to correct for fractionation. Reproducibility of the Nd standard, JNd-1, during the course of this study gave mean values of $^{143}Nd/^{144}Nd = 0.52121009 \pm 6.6$ppm ($2\sigma$, n = 67), within error of accepted values, so that no corrections were made to the data. Our analytical procedural blanks were always less than 0.20 pg of Nd, making blank corrections unnecessary.

4.3.3 Barium measurements

For core ML1208-17PC, Ba concentrations were measured on 40 bulk sediment samples at Texas A&M. Approximately 50 mg of homogenized bulk sample were digested with HF, HNO_3, and $HClO_4$ acids. After evaporation to a soluble salt, the samples were re-dissolved and diluted in 2% HNO_3. Ba concentrations were measured via Inductively-Coupled Plasma Mass Spec (ICP-MS), and replicate measurements of the NIST 2702 standard yielded accurate results

within 5% accuracy. Procedural blanks of less than 1% were measured, and the average reproducibility of Ba concentrations in the samples was <7%.

4.4 Results

4.4.1 Fish debris data

The ε_{Nd} signatures of fish debris ($\varepsilon_{Nd\text{-}FD}$) at 17PC are presented in Fig. 4.1 and in Table 4.2. The average $\varepsilon_{Nd\text{-}FD}$ ratio measured at this site is -3.28 ± 1.1, about 1 ε_{Nd} unit more radiogenic than the average composition of modern NPDW (Tachikawa et al., 2017). The $\varepsilon_{Nd\text{-}FD}$ ratio of most of the samples through time fall within the NPDW envelope (Tachikawa et al., 2017), but lie on the higher side of the envelope. The most radiogenic sample has a Nd isotopic composition of -1.2 at 60 kyr. There is no dominant long-term trend differentiating glacial from interglacial periods (Marine oxygen Isotope Stages, MIS 1- 5). The MIS periods with the least $\varepsilon_{Nd\text{-}FD}$ variability are MIS 1 and MIS 3 with average $\varepsilon_{Nd\text{-}FD}$ values of -3.2 ± 0.5 and -3.5 ± 0.2 respectively. The most variability is seen at MIS 5 with an average $\varepsilon_{Nd\text{-}FD}$ = -3.3 ± 1.7. Several samples show a remarkable degree of Nd radiogenic enrichment at 26.6 kyr, 60 kyr, and 79 kyr. The least radiogenic ε_{Nd} value is recorded at the MIS 6/MIS 5 boundary ($\varepsilon_{Nd\text{-}FD}$ = -7.2 ± 0.1) at about 130 kyr.

The core-top samples from the eastern equatorial Pacific (EEP) (Fig. 4.2) are presented in Table 4.3. There is a clear trend to less radiogenic values with depth in the water column. The shallowest and most radiogenic sample has a value $\varepsilon_{Nd\text{-}FD}$ = 0.3; while the deepest and least radiogenic sample has a $\varepsilon_{Nd\text{-}FD}$ = -3.4.

4.4.2 Barium data

Biogenic Ba, or excess Ba (Ba_{xs}), was calculated by subtracting the lithogenic fraction of Ba (estimated using ^{232}Th concentrations) from the total Ba (Ba_{tot}). The lithogenic fraction of Ba

is calculated from the assumed Ba/^{232}Th ratio in the continental crust multiplied by the measured ^{232}Th concentrations. We used 51.4 as the average Ba/Th ratio of the continental crust ratio (Taylor and McLennan, 1985) and the ^{232}Th concentrations as measured by Jacobel et al. (2016), Jacobel et al. (2017a). The biogenic Ba flux (Ba_{xs} flux) was subsequently calculated using the mass accumulation rate derived from the ^{230}Th-derived mass accumulation rate (Jacobel et al., 2017b, Jacobel et al., 2016).

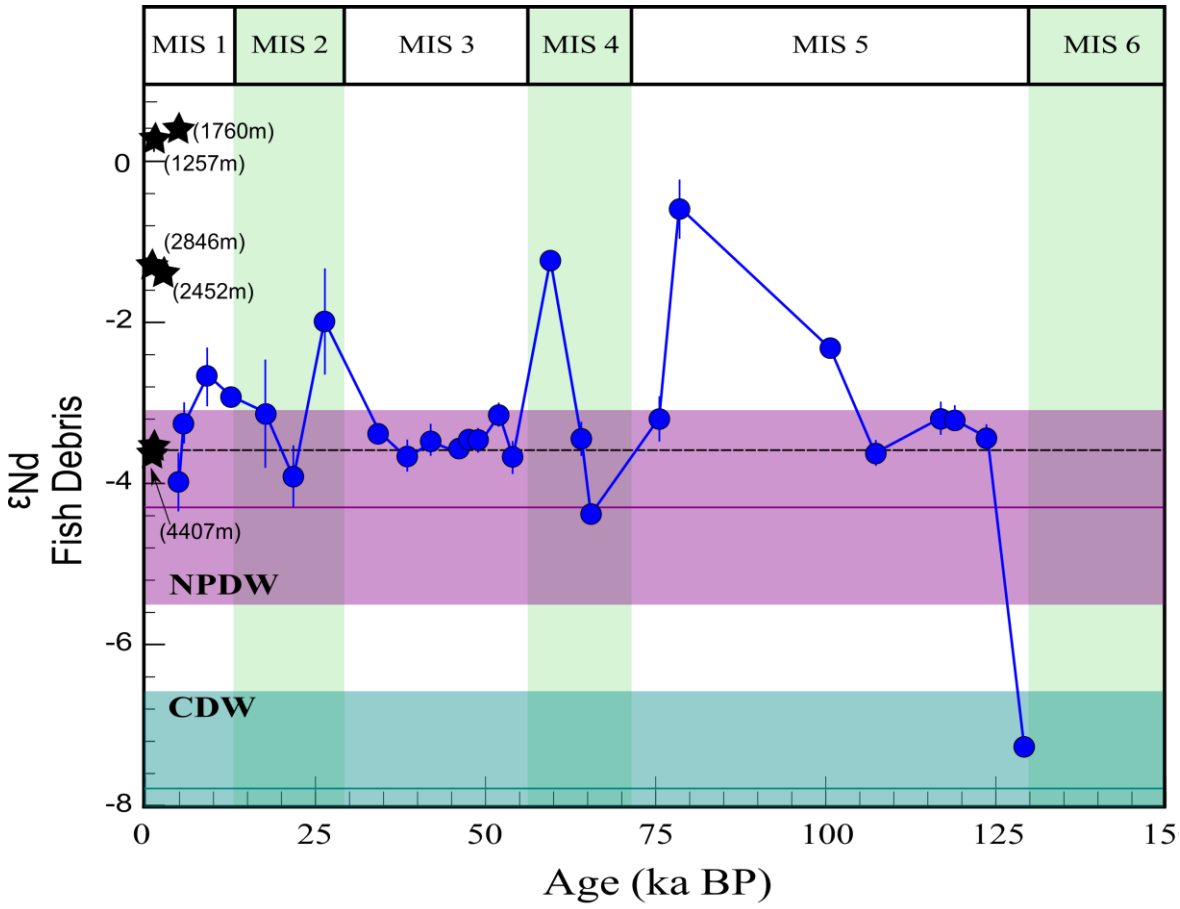

Figure 4.2 Neodymium isotopic record for ML1208-17PC. Nd isotopic record for core Ml1208-17PC, showing the ε_{Nd} value ranges for the modern composition of North Pacific Deep Water (NPDW – pink) and Circumpolar Deep Water (CDW – teal) (Tachikawa et al., 2017). Light green bars show the glacial MIS. Errors are 2-σ standard error. The black stars are core-top ε_{Nd} values (This study), core top ages (Marcantonio et al., 2014), core-top for 20MC (at 4407m) estimated from Horikawa et al. (2006). The black dashed line reflects the average NPDW value calculated by Fröllje et al. (2016) for the central North Pacific below 2000m depth (see section 5.1).

The Ba concentrations range from 305 to 670 ppm (Appendix C) Biogenic Ba makes up greater than 97% of the total Ba. Ba_{xs} flux accumulation rates range from 0.5 to 1.1 mg cm^{-2} kyr^{-1} (Fig. 4.2).

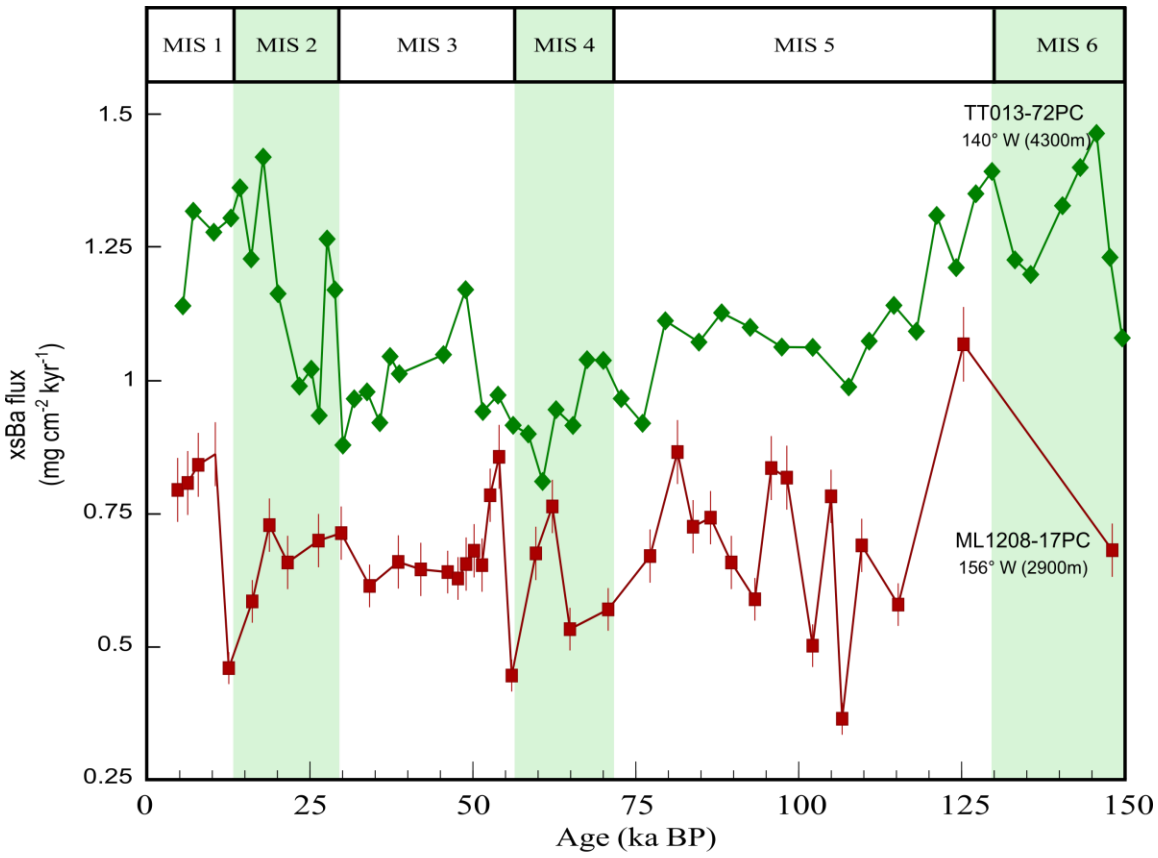

Figure 4.3 Excess barium over time. Ba_{xs} flux for core ML1208-17PC (red-this study). For core TT013-PC72 (green line) Ba_{xs} flux was calculated from published Ba concentration data (Murray et al., 2000) and ^{232}Th thorium flux (Winckler et al., 2016, Marcantonio et al., 2001).

4.5 Discussion

4.5.1 Holocene fish debris and modern seawater

At 2960 m, Site 17PC is bathed in the lower part of south-flowing NPDW (Fig. 4.1). NPDW is not homogenous vertically or horizontally with respect to εNd (Amakawa et al., 2009).

Surface waters are generally more radiogenic than deeper waters, but show a large degree of heterogeneity (εNd = -5.4 to -1.8, Piepgras and Jacobsen, 1988, Amakawa et al., 2009, Pahnke et al., 2012, Zimmermann et al., 2009), with values as high as ε_{Nd} = -1.4 to 0.8 reported for surface water near Hawaii (Fröllje et al., 2016, Vance et al., 2004). Given the dependency of ε_{Nd} on water depth, it is critical to have values with which to compare at 3km. Unfortunately, such studies are absent in the CEP. Indeed, only a few studies have described the distribution of Nd isotopes at depth in the Pacific Ocean (Piepgras and Jacobsen, 1992, Piepgras and Wasserburg, 1982, Shimizu et al., 1994, Lacan and Jeandel, 2001, Amakawa et al., 2004, Vance et al., 2004, Grasse et al., 2012, Carter et al., 2012, Amakawa et al., 2009, Fröllje et al., 2016).

There are no modern deepwater ε_{Nd} measurements from the Line Islands or nearby sites (Tachikawa et al., 2017). Meridionally, the nearest deepwater ε_{Nd} measurements have been made near Hawaii (ε_{Nd} of NPDW = -3.0 ± 0.4 at 3km, at 22.75° N, 158.00° W; (Fröllje et al., 2016), but concerns about the Nd isotopic enrichment of intermediate waters near Hawaii might not make this the best analog (Vance et al., 2004, Fröllje et al., 2016). Zonally, the nearest equatorial NPDW measurements at 3 km depth are closer to continents (Grasse et al., 2012), and may, therefore, experience a greater degree of boundary effects (Lacan and Jeandel, 2005), discussed further below. The calculated average of the ε_{Nd} ratio of NPDW below 1900m for sites in the central North Pacific (between 20°N and 30°N) is -3.5 ± 0.5 (n = 15) (Fröllje et al., 2016). Though this value is more radiogenic than the one defined by Tachikawa et al. (2017) of -4.3 ± 1.2 (n=82), estimated for waters below 1500m, it better reflects the bottom waters bathing our site (17PC).

The Holocene average at our site (ε_{Nd} = -3.2 ± 0.5) is in general agreement with the ε_{Nd} ratio of NPDW, although there is a 1.3 ε_{Nd} difference between the most radiogenic values during

the late Holocene and the least radiogenic values recorded at the top of the core (Fig. 4.2.). This radiogenic enrichment and the other larger enrichments we observe in sediment intervals deposited earlier cannot be explained through simple mixing between the two bottom water sources in the Pacific, as the ε_{Nd} for LCDW is even less radiogenic than NPDW (ε_{Nd} = -8.5; (Stichel et al., 2012a).

4.5.2 Differences between archival and bottom water ε_{Nd}.

Globally, archival ε_{Nd} has been observed to have a radiogenic offset relative to measured seawater neodymium (Tachikawa et al., 2017, Haley et al., 2017). Throughout the Pacific, there is a consistent difference between the ε_{Nd} values extracted from both foraminifera and fish debris in core-top studies and the measured ε_{Nd} ratios in seawater (Vance et al., 2004, Horikawa et al., 2011, Ehlert et al., 2013, Du et al., 2016). This difference is consistent enough to be more than a laboratory artifact. A direct comparison of core-top values and seawater profiles has been difficult in the Eastern Equatorial Pacific (EEP) due to the sparse nature of seawater profiles. Often these comparisons are done in sites that are too geographically distinct to draw precise contrasts (Horikawa et al., 2011).

Here, we compare our fish debris core-top record for the EEP at 85 °W with nearby seawater profiles measured by Grasse et al. (2012) at similar water depths (Fig. 4.4). The offset between our core-top and measured ε_{Nd} measurements is greater at higher water depths (1500-1700m) and less so at lower depths (4000m) (Fig. 4.4a). However, we show a consistent enrichment of core-top ε_{Nd} values relative to seawater ε_{Nd} (Fig. 4.4b), which suggests that archival ε_{Nd} values in the eastern equatorial Pacific does not faithfully record modern bottom water signals. This disagrees with previous comparisons in the EEP which showed only small offsets within uncertainty ranges (Horikawa et al., 2011, Hu et al., 2016b).

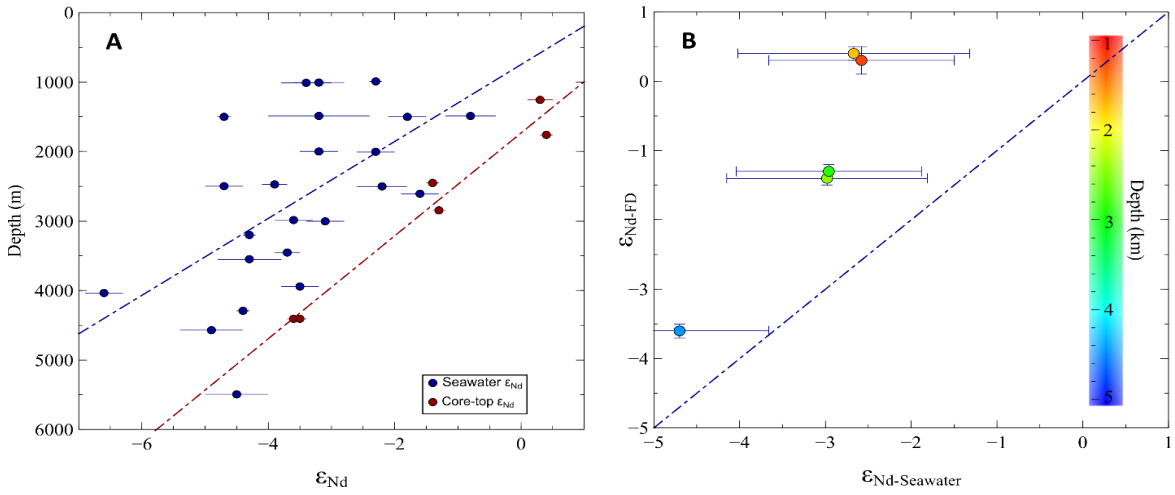

Figure 4.4 Comparison of ε_{Nd} values from core-top fossil fish debris and ambient seawater in the EEP. a. εNd changes with depth in seawater samples (dark blue -- Grasse et al. (2012)) and core-top fish debris (dark red – this study), error bars are 2σ. b. εNd in core-top fish debris against the εNd in seawater at a given depth (averaged for 400m sections), error bars are standard deviation, colors reflect the water depth of each core-top. 1:1 line in blue.

This interpretation agrees with other Pacific locations, where comparisons of ambient seawater and Holocene archives have shown that there is a consistent radiogenic enrichment in the archival measurements (Molina-Kescher et al., 2014, Horikawa et al., 2011, Hu et al., 2016b, Haley et al., 2017). One explanation for this variability could be the comparison of sites at slightly different depths and locations (Horikawa et al., 2011). However, our EEP offsets happen at sites in relatively close proximity (Fig. 4.1) and across similar depths (Fig. 4.4). In order to compare the ε_{Nd} of the seawater profiles, we averaged the signal for sites within a 300m window, so that the average water depth matched the water depth of the core-top. This follows the method for comparing ε_{Nd} in seawater and ε_{Nd} in core-tops from Horikawa et al. (2011). We also believe that the ε_{Nd} offset apparent in our EEP profile is not due to an integration of bottom water signals because of slow sedimentation rates and prolonged periods of deposition (Molina-Kescher et al., 2014). Here, the site with the slowest sedimentation rate MV104-20MC, at 8°S and 4200m depth

shows the best agreement with the seawater profile (Grasse et al., 2012), while more northern sites with faster sedimentation rates (Marcantonio et al., 2014) show more disagreement (Fig. 4).

The differences between archival and bottom water ε_{Nd} ratios do not seem to be uniformly distributed (Tachikawa et al., 2017), both at the basin (Horikawa et al., 2011) and global (van de Flierdt et al., 2016) scales. If the ε_{Nd} ratio in authigenic archives reflects the composition of pore waters instead of bottom waters (Du et al., 2016, Abbott et al., 2015b) then the difference between core-top and bottom-water ε_{Nd} will be affected by the magnitude of the benthic flux in the area (Haley et al., 2017), the exposure time of the bottom water to this flux (which depends on current velocities), and the reactivity and composition of detrital sediments (Du et al., 2016). This does not challenge the application of ε_{Nd} as a paleoceanography tool, but does require constraints on the non-conservative inputs to the ε_{Nd} signature. Pacific paleoceanographic studies have shown that when the radiogenic enrichment is small, it is possible to differentiate between southern- and northern-sourced water at depth, such that archival ε_{Nd} has been used throughout the Pacific to reconstruct late Pleistocene bottom water changes (Hu et al., 2016a, Hu et al., 2016b, Ehlert et al., 2013, Noble et al., 2013, Basak et al., 2010).

4.5.3 Water mass changes and the radiogenic enrichment of 17PC

Throughout the past 125 kyrs there are several periods of radiogenic enrichment at site 17PC, which at a first order do not seem to be connected to global cooling or warming, as they occur throughout the record in both glacial and interglacial climates (Fig. 4.1). The first and largest ε_{Nd} radiogenic enrichment event occurs during MIS 5 at 79 kyr, although the MIS 5 interval presented here is poorly sampled. There is also a slight enrichment event (relative to the NPDW ε_{Nd} ratio) at 100 kyr during MIS 5. Given the lack of resolution it is currently unclear if

the data demonstrate the persistence of a high ε_{Nd} signal at 17PC during MIS 5 or briefer ε_{Nd} incursions. All of the ε_{Nd} radiogenic enrichment events are outside of the range of modern values for both NPDW and LCDW and, therefore, do not represent a change in admixing between these two water masses. Below we will explore whether these changes are a product of changes in the composition of endmembers over the past 125 kyr.

In the Pacific, in particular, there remain unanswered questions about how NPDW acquires its distinct ε_{Nd} signal, and functions as an end-member in global ε_{Nd} based circulation models (Goldstein and Hemming, 2003), given that there is no deep-water formation in the north Pacific in modern times (Kawabe and Fujio, 2010). It is clear that NPDW develops an ε_{Nd} signature that is independent of traditional conservative water tracers (Haley et al., 2017).

The composition of LCDW reflects a mixing of NADW and NPDW in the Southern Ocean (Frank, 2002). Studies focusing in the North Atlantic basin have found a nearly constant ε_{Nd} signature of NADW through the mid-Pleistocene (van de Flierdt et al., 2006, Foster et al., 2007). Comparisons of ε_{Nd} values at depth in SW Pacific suggested an increase in the ε_{Nd} of LCDW by nearly 2 ε_{Nd} units at the LGM, while NPDW remained mostly unchanged (Hu et al., 2016a). Records from the South Pacific have suggested that LCDW experienced small changes in $\varepsilon_{Nd\text{-}FD}$ due to a reduced admixture from NADW in the central South Pacific (Molina-Kescher et al., 2016), and a reduced flux of NADW into the Southern Ocean in the SW Pacific during glacial times (Hu et al., 2016a, Elderfield et al., 2012, Noble et al., 2013). One potential caveat to these findings is that potential exchange with volcanogenic material was not addressed (Noble et al., 2013), despite the fact that the SW Pacific is a volcanically active location. This assertion was supported by a broader Pacific Ocean study in which it was determined that the ε_{Nd} signature of NPDW remained largely unchanged from the LGM to the Holocene (ε_{Nd} = -3 to -4; Hu et al.,

2016b). Although there are no archival records of the ε_{Nd} ratios for NPDW extending over 125 kyrs, we suggest that the bottom water signature of NPDW at site 17PC did not experience significant changes (Section 5.1).

Given that there is no evidence for a significant change to the composition of Pacific bottom-water endmembers throughout the last two glacial cycles, the enrichment events we observe likely reflect times during which Nd isotopes are recording a non-conservative behavior preserved in the $\varepsilon_{Nd\text{-}FD}$. In the following sections, we will examine the potential non-conservative influences on the radiogenic enrichment at 17PC, with emphasis on the particle-water interactions in the sediments (Abbott et al., 2016, Abbott et al., 2015a).

A "bottoms up" explanation to the Nd cycle explains why Nd concentrations and ε_{Nd} ratios can behave conservatively below the permanent thermocline in some situations, but act non-conservatively when exposed to a benthic flux (Abbott et al., 2015a). A benthic flux, which exchanges porewater ε_{Nd} with bottom water ε_{Nd}, will impact overlying bottom water, and may be carried laterally along isopycnals (Grasse et al., 2012, Singh et al., 2012, Abbott et al., 2015b). In the absence of a positive benthic flux (of either enriched or depleted Nd isotopes), both Nd and ε_{Nd} will behave conservatively (Haley et al., 2017). This would resolve model and observation inconsistencies of REE distributions in the Pacific Ocean (Jones et al., 2008, Arsouze et al., 2009). Abbott et al. (2015a) claim that the prominent radiogenic depletion of Nd with water depth in the Pacific Ocean (Lacan et al., 2012) can be explained by prolonged contact between bottom waters and a positive benthic flux.

4.5.4 Matters of particulate importance

In order to interpret variations in ε_{Nd} ratios in 17PC in the context of paleoclimate and paleoceanography, we first need to evaluate causes for the non-conservative behavior observed

in the CEP (Fig. 4.2). An important element to consider is the effect of water-particle interactions on the dissolved Nd isotopic signal (Arsouze et al., 2009, Jeandel, 2016). Aside from dust and riverine inputs, recent modelling work suggested that a major fraction of Nd enters the ocean through the sediment-seawater interface (Tachikawa et al., 2003, Arsouze et al., 2009, Rempfer et al., 2011). There, the potential for isotopic changes in bottom waters depends on the behavior of Nd isotopes in sediments. Non-conservative behaviors have been widely observed at the continental margins (Jeandel, 2016, Lacan and Jeandel, 2005), in waters with long residence times (Osborne et al., 2014), and in areas with large riverine inputs (Rousseau et al., 2015, Bayon et al., 2015, Stewart et al., 2016). Furthermore, reconstructions of water mass circulation changes using ε_{Nd} in a variety of marine sediment records show exceptional disparities at sites close to each other, which is difficult to justify if one assumes conservative behavior of Nd (Stumpf et al., 2010, Roberts and Piotrowski, 2015, Howe et al., 2016, Hu et al., 2016b). Additionally, basin-level studies have shown the potential for disparities between Holocene ε_{Nd} signatures in core-tops and those in present-day bottom waters (Horikawa et al., 2011).

Particle flux can impact the ε_{Nd} of bottom water, and therefore porewaters, if there is a lot of reversible particle scavenging. Through this mechanism, particles acquired the ε_{Nd} value of surface water but once deposited in sediments, Nd is desorbed leading to the isotopic enrichment of bottom water (Siddall et al., 2008), and subsequently pore waters through a benthic connection (Haley et al., 2017). In areas where the ε_{Nd} ratios in surface water are similar to the ε_{Nd} of bottom waters, like the Southern Ocean (Stichel et al., 2012b), particle flux has a lot potential to affect the ε_{Nd} of deep-waters. In the central Pacific, however, where the surface water ε_{Nd} is much more enriched than in the deep waters (Amakawa et al., 2009), an increase in the

particle flux that sinks through the water column and reaches the seafloor has the potential to affect the bottom water ε_{Nd} ratio (Abbott et al., 2015a).

In the following sections we examine the factors that account for the differences between $\varepsilon_{Nd\text{-}FD}$ and ε_{Nd} in bottom waters (see section 5.3), and try to explain the radiogenic enrichment events recorded at 17PC. We constrain changes in particle flux by examining both the lithogenic and biogenic fluxes, normalized using the ^{230}Th methodology (Section 5.4.1). We will also examine whether changes in the chemical composition of detrital inputs to the CEP have affected the $\varepsilon_{Nd\text{-}FD}$ values by looking at the changes in the provenance of detrital materials in the CEP (Section 5.4.2). Finally, we will present our $\varepsilon_{Nd\text{-}FD}$ data in relation to authigenic uranium records (aU) previously generated in the central and eastern Pacific (Jacobel et al., 2017b, Loveley et al., 2017, Winckler et al., 2016), which has been used as a proxy for the oxic conditions of pore waters. In so doing, we will address how bottom water exposure time to a benthic flux might affect $\varepsilon_{Nd\text{-}FD}$ (Section 5.5).

4.5.4.1 Biogenic and lithogenic particle fluxes in the CEP and their effect on εNd

Biogenic particles have been shown to adsorbed the ε_{Nd} of surface water (Akagi et al., 2014), and increases in biogenic flux in areas of high productivity have been hypothesized to affect the ε_{Nd} composition of bottom waters in the EEP (Grasse et al., 2012). In the CEP we will look at changes in biogenic flux as represented in excess Ba concentrations.

Organic matter can induce the precipitation of the mineral barite in the water column such that high barite concentrations are correlated with high organic matter content, such that barite is used as proxy of past productivity (Griffith and Paytan, 2012). We constrained the marine barite flux using Ba concentration measurements and correcting for detrital barium using a Ba/Th ratio of 51.4 (Taylor and McLennan, 1985) and the ^{232}Th concentrations measured at the

same depths (Jacobel et al., 2017a). The non-detrital Ba (Ba_{xs}) flux is assumed to be biogenic in nature and can be used for paleoceanographic reconstructions of past export production (Dymond et al., 1992), as has been applied previously in the equatorial Pacific as a productivity proxy (Costa et al., 2016, Murray et al., 1995). To calculate the flux of Ba_{xs}, we multiplied the Ba_{xs} data by the ^{230}Th-derived MARs for the same samples (Jacobel et al., 2017a). There is no issue with hydrodynamic biasing of the ^{230}Th MARs since deep-sea lateral advection at 17PC is virtually non-existent (Costa et al., 2016; Jacobel et al., 2016).

Our Ba_{xs} flux record (Fig. 4.3 & Fig. 4.5b) is compared to three other equatorial records of past productivity: a Ba_{xs} flux record from TT013-72PC (0.1°N, 139.4 °W, at 4300m depth, (Winckler et al., 2016), hereafter referred to as 72PC; Fig. 3), and two ^{231}Pa/^{230}Th records that cover the last 30 kyr at the Line Islands, one from ML1208 site 20BB (1.27° N and 157.26° W, 2850m water depth, Costa et al., 2017) and the other from ML1208 site 13BB (0.22° S and 155.96° W, 3049m water depth, Costa et al., 2017) (Fig. 4.5c). Previous work has shown that in the CEP Ba_{xs} flux and ^{231}Pa/^{230}Th are well correlated with each other and with changes in ocean productivity (Costa et al., 2016). As there are no other Ba_{xs} profiles in the CE, we present the ^{231}Pa/^{230}Th as a higher resolution comparison to our productivity record, allowing us to address carefully whether there is any correlation between changes in productivity (biogenic flux) and ε_{Nd} enrichment since the LGM.

Though the two Ba_{xs} fluxes (Fig. 4.3) (PC72 and 17PC) show slightly different high-frequency variations, the overall trends are similar, with higher productivity during warm interglacial times, and lower productivity during glacial times. Interestingly, site 72PC has consistently higher Ba_{xs} fluxes throughout the study periods. At a first glance this is incongruous, as nutrient supply for sites in the Equatorial Pacific is very homogenous (Winckler et al., 2008),

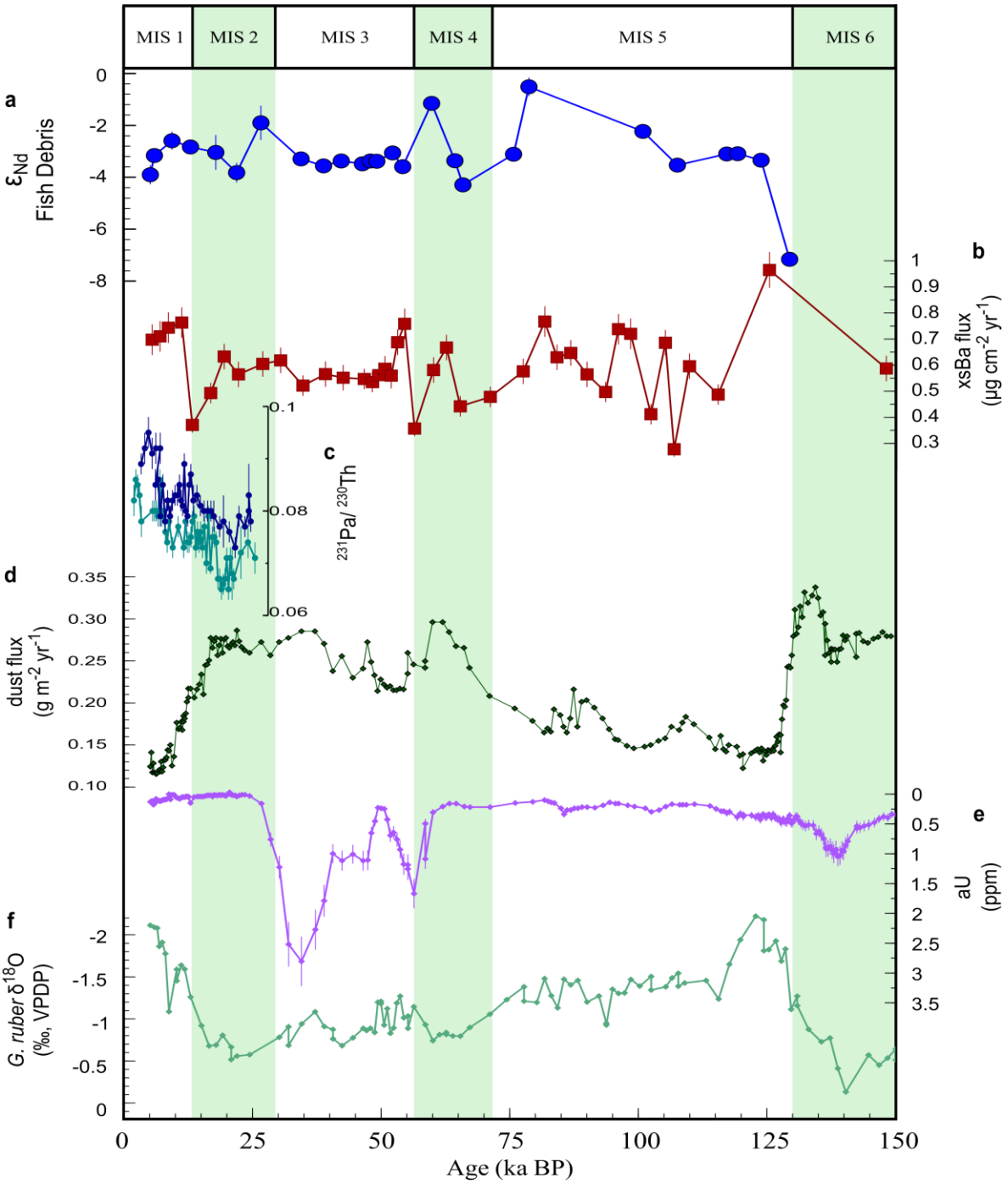

Figure 4.5 Local constrains on the Nd isotopic enrichment at site ML1208-17PC. a Neodymium isotopic record (blue circles). **b.** Ba_{xs} flux over time (red squares) **c.** $^{231}Pa/^{230}Th$ over the last 30 kyr for core ML1208-20BB (dark blue circles) at 1.27° N and 0.3 °S ML1208-13BB (teal circles) (Costa et al., 2017). **d** ^{230}Th-normalized-^{232}Th dust flux (dark green diamonds) (Jacobel et al., 2016, Jacobel et al., 2017a), see reference for errors. **e** authigenic Nd (pink line) (Jacobel et al., 2017b) **f.** oxygen isotope data for core ML1208-17PC (light green line) (Lynch-Stieglitz et al., 2015), see reference for analytical errors.

with both sites fed by the Equatorial Undercurrent, which is dominant in the equatorial surface water (Lacan and Jeandel, 2001). However, the likely explanation is that the magnitude difference is a product of water depth (Schenau et al., 2001, Von Breymann et al., 1992, Prakash Babu et al., 2002).

In the EEP, Grasse et al. (2012) suggested that the radiogenic enrichment seen in seawater samples at 2000 m depth was a consequence of reversible scavenging and a large flux of biogenic particles. In our records, an enrichment in $\varepsilon_{Nd\text{-}FD}$ which does occur during the Holocene (less than $2\varepsilon_{Nd}$ units) coincides with an Ba_{xs} flux peak, and a general increase in $^{231}Pa/^{230}Th$ (Fig. 4.5c). But, the other three $\varepsilon_{Nd\text{-}FD}$ enrichment events do not coincide with increases in Ba_{xs} flux. In addition, the peak in Ba_{xs} flux which coincides with MIS 5e –a pronounced $\delta^{18}O$ feature in the CEP (Fig. 4.5e)– is not related to any feature in the $\varepsilon_{Nd\text{-}FD}$ record (Fig. 4.5). Therefore, at site 17PC the non-conservative behavior of Nd, as recorded in $\varepsilon_{Nd\text{-}FD}$ ratios, is not likely caused by increases in productivity and the subsequent transfer of an enriched surface water signal (contained in an enhanced biogenic flux) to the bottom waters.

Nevertheless, it is still possible than in the EEP the radiogenic enrichment observed by Grasse et al. (2012) is indeed a consequence of the high particle flux, since sedimentation rates and productivity at 85 °W are 5-10 higher than in the Line Islands (Loveley et al., 2017). Enhanced reversible scavenging due to high particle fluxes could also explain the high discrepancies between core-top $\varepsilon_{Nd\text{-}FD}$ and ε_{Nd} ratios in bottom waters in the EEP (Fig. 4.2b). This discrepancy between the mechanisms controlling the radiogenic enrichment of fish debris in the EEP versus the CEP fits within the framework established by Haley et al. (2017) and suggests that there are additional water column processes (unrelated to enhanced biogenic fluxes) that may act as secondary controls on the ε_{Nd} ratios of seawater.

We can examine the lithogenic particle flux by looking at the ^{230}Th normalized-^{232}Th dust flux (Jacobel et al., 2017a) (Fig. 4.5d). Dust flux at site 17PC peaks during glacial times and is the lowest during the warm MIS 1 and MIS 5 intervals (Jacobel et al., 2017a, Jacobel et al., 2016). There is moderate agreement between increases in dust flux and peaks in ε_{Nd} ratios. The dust flux peaks at MIS 2 and MIS 4 are contemporaneous with the two glacial radiogenic enrichment events (Fig. 4.5). However, during MIS 1 and MIS 5, ε_{Nd} ratios peak, while dust fluxes are depressed. Critically, the sustained elevated dust fluxes during MIS 3 do not appear to have any impact on the $\varepsilon_{Nd\text{-}FD}$ ratios.

4.5.4.2 The radiogenic enrichment of the lithogenic fraction through time

The relationship between the Nd isotopes in authigenic and detrital phases is a critical component of evaluating the mechanism behind the non-conservative behavior of ε_{Nd} ratios in various records (Du et al., 2016). Changes in sediment distribution and composition can alter the ε_{Nd} signature of the authigenic phases without a change in water mass (Scher and Martin, 2004, Fagel and Hillaire-Marcel, 2006, Franzese et al., 2006). Small changes in particle dissolution can alter the ε_{Nd} signal of seawater (Jeandel and Oelkers, 2015, Oelkers et al., 2011, Pearce et al., 2013). In the CEP, we can compare our archival $\varepsilon_{Nd\text{-}FD}$ record to previous determinations of the operationally-defined detrital fraction (Reimi and Marcantonio, 2016, Reimi et al., in prep) to estimate how potential particle composition may alter $\varepsilon_{Nd\text{-}FD}$ ratios.

At site 17PC the fish debris ε_{Nd} ratios are consistently more radiogenic than the detrital ε_{Nd} ratios ($\varepsilon_{Nd\text{-}DET}$) (Fig. 4.6). There is no coherent temporal trend in the degree of $\varepsilon_{Nd\text{-}FD}$ radiogenic enrichment relative to $\varepsilon_{Nd\text{-}DET}$. Across the last 150 kyrs, there is little change in the provenance of the dust delivered to this site, as measured by Pb and Nd isotopes (Reimi and Marcantonio, 2016, Reimi et al., in prep). Therefore, it is unlikely that the difference in ε_{Nd}

enrichment in the authigenic phase is due to changes in the reactivity of the terrigenous component (Wilson et al., 2013, Abbott et al., 2016). The one significant change in provenance occurs at the MIS 6/ MIS 5 boundary, where the dust at 17PC has a significantly more Asian provenance (Reimi et al., in prep), which could explain the decrease in the ε_{Nd} signal at this time.

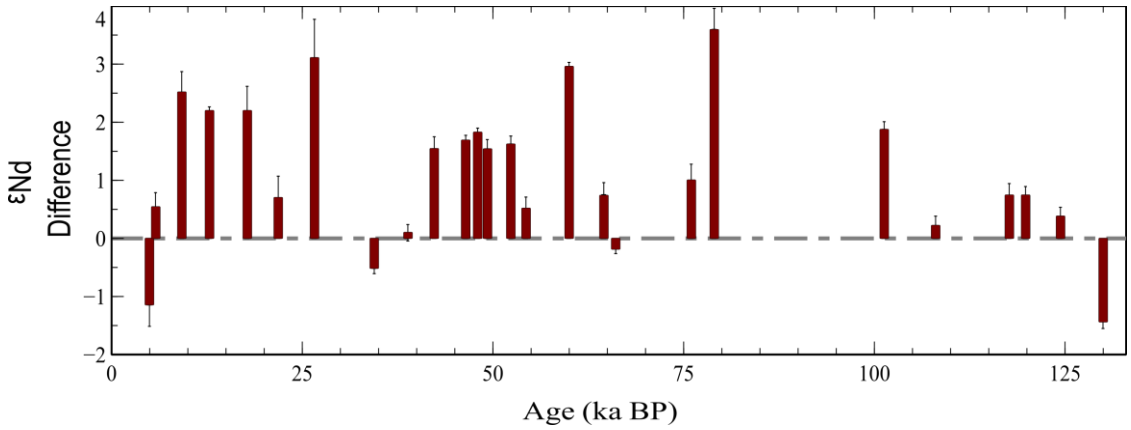

Figure 4.6 Difference between detrital ε_{Nd} and fish debris ε_{Nd} ($\varepsilon_{Nd\text{-}DET}$-$\varepsilon_{Nd\text{-}FD}$) at site ML1208-17PC. The detrital residue is the operationally defined detrital value as isolated in Reimi et al. (2016) and Reimi et al. (in prep), as well as this study (see supplemental). The baseline was generating by using a five-point average of all detrital ε_{Nd} values in the record over time

One important caveat for this argument is that the $\varepsilon_{Nd\text{-}DET}$ values are measurements of the operationally-defined aluminosilicate fraction, a fraction which is subjected to sequential leaching (Reimi and Marcantonio, 2016, Reimi et al., in prep, Xie and Marcantonio, 2012). Studies of sequential leaching often focus on the contamination of the authigenic phases by detrital material (Martin et al., 2010, Bayon et al., 2002, Gutjahr et al., 2008, Blaser et al., 2016), or the correct recovery of the authigenic phase from bulk sediment (Piotrowski et al., 2012, Roberts et al., 2012). But it is also true that sequential leaching can attack vulnerable aluminosilicate fractions, like fine grained ash, which is more reactive than weathered crustal

materials (Elderfield and Gieskes, 1982, Jones et al., 2012, Jeandel and Oelkers, 2015, Wilson et al., 2013, Bayon et al., 2015).

A detrital volcanic component can affect the ε_{Nd} ratios of leachates (Vance et al., 2004, Roberts et al., 2010, Elmore et al., 2011), which implies the loss of volcanic material during the chemical abrasion of bulk sediments. The overprinting of the $\varepsilon_{Nd\text{-}FD}$ ratios is not a concern. Rather, the concern is whether we are underestimating the impact of chemical alteration of the $\varepsilon_{Nd\text{-}DET}$ ratio during early diagenesis because we have leached the most labile volcanic ash, which might exhibit a different ε_{Nd} signature (Wilson et al., 2013). In the North Pacific, the volcanic component is radiogenically enriched, with an average ε_{Nd} signature of +4 (Jones et al., 1994). If sequential leaching preferentially leaches away a distinct volcanic component, then the Nd isotope of the measured residual component is not a true representative of the bulk detrital (i.e sedimentary eolian fraction plus volcanogenic fraction) composition.

Dispersed ash is a significant component of the residual operationally-defined aluminosilicate fraction (Ziegler et al., 2007, Scudder et al., 2014) in sediment samples from the Pacific Ocean. However, it is not possible to completely chemically separate volcanic ash from pelagic clay (Dunlea et al., 2015, Scudder et al., 2016). Moreover, laboratory sequential leaching can have varying effective recovery rates depending on lithology (Kryc et al., 2003). This suggest that our sequential leaching residuals might misrepresent the full detrital inputs – preserving the sedimentary eolian fraction, but possibly leaching the volcanogenic fraction. This missing ash could have an outsized effect on the ε_{Nd} radiogenic enrichment. Ash dissolution in pore waters has been shown to affect the REE distribution during early diagenesis (Schacht et al., 2010). This radiogenic enrichment can happen even when more inert detrital (i.e. clays) material is the dominant source of the Nd budget (Wilson et al., 2012). In the NE Atlantic a comparison

of volcanic IRD and ε_{Nd} on glacial-interglacial cycles, also found a substantial effect of isotope relabeling of the NADW during MIS 2 (Roberts and Piotrowski, 2015).

Simply stated, it seems like the measured $\varepsilon_{Nd\text{-}DET}$ ratios are less radiogenic than the $\varepsilon_{Nd\text{-}FD}$ values (Fig. 4.6), however as these measures are performed on the sequential leaching residue (i.e. detrital fraction minus volcanogenic fraction), we are possibly underestimating the impact of changes in detrital composition to pore water ε_{Nd} (Abbott et al., 2015a). Therefore, we do not think it is appropriate to examine the ε_{Nd} ratios of sequential leaching residues to assess the diagenic contamination of authigenic phases, as previously suggested by Wilson et al. (2013). This does not challenge the use of Nd isotopes as dust provenance tracer, since the eolian inputs are preserved in leaching residuals. However, we suggest that the ε_{Nd} of leached potential dust source samples should be examined for more accurate dust source to residual ε_{Nd} comparisons (Nakai et al., 1993).

We support the previous eolian dust provenance estimates calculated for 17PC (Reimi and Marcantonio, 2016, Reimi et al., in prep). As further evidence from the Pb isotopic composition of 17PC shows variations that are consistent with mixing of South American sources (Reimi and Marcantonio, 2016, Reimi et al., in prep). Moreover, work by Pichat et al. (2014) suggest that there is very little separation of Pb isotopes among different phases of sediment, as bulk leachates reflect detrital Pb values, suggesting that the composition of the detrital material in CEP has changed very little over the past 125 kyr.

Instead of changes in the composition of detrital sediment through time, we argue that the changes in the modification of $\varepsilon_{Nd\text{-}FD}$ ratios over time are due to the increased reactivity of the detrital component supply during exposure to oxic bottom waters, as determined using aU records (Fig. 4.5, Fig. 4.7) (Section 4.5.5).

4.5.5 Oxic pore water and $\varepsilon_{Nd\text{-}FD}$

Archives of Nd isotope composition such as fish debris inherit the ε_{Nd} signal of pore waters during early diagenesis, but are subjected to alteration from the reactive elements of detritus (Du et al., 2016). Here, we examine the impact of oxic pore water conditions on the reactivity of detrital sediment. We suggest that such reactivity, which plays the largest role in affecting $\varepsilon_{Nd\text{-}FD}$ at site 17PC, is a consequence of the reduced ventilation of the Southern Ocean during glacial times (Anderson et al., 2009).

In order to explore the onset of reducing conditions at site ML1208-17PC in light of aU burndown, we compared the 17PC aU record (Jacobel et al., 2017b), with aU at two equatorial sites further east, PC72 (Winckler et al., 2016, Anderson et al., 2006), and MV1014-02-17JC (hereafter referred to as 17JC; 0.18° S, 85.57° W, at 2846 m, (Loveley et al., 2017), Fig. 4.7). The 5-10 times higher sedimentation rate of site 17JC improves the preservation of aU and its timing in the equatorial Pacific. This record agrees with the near-equatorial aU records at sites west of the Line Islands (Bradtmiller et al., 2010), which show a similar high-amplitude increase in aU during the last 30 kyrs. At 17JC, the lack of coincidence between Ba_{xs} flux and aU peaks, suggests that aU reflect bottom-water conditions, and that EEP bottom waters were likely continuously suboxic during the glacial period –MIS 2, 3 and 4 (Loveley et al., 2017). Low-oxygen bottom waters during the last glacial period that occurred across a wide swath of the equatorial Pacific from the east (Loveley et al., 2017; Bradtmiller et al., 2010) to the central Pacific (Jacobel et al., 2017) correlate with times of similar low-bottom-water oxygen levels in the Southern Ocean (Jaccard et al., 2016). These times of suboxic bottom waters are thought to reflect increased storage of respired carbon and reduced global ocean ventilation rates (Jacobel et al., 2017b, Loveley et al., 2017).

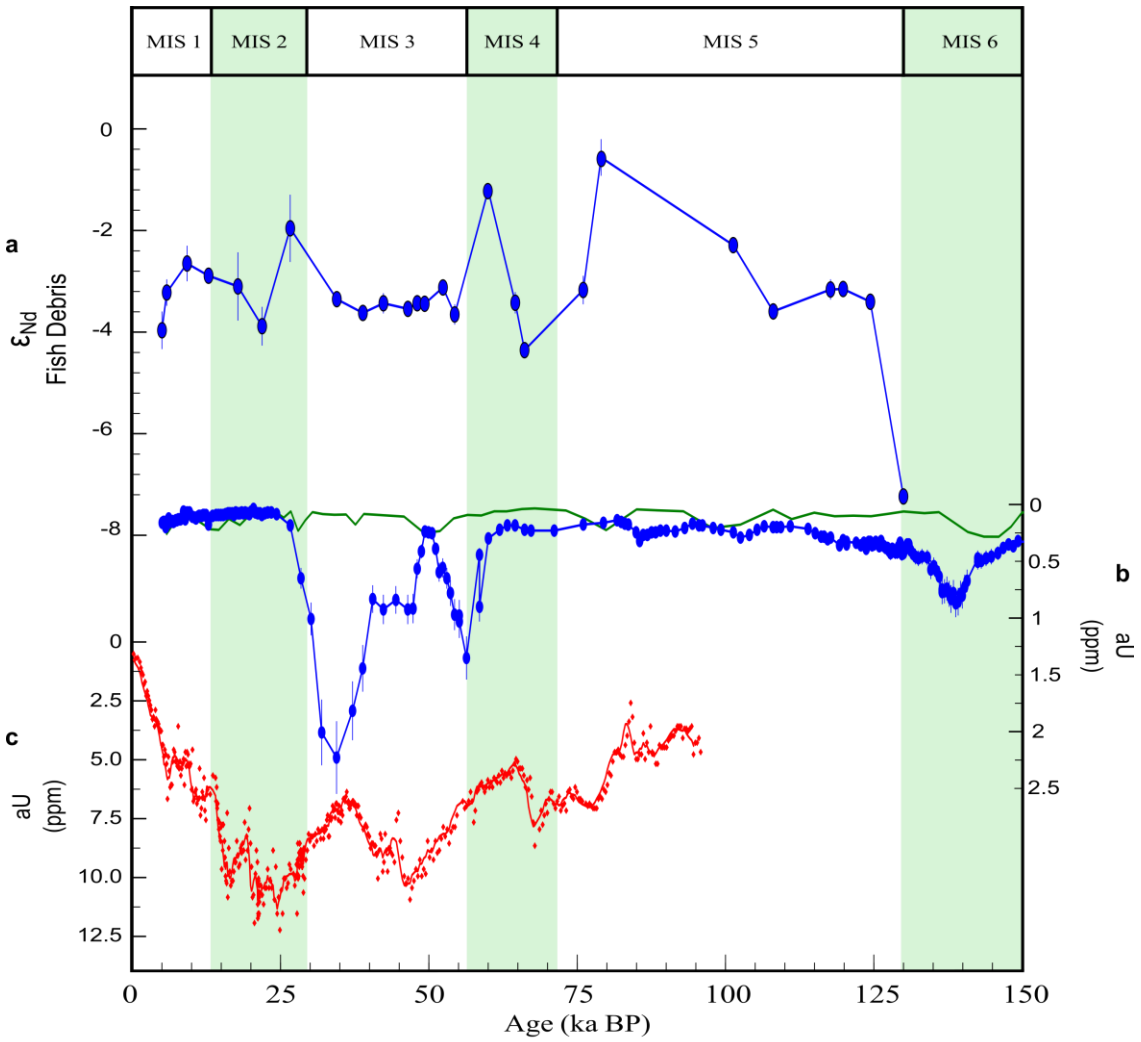

Figure 4.7 Pore water oxygen and ε_{Nd} trend in ML1208-17PC. a Neodymium isotopic record (blue circles). **b.** authigenic U for core ML1208-17PC (blue line) and authigenic Uranium in TT013-PC72 (green line) (Winckler et al., 2016) **c.** Authigenic Uranium for core MV1014-02-17JC (Loveley et al., 2017).

We can compare the timing of our CEP anomalous $\varepsilon_{Nd\text{-}FD}$ fish debris signatures to the timing of reduced ventilation (low bottom water oxygen values), as determined by Loveley et al. (2017) to potentially cover a wide swath of the Southern and Pacific Oceans (Fig. 4.7c). Here, we can see that the peaks in $\varepsilon_{Nd\text{-}FD}$ ratios happen close to the three major reductions in bottom-water oxygen.

If reduced ventilation rates in the Southern and Pacific Oceans, result in older less oxygenated NPDW, then the radiogenic ε_{Nd} pulses seen in our data may be a consequence of more sluggish and more stratified deep-waters. This fits the framework developed by Abbott et al. (2016), to explain the difference in the conservative behavior of the Atlantic and the Pacific. In the Atlantic faster moving waters (Kawabe and Fujio, 2010) behave more conservatively, while in the Pacific sluggish waters –therefore increasing exposure times to the benthic flux– lead to the enrichment of deep-waters. Assuming that the benthic flux remains relatively constant through the late Pleistocene, then pronounced $\varepsilon_{Nd\text{-}FD}$ enrichment of the Pacific could be aided by increased exposure to benthic flux as a response to decrease ventilation, combined with the effects of increased $\varepsilon_{Nd\text{-}DET}$ inputs during more reducing conditions (Du et al., 2016).

The non-conservative effects on the $\varepsilon_{Nd\text{-}FD}$ at site 17PC are dominated by the effects of low pore-water oxygen as seen in the aU record (Fig. 4.7), with alterations due to changes in particle flux and composition (Table 4.4). The $\varepsilon_{Nd\text{-}FD}$ enrichments during glacial time are due to increased reactions of reactive detrital material and lower pore water oxygen conditions.

4.6 Conclusions

In the CEP at site 17PC, $\varepsilon_{Nd\text{-}FD}$ ratios throughout most of the last 125 kyr are identical, within error, to those determined for modern-day NPDW. However, there are several periods of enriched $\varepsilon_{Nd\text{-}FD}$ values which cannot be explained by conservative water-mass mixing or water mass endmember changes through the last 125 kyrs. These enrichment events represent changes in the geochemical behavior Nd, suggesting a non-conservative behavior during certain intervals of the record. The punctuated non-conservative behavior is further supported by core-top ε_{Nd} signatures from a transect in the EEP, showing varying degrees of ε_{Nd} enrichment at different water depths.

We postulate that the ε_{Nd} record in 17PC signals changes in the exposure time to benthic flux and increased ash leaching during low oxygenation events, determined by comparing the timing of these events to previously published authigenic U records from the Pacific (Fig. 4.5e). If suboxic conditions in the equatorial Pacific are produced by reduced oceanic ventilation rates, then $\varepsilon_{Nd\text{-}FD}$ records may be used as support for changes in such rates. Changes in particle flux and chemical composition only present minor influences on the non-conservative behavior of Nd.

4.7 Tables

Table 4.1 Location and water depth of all cores in section 4.

Core	Latitude (° N)	Longitude (° W)	Water Depth (m)
ML1208-13BB	-0.22	155.96	3050
ML1208-17PC	0.48	156.45	2926
ML1208-20BB	1.27	157.26	2850
TT013-PC72	0.1	139.4	4300
MV1014-02-17JC	-0.18	85.57	2846
Core tops	(Appendix C)		

Table 4.2 Nd isotopic composition of fish debris in ML1208-17PC.

Depth (cm)		Age	Fish debris	
Top	Bottom	(ka)	ε_{Nd}	±SE
0	1	5.0	-4.0	0.4
4	5	5.8	-3.2	0.3
20	21	9.2	-2.7	0.4
32	33	12.8	-2.91	0.08
44	45	17.8	-3.1	0.7
56	57	21.8	-3.9	0.4
64	65	26.6	-2.0	0.7
80	81	34.4	-3.37	0.09

Table 4.2 Continued

Depth (cm)		Age	Fish debris	
Top	Bottom	(ka)	ε_{Nd}	±SE
88	89	38.8	-3.6	0.1
96	97	42.3	-3.4	0.2
104	105	46.4	-3.56	0.09
112	113	48.0	-3.45	0.07
120	121	49.3	-3.5	0.2
140	141	52.3	-3.1	0.1
120	121	49.3	-3.5	0.2
140	141	52.3	-3.1	0.1
152	153	54.3	-3.7	0.2
168	169	60.0	-1.23	0.07
180	181	64.5	-3.4	0.2
184	185	66.1	-4.37	0.08
196	197	76.0	-3.2	0.3
200	201	79.0	-0.6	0.4
260	261	101.3	-2.3	0.1
280	281	108.0	-3.6	0.2
300	301	117.7	-3.2	0.2
304	305	119.8	-3.2	0.1
312	313	124.4	-3.4	0.2
332	333	130.0	-7.2	0.1

Table 4.3 Nd isotopic composition of fish debris in core-tops at site MV1014-03

Core	Latitude (° N)	Longitude (° W)	Water Depth (m)	Age (Ka)	$\varepsilon_{Nd\text{-}FD}$	±SE
MV1014-1MC	5.82	85.73	1760	4899	0.4	0.1
MV1014-6MC	6.17	86.15	1257	1328	0.3	0.2
MV1014-9MC	0.69	85.31	2452	2585	-1.4	0.1
MV1014-16MC	0.17	85.87	2846	1000	-1.3	0.1
MV1014-20MC	-8.5	87.03	4407	1000[a]	-3.6	0.1
20MC_rerun	-8.5	87.03	4407	1000[a]	-3.5	0.1

* errors are standard error. Ages from Marcantonio et al. (2014). **a.** Age for 20MC is an estimate based ^{14}C ages on core HY08B at 5.95 °S, 95.44° E (Horikawa et al., 2006).

Table 4.4 List of non-conservative influence on the ε_{Nd} radiogenic highs at 17PC.

	Holocene	27 ka (MIS 2)	59 ka (MIS 4)	79 ka (MIS 5)
Biogenic flux	↑	↔	↓	↔
Dust flux	↔	↑	↑↑	↔
Detrital Composition	↑	↓	↓↓	↓
aU (CEP)	↔	↔	↑	↔
aU (EEP)	↑↑	↑↑	↔	↑

↑↑ (peak value) ↑ (high value) ↔ (baseline value) ↓ (low value) ↓↓ (lowest value).

4.8 References

ABBOTT, A. N., HALEY, B. A. & GEOLOGY, M.-J. 2015a. Bottoms up: Sedimentary control of the deep North Pacific Ocean's εNd signature. *Geology*.

ABBOTT, A. N., HALEY, B. A. & MCMANUS, J. 2016. The impact of sedimentary coatings on the diagenetic Nd flux. *Earth and Planetary Science Letters,* 449**,** 217-227.

ABBOTT, A. N., HALEY, B. A., MCMANUS, J. & REIMERS, C. E. 2015b. The sedimentary flux of dissolved rare earth elements to the ocean. *Geochimica et Cosmochimica Acta,* 154**,** 186-200.

AKAGI, T., YASUDA, S., ASAHARA, Y., EMOTO, M. & TAKAHASHI, K. 2014. Diatoms spread a high εNd-signature in the North Pacific Ocean. *GEOCHEMICAL JOURNAL,* 48**,** 121-131.

AMAKAWA, H., ALIBO, D. S. & NOZAKI, Y. 2004. Nd concentration and isotopic composition distributions in surface waters of Northwest Pacific Ocean and its adjacent seas. *Geochemical Journal,* 38**,** 493-504.

AMAKAWA, H., SASAKI, K. & EBIHARA, M. 2009. Nd isotopic composition in the central North Pacific. *Geochimica et Cosmochimica Acta,* 73**,** 4705-4719.

ANDERSON, R., FLEISHER, M. & LAO, Y. 2006. Glacial–interglacial variability in the delivery of dust to the central equatorial Pacific Ocean. *Earth and Planetary Science Letters,* 242**,** 406-414.

ANDERSON, R. F., ALI, S., BRADTMILLER, L. I., NIELSEN, S. H. H., FLEISHER, M. Q., ANDERSON, B. E. & BURCKLE, L. H. 2009. Wind-Driven Upwelling in the Southern Ocean and the Deglacial Rise in Atmospheric CO_2. *Science,* 323**,** 1443-1448.

ARSOUZE, T., DUTAY, J. C., LACAN, F. & JEANDEL, C. 2009. Reconstructing the Nd oceanic cycle using a coupled dynamical – biogeochemical model. *Biogeosciences,* 6.

BASAK, C., MARTIN, E., HORIKAWA, K. & MARCHITTO, T. 2010. Southern Ocean source of 14 C-depleted carbon in the North Pacific Ocean during the last deglaciation. *Nature Geoscience,* 3**,** 770.

BAYON, G., GERMAN, C. R., BOELLA, R. M., MILTON, J. A., TAYLOR, R. N. & NESBITT, R. W. 2002. An improved method for extracting marine sediment fractions and its application to Sr and Nd isotopic analysis. *Chemical Geology,* 187**,** 179-199.

BAYON, G., TOUCANNE, S., SKONIECZNY, C., ANDRÉ, L., BERMELL, S., CHERON, S., DENNIELOU, B., ETOUBLEAU, J., FRESLON, N., GAUCHERY, T., GERMAIN, Y., JORRY, S. J., MÉNOT, G., MONIN, L., PONZEVERA, E., ROUGET, M. L., TACHIKAWA, K. & BARRAT, J. A. 2015. Rare earth elements and neodymium isotopes in world river sediments revisited. *Geochimica et Cosmochimica Acta,* 170**,** 17-38.

BLASER, P., LIPPOLD, J., GUTJAHR, M., FRANK, N., LINK, J. M. & FRANK, M. 2016. Extracting foraminiferal seawater Nd isotope signatures from bulk deep sea sediment by chemical leaching. *Chemical Geology,* 439**,** 189-204.

BRADTMILLER, L. I., ANDERSON, R. F., SACHS, J. P. & FLEISHER, M. Q. 2010. A deeper respired carbon pool in the glacial equatorial Pacific Ocean. *Earth and Planetary Science Letters,* 299**,** 417-425.

BROECKER, W. S. & PENG, T.-H. 1982. *Tracers in the Sea,* Palisades, NY, Eldigio Press.

CARTER, P., VANCE, D., HILLENBRAND, C. D., SMITH, J. A. & SHOOSMITH, D. R. 2012. The neodymium isotopic composition of waters masses in the eastern Pacific sector of the Southern Ocean. *Geochimica et Cosmochimica Acta,* 79**,** 41-59.

COSTA, K. M., JACOBEL, A. W., MCMANUS, J. F., ANDERSON, R. F., WINCKLER, G. & THIAGARAJAN, N. 2017. Productivity patterns in the equatorial Pacific over the last 30,000 years. *Global Biogeochemical Cycles*.

COSTA, K. M., MCMANUS, J. F., ANDERSON, R., REN, H., SIGMAN, D., WINCKLER, G., FLEISHER, M., MARCANTONIO, F. & RAVELO, A. 2016. No iron fertilization in the equatorial Pacific Ocean during the last ice age. *Nature,* 529**,** 519-522.

DU, J., HALEY, B. A. & MIX, A. C. 2016. Neodymium isotopes in authigenic phases, bottom waters and detrital sediments in the Gulf of Alaska and their implications for paleo-circulation reconstruction. *Geochimica et Cosmochimica Acta,* 193**,** 14-35.

DUNLEA, A. G., MURRAY, R. W., SAUVAGE, J., SPIVACK, A. J., HARRIS, R. N. & D'HONDT, S. 2015. Dust, volcanic ash, and the evolution of the South Pacific Gyre through the Cenozoic. *Paleoceanography,* 30**,** 1078-1099.

DYMOND, J., SUESS, E. & LYLE, M. 1992. Barium in deep-sea sediment: A geochemical proxy for paleoproductivity. *Paleoceanography,* 7**,** 163-181.

EHLERT, C., GRASSE, P. & FRANK, M. 2013. Changes in silicate utilisation and upwelling intensity off Peru since the Last Glacial Maximum – insights from silicon and neodymium isotopes. *Quaternary Science Reviews,* 72**,** 18-35.

ELDERFIELD, H., FERRETTI, P., GREAVES, M., CROWHURST, S., MCCAVE, I., HODELL, D. & PIOTROWSKI, A. 2012. Evolution of ocean temperature and ice volume through the mid-Pleistocene climate transition. *Science,* 337**,** 704-709.

ELDERFIELD, H. & GIESKES, J. M. 1982. Sr isotopes in interstitial waters of marine sediments from Deep Sea Drilling Project cores. *Nature,* 300**,** 493.

ELDERFIELD, H. & PAGETT, R. 1986. Rare earth elements in ichthyoliths: variations with redox conditions and depositional environment. *Science of the Total Environment,* 49**,** 175-197.

ELMORE, A. C., PIOTROWSKI, A. M., WRIGHT, J. D. & SCRIVNER, A. E. 2011. Testing the extraction of past seawater Nd isotopic composition from North Atlantic deep sea sediments and foraminifera. *Geochemistry, Geophysics, Geosystems,* 12**,** n/a-n/a.

FAGEL, N. & HILLAIRE-MARCEL, C. 2006. Glacial/interglacial instabilities of the Western Boundary Under Current during the last 365 kyr from Sm/Nd ratios of the sedimentary clay-size fractions at ODP site 646 (Labrador Sea). *Marine Geology,* 232**,** 87-99.

FOSTER, G. L., VANCE, D. & PRYTULAK, J. 2007. No change in the neodymium isotope composition of deep water exported from the North Atlantic on glacial-interglacial time scales. *Geology,* 35**,** 37-40.

FRANK, M. 2002. Radiogenic isotopes: Tracers of past ocean circulation and erosional input. *Reviews of Geophysics,* 40.

FRANZESE, A. M., HEMMING, S. R., GOLDSTEIN, S. L. & ANDERSON, R. F. 2006. Reduced Agulhas Leakage during the Last Glacial Maximum inferred from an integrated provenance and flux study. *Earth and Planetary Science Letters,* 250**,** 72-88.

FRÖLLJE, H., PAHNKE, K., SCHNETGER, B., BRUMSACK, H.-J., DULAI, H. & FITZSIMMONS, J. N. 2016. Hawaiian imprint on dissolved Nd and Ra isotopes and rare earth elements in the central North Pacific: Local survey and seasonal variability. *Geochimica et Cosmochimica Acta,* 189**,** 110-131.

GARCIA, H. E., LOCARNINI, R. A., BOYER, T. P., ANTONOV, J. I., BARANOVA, O. K., ZWENG, M. M., REAGAN, J. R. & JOHNSON, D. R. 2014. World Ocean Atlas 2013, Volume 3: Dissolved Oxygen, Apparent Oxygen Utilization, and Oxygen Saturation. *In:* LEVITUS, S. & MISHONOV, A. (eds.) *NOAA Atlas NESDIS.*

GOLDSTEIN, S. L. & HEMMING, S. R. 2003. Long-lived isotopic tracers in oceanography, paleoceanography, and ice-sheet dynamics. *Treatise on geochemistry,* 6**,** 453-489.

GRASSE, P., STICHEL, T., STUMPF, R., STRAMMA, L. & FRANK, M. 2012. The distribution of neodymium isotopes and concentrations in the Eastern Equatorial Pacific: Water mass advection versus particle exchange. *Earth and Planetary Science Letters,* 353**,** 198-207.

GRIFFITH, E. M. & PAYTAN, A. 2012. Barite in the ocean – occurrence, geochemistry and palaeoceanographic applications. *Sedimentology,* 59**,** 1817-1835.

GUTJAHR, M., FRANK, M., STIRLING, C. H., KEIGWIN, L. D. & HALLIDAY, A. N. 2008. Tracing the Nd isotope evolution of North Atlantic Deep and Intermediate Waters in the western North Atlantic since the Last Glacial Maximum from Blake Ridge sediments. *Earth and Planetary Science Letters,* 266**,** 61-77.

HAGUE, A. M., THOMAS, D. J., HUBER, M., KORTY, R., WOODARD, S. C. & JONES, L. B. 2012. Convection of North Pacific deep water during the early Cenozoic. *Geology,* 40**,** 527-530.

HALEY, B. A., DU, J., ABBOTT, A. N. & MCMANUS, J. 2017. The Impact of Benthic Processes on Rare Earth Element and Neodymium Isotope Distributions in the Oceans. *Frontiers in Marine Science,* 4**,** 426.

HORIKAWA, K., MARTIN, E. E., ASAHARA, Y. & SAGAWA, T. 2011. Limits on conservative behavior of Nd isotopes in seawater assessed from analysis of fish teeth from Pacific core tops. *Earth and Planetary Science Letters,* 310**,** 119-130.

HORIKAWA, K., MINAGAWA, M., MURAYAMA, M., KATO, Y. & ASAHI, H. 2006. Spatial and temporal sea-surface temperatures in the eastern equatorial Pacific over the past 150 kyr. *Geophysical Research Letters,* 33**,** n/a-n/a.

HOWE, J. N., PIOTROWSKI, A. M. & RENNIE, V. C. 2016. Abyssal origin for the early Holocene pulse of unradiogenic neodymium isotopes in Atlantic seawater. *Geology,* 44**,** 831-834.

HU, R., NOBLE, T. L., PIOTROWSKI, A. M., MCCAVE, N. I., BOSTOCK, H. C. & NEIL, H. L. 2016a. Neodymium isotopic evidence for linked changes in Southeast Atlantic and Southwest Pacific circulation over the last 200 kyr. *Earth and Planetary Science Letters,* 455**,** 106-114.

HU, R., PIOTROWSKI, A. M., BOSTOCK, H. C., CROWHURST, S. & RENNIE, V. 2016b. Variability of neodymium isotopes associated with planktonic foraminifera in the Pacific Ocean during the Holocene and Last Glacial Maximum. *Earth and Planetary Science Letters,* 447**,** 130-138.

HUCK, C. E., VAN DE FLIERDT, T., JIMÉNEZ-ESPEJO, F. J., BOHATY, S. M., RÖHL, U. & HAMMOND, S. J. 2016. Robustness of fossil fish teeth for seawater neodymium isotope reconstructions under variable redox conditions in an ancient shallow marine setting. *Geochemistry, Geophysics, Geosystems,* 17**,** 679-698.

JACOBEL, A. W., MCMANUS, J., ANDERSON, R. & WINCKLER, G. 2016. Large deglacial shifts of the Pacific Intertropical Convergence Zone. *Nature Communications,* 7.

JACOBEL, A. W., MCMANUS, J. F., ANDERSON, R. F. & WINCKLER, G. 2017a. Climate-related response of dust flux to the central equatorial Pacific over the past 150 kyr. *Earth and Planetary Science Letters,* 457**,** 160-172.

JACOBEL, A. W., WINCKLER, G., MCMANUS, J. & ANDERSON, R. 2017b. Repeated storage of respired carbon in the equatorial Pacific Ocean over the last three glacial cycles. *Nature communications,* 8**,** 1727.

JACOBSEN, S. B. & WASSERBURG, G. 1980. Sm-Nd isotopic evolution of chondrites. *Earth and Planetary Science Letters,* 50**,** 139-155.

JEANDEL, C. 2016. Overview of the mechanisms that could explain the 'Boundary Exchange' at the land–ocean contact. *Phil. Trans. R. Soc. A,* 374**,** 20150287.

JEANDEL, C. & OELKERS, E. H. 2015. The influence of terrigenous particulate material dissolution on ocean chemistry and global element cycles. *Chemical Geology,* 395**,** 50-66.

JOHANNESSON, K. H. & BURDIGE, D. J. 2007. Balancing the global oceanic neodymium budget: evaluating the role of groundwater. *Earth and Planetary Science Letters,* 253**,** 129-142.

JONES, C. E., HALLIDAY, A. N., REA, D. K. & OWEN, R. M. 1994. Neodymium isotopic variations in North Pacific modern silicate sediment and the insignificance of detrital REE contributions to seawater. *Neodymium isotopic variations in North Pacific modern silicate sediment and the insignificance of detrital REE contributions to seawater*.

JONES, K. M., KHATIWALA, S. P., GOLDSTEIN, S. L., HEMMING, S. R. & VAN DE FLIERDT, T. 2008. Modeling the distribution of Nd isotopes in the oceans using an ocean general circulation model. *Earth and Planetary Science Letters,* 272**,** 610-619.

JONES, M. T., PEARCE, C. R., JEANDEL, C., GISLASON, S. R., EIRIKSDOTTIR, E. S., MAVROMATIS, V. & OELKERS, E. H. 2012. Riverine particulate material dissolution as a significant flux of strontium to the oceans. *Earth and Planetary Science Letters,* 355-356**,** 51-59.

KAWABE, M. & FUJIO, S. 2010. Pacific ocean circulation based on observation. *Journal of Oceanography,* 66**,** 389-403.

KRYC, K. A., MURRAY, R. W. & MURRAY, D. W. 2003. Elemental fractionation of Si, Al, Ti, Fe, Ca, Mn, P, and Ba in five marine sedimentary reference materials: results from sequential extractions. *Analytica Chimica Acta,* 487**,** 117-128.

LACAN, F. & JEANDEL, C. 2001. Tracing Papua New Guinea imprint on the central Equatorial Pacific Ocean using neodymium isotopic compositions and Rare Earth Element patterns. *Earth and Planetary Science Letters,* 186**,** 497-512.

LACAN, F. & JEANDEL, C. 2005. Neodymium isotopes as a new tool for quantifying exchange fluxes at the continent–ocean interface. *Earth and Planetary Science Letters,* 232**,** 245-257.

LACAN, F., TACHIKAWA, K. & JEANDEL, C. 2012. Neodymium isotopic composition of the oceans: A compilation of seawater data. *Chemical Geology,* 300**,** 177-184.

LISIECKI, L. E. & RAYMO, M. E. 2005. A Pliocene-Pleistocene stack of 57 globally distributed benthic δ18O records. *Paleoceanography,* 20.

LOVELEY, M., MARCANTONIO, F., WISLER, M., HERTZBERG, J., SCHMIDT, M. & LYLE, M. 2017. Millenial-scale iron fertilization of the eastern equatorial Pacific over the past 100,000 years. *Nature Geoscience*.

LYNCH-STIEGLITZ, J., POLISSAR, P. J., JACOBEL, A. W., HOVAN, S. A., POCKALNY, R. A., LYLE, M., MURRAY, R. W., RAVELO, C. A., BOVA, S. C., DUNLEA, A. G., FORD, H. L., HERTZBERG, J. E., WERTMAN, C. A., MALONEY, A. E., SHACKFORD, J. K., WEJNERT, K. & XIE, R. C. 2015. Glacial-interglacial changes in central tropical Pacific surface seawater property gradients. *Paleoceanography,* 30**,** 423-438.

MARCANTONIO, F., ANDERSON, R. F., HIGGINS, S., STUTE, M., SCHLOSSER, P. & KUBIK, P. 2001. Sediment focusing in the central equatorial Pacific Ocean. *Paleoceanography,* 16**,** 260-267.

MARCANTONIO, F., LYLE, M. & IBRAHIM, R. 2014. Particle sorting during sediment redistribution processes and the effect on 230Th-normalized mass accumulation rates. *Geophysical Research Letters,* 41**,** 5547-5554.

MARTIN, E. E., BLAIR, S. W., KAMENOV, G. D., SCHER, H. D., BOURBON, E., BASAK, C. & NEWKIRK, D. N. 2010. Extraction of Nd isotopes from bulk deep sea sediments for paleoceanographic studies on Cenozoic time scales. *Chemical Geology,* 269.

MARTIN, E. E. & HALEY, B. 2000. Fossil fish teeth as proxies for seawater Sr and Nd isotopes. *Geochimica et Cosmochimica Acta,* 64**,** 835-847.

MARTIN, E. E. & SCHER, H. D. 2004. Preservation of seawater Sr and Nd isotopes in fossil fish teeth: bad news and good news. *Earth and Planetary Science Letters,* 220.

MOLINA-KESCHER, M., FRANK, M. & HATHORNE, E. C. 2014. Nd and Sr isotope compositions of different phases of surface sediments in the South Pacific: Extraction of seawater signatures, boundary exchange, and detrital/dust provenance. *Geochemistry, Geophysics, Geosystems,* 15**,** 3502-3520.

MOLINA-KESCHER, M., FRANK, M., TAPIA, R., RONGE, T. A., NÜRNBERG, D. & TIEDEMANN, R. 2016. Reduced admixture of North Atlantic Deep Water to the deep central South Pacific during the last two glacial periods. *Paleoceanography,* 31**,** 651-668.

MURRAY, R., KNOWLTON, C., LEINEN, M., MIX, A. C. & POLSKY, C. 2000. Export production and carbonate dissolution in the central equatorial Pacific Ocean over the past 1 Myr. *Paleoceanography,* 15**,** 570-592.

MURRAY, R. W., LEINEN, M., MURRAY, D. W., MIX, A. C. & KNOWLTON, C. W. 1995. Terrigenous Fe input and biogenic sedimentation in the glacial and interglacial equatorial Pacific Ocean. *Global Biogeochemical Cycles,* 9.

NAKAI, S. I., HALLIDAY, A. N. & REA, D. K. 1993. Provenance of dust in the Pacific Ocean. *Earth and Planetary Science Letters,* 119.

NOBLE, T. L., PIOTROWSKI, A. M. & MCCAVE, N. I. 2013. Neodymium isotopic composition of intermediate and deep waters in the glacial southwest Pacific. *Earth and Planetary Science Letters,* 384**,** 27-36.

OELKERS, E. H., GISLASON, S. R., EIRIKSDOTTIR, E. S., JONES, M., PEARCE, C. R. & JEANDEL, C. 2011. The role of riverine particulate material on the global cycles of the elements. *Applied Geochemistry,* 26**,** S365-S369.

OSBORNE, A. H., HALEY, B. A., HATHORNE, E. C., FLÖGEL, S. & FRANK, M. 2014. Neodymium isotopes and concentrations in Caribbean seawater: Tracing water mass

mixing and continental input in a semi-enclosed ocean basin. *Earth and Planetary Science Letters,* 406**,** 174-186.

PAHNKE, K., FLIERDT, T. V. D., JONES, K. M., LAMBELET, M., HEMMING, S. R. & GOLDSTEIN, S. L. 2012. GEOTRACES intercalibration of neodymium isotopes and rare earth element concentrations in seawater and suspended particles. Part 2: Systematic tests and baseline profiles. *Limnology and Oceanography: Methods,* 10**,** 252-269.

PEARCE, C. R., JONES, M. T., OELKERS, E. H., PRADOUX, C. & JEANDEL, C. 2013. The effect of particulate dissolution on the neodymium (Nd) isotope and Rare Earth Element (REE) composition of seawater. *Earth and Planetary Science Letters,* 369-370.

PICHAT, S., ABOUCHAMI, W. & GALER, S. 2014. Lead isotopes in the Eastern Equatorial Pacific record Quaternary migration of the South Westerlies. *Earth and Planetary Science Letters,* 388.

PIEPGRAS, D. J. & JACOBSEN, S. B. 1988. The isotopic composition of neodymium in the North Pacific. *Geochimica et Cosmochimica Acta,* 52**,** 1373-1381.

PIEPGRAS, D. J. & JACOBSEN, S. B. 1992. The behavior of rare earth elements in seawater: Precise determination of variations in the North Pacific water column. *Geochimica et Cosmochimica Acta,* 56**,** 1851-1862.

PIEPGRAS, D. J. & WASSERBURG, G. J. 1982. Isotopic composition of neodymium in waters from the Drake Passage. *Science,* 217**,** 207-214.

PIOTROWSKI, A. M., GALY, A., NICHOLL, J. A. L., ROBERTS, N., WILSON, D. J., CLEGG, J. A. & YU, J. 2012. Reconstructing deglacial North and South Atlantic deep water sourcing using foraminiferal Nd isotopes. *Earth and Planetary Science Letters,* 357-358.

PIOTROWSKI, A. M., GOLDSTEIN, S. L., HEMMING, S. R. & FAIRBANKS, R. G. 2005. Temporal relationships of carbon cycling and ocean circulation at glacial boundaries. *Science (New York, N.Y.),* 307**,** 1933-1938.

PRAKASH BABU, C., BRUMSACK, H. J., SCHNETGER, B. & BÖTTCHER, M. E. 2002. Barium as a productivity proxy in continental margin sediments: a study from the eastern Arabian Sea. *Marine Geology,* 184**,** 189-206.

REIMI, M. A. & MARCANTONIO, F. 2016. Constraints on the magnitude of the deglacial migration of the ITCZ in the Central Equatorial Pacific Ocean. *Earth and Planetary Science Letters,* 453**,** 1-8.

REIMI, M. A., MARCANTONIO, F., LYNCH STIEGLITZ, J., JACOBEL, A. W., MCMANUS, J. F. & WINCKLER, G. in prep. The penultimate glacial terminaiton and large migrations of the Pacific Intertropical Convergence Zone.

REMPFER, J., STOCKER, T. F., JOOS, F., DUTAY, J.-C. & SIDDALL, M. 2011. Modelling Nd-isotopes with a coarse resolution ocean circulation model: Sensitivities to model parameters and source/sink distributions. *Geochimica et Cosmochimica Acta,* 75**,** 5927-5950.

REYNARD, B., LÉCUYER, C. & GRANDJEAN, P. 1999. Crystal-chemical controls on rare-earth element concentrations in fossil biogenic apatites and implications for paleoenvironmental reconstructions. *Chemical Geology,* 155**,** 233-241.

ROBERTS, N. L. & PIOTROWSKI, A. M. 2015. Radiogenic Nd isotope labeling of the northern NE Atlantic during MIS 2. *Earth and Planetary Science Letters,* 423**,** 125-133.

ROBERTS, N. L., PIOTROWSKI, A. M., ELDERFIELD, H., EGLINTON, T. I. & LOMAS, M. W. 2012. Rare earth element association with foraminifera. *Geochimica et Cosmochimica Acta,* 94**,** 57-71.

ROBERTS, N. L., PIOTROWSKI, A. M., MCMANUS, J. F. & KEIGWIN, L. D. 2010. Synchronous Deglacial Overturning and Water Mass Source Changes. *Science,* 327**,** 75-78.

ROUSSEAU, T. C. C., SONKE, J. E., CHMELEFF, J., VAN BEEK, P., SOUHAUT, M., BOAVENTURA, G., SEYLER, P. & JEANDEL, C. 2015. Rapid neodymium release to marine waters from lithogenic sediments in the Amazon estuary. *Nature Communications,* 6**,** 7592.

RYAN, W. B., CARBOTTE, S. M., COPLAN, J. O., O'HARA, S., MELKONIAN, A., ARKO, R., WEISSEL, R. A., FERRINI, V., GOODWILLIE, A. & NITSCHE, F. 2009. Global multi-resolution topography synthesis. *Geochemistry, Geophysics, Geosystems,* 10.

SCHACHT, U., WALLMANN, K. & KUTTEROLF, S. 2010. The influence of volcanic ash alteration on the REE composition of marine pore waters. *Journal of Geochemical Exploration,* 106**,** 176-187.

SCHENAU, S. J., PRINS, M. A., DE LANGE, G. J. & MONNIN, C. 2001. Barium accumulation in the Arabian Sea: controls on barite preservation in marine sediments. *Geochimica et Cosmochimica Acta,* 65**,** 1545-1556.

SCHER, H. D. & MARTIN, E. E. 2004. Circulation in the Southern Ocean during the Paleogene inferred from neodymium isotopes. *Earth and Planetary Science Letters,* 228**,** 391-405.

SCHLITZER, R. 2015. *Ocean Data View* [Online]. Available: https://odv.awi.de/ [Accessed 02/22/2018].

SCUDDER, R. P., MURRAY, R. W., SCHINDLBECK, J. C., KUTTEROLF, S., HAUFF, F. & MCKINLEY, C. C. 2014. Regional-scale input of dispersed and discrete volcanic ash to the Izu-Bonin and Mariana subduction zones. *Geochemistry, Geophysics, Geosystems,* 15**,** 4369-4379.

SCUDDER, R. P., MURRAY, R. W., SCHINDLBECK, J. C., KUTTEROLF, S., HAUFF, F., UNDERWOOD, M. B., GWIZD, S., LAUZON, R. & MCKINLEY, C. C. 2016. Geochemical approaches to the quantification of dispersed volcanic ash in marine sediment. *Progress in Earth and Planetary Science,* 3**,** 1.

SHAW, H. & WASSERBURG, G. 1985. Sm-Nd in marine carbonates and phosphates: Implications for Nd isotopes in seawater and crustal ages. *Geochimica et Cosmochimica Acta,* 49**,** 503-518.

SHIMIZU, H., TACHIKAWA, K., MASUDA, A. & NOZAKI, Y. 1994. Cerium and neodymium isotope ratios and REE patterns in seawater from the North Pacific Ocean. *Geochimica et Cosmochimica Acta,* 58.

SIDDALL, M., KHATIWALA, S., VAN DE FLIERDT, T., JONES, K., GOLDSTEIN, S. L., HEMMING, S. & ANDERSON, R. F. 2008. Towards explaining the Nd paradox using reversible scavenging in an ocean general circulation model. *Earth and Planetary Science Letters,* 274**,** 448-461.

SINGH, S. P., SINGH, S. K., GOSWAMI, V., BHUSHAN, R. & RAI, V. K. 2012. Spatial distribution of dissolved neodymium and εNd in the Bay of Bengal: Role of particulate matter and mixing of water masses. *Geochimica et Cosmochimica Acta,* 94**,** 38-56.

STAUDIGEL, H., DOYLE, P. & ZINDLER, A. 1985. Sr and Nd isotope systematics in fish teeth. *Earth and Planetary Science Letters,* 76**,** 45-56.

STEWART, J. A., GUTJAHR, M., JAMES, R. H., ANAND, P. & WILSON, P. A. 2016. Influence of the Amazon River on the Nd isotope composition of deep water in the western equatorial Atlantic during the Oligocene–Miocene transition. *Earth and Planetary Science Letters,* 454**,** 132-141.

STICHEL, T., FRANK, M., RICKLI, J. & HALEY, B. A. 2012a. The hafnium and neodymium isotope composition of seawater in the Atlantic sector of the Southern Ocean. *Earth and Planetary Science Letters,* 317**,** 282-294.

STICHEL, T., FRANK, M., RICKLI, J., HATHORNE, E. C., HALEY, B. A., JEANDEL, C. & PRADOUX, C. 2012b. Sources and input mechanisms of hafnium and neodymium in surface waters of the Atlantic sector of the Southern Ocean. *Geochimica et Cosmochimica Acta,* 94**,** 22-37.

STORDAL, M. C. & WASSERBURG, G. J. 1986. Neodymium isotopic study of Baffin Bay water: sources of REE from very old terranes. *Earth and Planetary Science Letters,* 77.

STUMPF, R., FRANK, M., SCHÖNFELD, J. & HALEY, B. A. 2010. Late Quaternary variability of Mediterranean Outflow Water from radiogenic Nd and Pb isotopes. *Quaternary Science Reviews,* 29.

TACHIKAWA, K., ARSOUZE, T., BAYON, G., BORY, A., COLIN, C., DUTAY, J.-C., FRANK, N., GIRAUD, X., GOURLAN, A. T., JEANDEL, C., LACAN, F.,

MEYNADIER, L., MONTAGNA, P., PIOTROWSKI, A. M., PLANCHEREL, Y., PUCÉAT, E., ROY-BARMAN, M. & WAELBROECK, C. 2017. The large-scale evolution of neodymium isotopic composition in the global modern and Holocene ocean revealed from seawater and archive data. *Chemical Geology,* 457**,** 131-148.

TACHIKAWA, K., ATHIAS, V. & JEANDEL, C. 2003. Neodymium budget in the modern ocean and paleo-oceanographic implications. *Journal of Geophysical Research,* 108.

TAYLOR, S. & MCLENNAN, S. 1985. The continental crust: Its evolution and composition. *Lon on: Blackwell*.

THOMAS, D. J., KORTY, R., HUBER, M., SCHUBERT, J. A. & HAINES, B. 2014. Nd isotopic structure of the Pacific Ocean 70–30 Ma and numerical evidence for vigorous ocean circulation and ocean heat transport in a greenhouse world. *Paleoceanography,* 29**,** 454-469.

TOYODA, K. & TOKONAMI, M. 1990. Diffusion of rare-earth elements in fish teeth from deep-sea sediments. *Nature,* 345**,** 607.

VAN DE FLIERDT, T., GRIFFITHS, A. M., LAMBELET, M., LITTLE, S. H., STICHEL, T. & WILSON, D. J. 2016. Neodymium in the oceans: a global database, a regional comparison and implications for palaeoceanographic research. *Philosophical Transactions of the Royal Society A: Mathematical, Physical and Engineering Sciences,* 374.

VAN DE FLIERDT, T., ROBINSON, L. F. & ADKINS, J. F. 2010. Deep-sea coral aragonite as a recorder for the neodymium isotopic composition of seawater. *Geochimica et Cosmochimica Acta,* 74.

VAN DE FLIERDT, T., ROBINSON, L. F., ADKINS, J. F., HEMMING, S. R. & GOLDSTEIN, S. L. 2006. Temporal stability of the neodymium isotope signature of the Holocene to glacial North Atlantic. *Paleoceanography,* 21.

VANCE, D., SCRIVNER, A. E., BENEY, P., STAUBWASSER, M., HENDERSON, G. M. & SLOWEY, N. C. 2004. The use of foraminifera as a record of the past neodymium isotope composition of seawater. *Paleoceanography,* 19**,** n/a-n/a.

VON BREYMANN, M. T., EMEIS, K.-C. & SUESS, E. 1992. Water depth and diagenetic constraints on the use of barium as a palaeoproductivity indicator. *Geological Society, London, Special Publications,* 64**,** 273-284.

WILSON, D. J., PIOTROWSKI, A. M., GALY, A. & CLEGG, J. A. 2013. Reactivity of neodymium carriers in deep sea sediments: Implications for boundary exchange and paleoceanography. *Geochimica et Cosmochimica Acta,* 109.

WILSON, D. J., PIOTROWSKI, A. M., GALY, A. & MCCAVE, N. I. 2012. A boundary exchange influence on deglacial neodymium isotope records from the deep western Indian Ocean. *Earth and Planetary Science Letters,* 341**,** 35-47.

WINCKLER, G., ANDERSON, R. F., FLEISHER, M. Q., MCGEE, D. & MAHOWALD, N. 2008. Covariant glacial-interglacial dust fluxes in the equatorial Pacific and Antarctica. *Science (New York, N.Y.),* 320**,** 93-96.

WINCKLER, G., ANDERSON, R. F., JACCARD, S. L. & MARCANTONIO, F. 2016. Ocean dynamics, not dust, have controlled equatorial Pacific productivity over the past 500,000 years. *Proceedings of the National Academy of Sciences,* 113**,** 6119-6124.

WRIGHT, J., SEYMOUR, R. S. & SHAW, H. F. 1984. REE and Nd isotopes in conodont apatite: variations with geological age and depositional environment. *Conodont Biofacies and Provincialism,* 196**,** 325-340.

XIE, R. C. & MARCANTONIO, F. 2012. Deglacial dust provenance changes in the Eastern Equatorial Pacific and implications for ITCZ movement. *Earth and Planetary Science Letters.*

ZHANG, L., ALGEO, T. J., CAO, L., ZHAO, L., CHEN, Z.-Q. & LI, Z. 2016. Diagenetic uptake of rare earth elements by conodont apatite. *Palaeogeography, Palaeoclimatology, Palaeoecology,* 458**,** 176-197.

ZIEGLER, C. L., MURRAY, R. W., HOVAN, S. A. & REA, D. K. 2007. Resolving eolian, volcanogenic, and authigenic components in pelagic sediment from the Pacific Ocean. *Earth and Planetary Science Letters,* 254**,** 416-432.

ZIMMERMANN, B., PORCELLI, D., FRANK, M., RICKLI, J., LEE, D.-C. & HALLIDAY, A. N. 2009. The hafnium isotope composition of Pacific Ocean water. *Geochimica et Cosmochimica Acta,* 73**,** 91-101.

ZWENG, M. M., REAGAN, J. R., ANTONOV, J. I., LOCARNINI, R. A., MISHONOV, A. V., BOYER, T. P., GARCIA, H. E., BARANOVA, O. K., JOHNSON, D. R., SEIDOV, D. & BIDDLE, M. M. 2013. World Ocean Atlas 2013, Volume 2: Salinity. *In:* LEVITUS, S. & MISHONOV, A. (eds.) *NOAA Atlas NESDIS.*

5. CONCLUSIONS

This work has demonstrated that Nd and Pb isotopes in the operationally defined detrital fraction of marine sediments in the CEP are sensitive to changes in the ITCZ position. The Line Islands sites studied over the prescribed time interval (Section 2 and 3) received their dust signature from either the Chinese loess or South American volcanic regions. The South American sources show considerable heterogeneity divided into at least three regions (South Central Volcanic Zone, North Central Volcanic Zone, South Volcanic Zone). We do not find an Australian or North African signal at these sites across the last two glacial terminations.

During both of the last two deglaciations (0-30 kyr and 110-150kyrs), the dominant dust source to site 37BB is Asian loess. The equatorial core (17PC) predominantly received dust from South American sources, with the exception of the deglacial migration of the ITCZ to south of the equator, when 17PC receives Asian loess dust. The three middle cores (31BB, 28BB and 20BB) receive a mixed South American and Asian loess signal. We have found that during the last deglacial period the ITCZ migrated by between 2.5° and 7° southward from its LGM position to its modern position. During the penultimate deglaciation, the ITCZ moved by at least 7°, migrating farthest south during Heinrich Stadial 11.

In our examination of the neodymium isotope ratios of fish debris throughout the last 125 kyr, we found several periods of rapid radiogenic Nd enrichment, which we attributed to changes in the non-conservative behavior of Nd in the pore waters. We examined other possible explanations for the enrichment event, and we concluded that there had not been significant changes in water mass endmembers or endmember mixing and that particulate flux and reversible particle scavenging were not satisfying explanations for all events observed. We found

the most correlation between high authigenic uranium in EEP pore waters and enriched fish debris Nd. Therefore, we argue that under certain conditions the ε_{Nd} changes in authigenic Nd archives reflect changes in pore water oxygenation, and they can be used as a record of reduced ventilation rates in the Southern Ocean.

APPENDIX A

Supplementary information for section 2: Constraints on the Magnitude of the Deglacial Migration of the ITCZ in the Central Equatorial Pacific Ocean.

Table A1: Radiogenic Isotope data for Cores MGL1208-17PC, MGL1208-31BB, and MGL1208-37BB.

Core	Depth (cm)	lat (N)	long (E)	Age (years)	Nd IC	Std error	ƐNd	206/204	Std error	207/204	Std error	208/204	Std error
MGL1208-17PC	0	0.48	-161.63	3734	0.51258312	4.23E-05	-1.07	18.71	0.006	15.61	0.005	38.74	0.014
MGL1208-17PC	4	0.48	-161.63	5017	0.5125	4.21E-05	-3.09						
MGL1208-17PC	8	0.48	-161.63	6301				18.80	0.012	15.69	0.010	38.79	0.026
MGL1208-17PC	12	0.48	-161.63	7584	0.5124	2.33E-05	-4.34	18.65	0.015	15.54	0.013	38.54	0.031
MGL1208-17PC	16	0.48	-161.63	8867	0.5124	2.98E-06	-3.88						
MGL1208-17PC	20	0.48	-161.63	10150				18.73	0.017	15.64	0.015	38.82	0.038
MGL1208-17PC	24	0.48	-161.63	11434	0.5123	3.23E-05	-6.78						
MGL1208-17PC	28	0.48	-161.63	12717	0.5124	4.80E-06	-4.90						
MGL1208-17PC	32	0.48	-161.63	14000	0.5124	4.98E-06	-4.52						
MGL1208-17PC	36	0.48	-161.63	16727	0.5124	2.98E-06	-4.90	18.65	0.023	15.58	0.019	38.62	0.048
MGL1208-17PC	40	0.48	-161.63	18091	0.5123	3.00E-06	-5.89						
MGL1208-17PC	44	0.48	-161.63	19455	0.5123	4.45E-06	-5.77						
MGL1208-17PC	48	0.48	-161.63	20818	0.51235123	2.20E-06	-5.59	18.79	0.002	15.65	0.002	38.83	0.005
MGL1208-17PC	52	0.48	-161.63	22182	0.512441987	3.10E-06	-3.82	18.76	0.001			38.70	0.004
MGL1208-17PC	56	0.48	-161.63	23545	0.51238066	4.31E-06	-5.02						
MGL1208-17PC	60	0.48	-161.63	24909	0.512384541	1.62E-05	-4.94	18.83	0.001	15.66	0.001	38.96	0.004
MGL1208-17PC	64	0.48	-161.63	26273	0.51238812	2.75E-06	-4.87						
MGL1208-17PC	68	0.48	-161.63	27636	0.51240382	2.28E-06	-4.57						
MGL1208-17PC	72	0.48	-161.63	29000	0.51233883	1.55E-05	-5.84						
MGL1208-17PC	76	0.48	-161.63	29000	0.512399401	3.09E-05	-4.65						
MGL1208-17PC	80	0.48	-161.63	30273	0.51250172	1.17E-05	-2.66						
MGL1208-18GC	0	0.59	-156.66	3167				18.69	0.003	15.69	0.002	38.80	0.012
MGL1208-18GC	20	0.59	-156.66	6825				18.69	0.002	15.65	0.001	38.72	0.009
MGL1208-18GC	30	0.59	-156.66	9098				18.69	0.011	15.68	0.008	38.94	0.048
MGL1208-18GC	35	0.59	-156.66	9770				18.71	0.003	15.64	0.002	38.71	0.011
MGL1208-18GC	50	0.59	-156.66	11603				18.80	0.003	15.69	0.002	38.89	0.013
MGL1208-18GC	55	0.59	-156.66	13828				18.83	0.001	15.65	0.001	38.86	0.003
MGL1208-31BB	0	4.68	-160.05	12689	0.5124	1.62E-05	-5.45	18.86	0.014	15.67	0.011	39.04	0.028
MGL1208-31BB	5	4.68	-160.05	7231	0.5123	2.14E-05	-7.14	18.73	0.010	15.66	0.008	38.81	0.021
MGL1208-31BB	10	4.68	-160.05	5613	0.5123	1.26E-05	-5.91	18.80	0.017	15.65	0.015	38.91	0.036
MGL1208-31BB	15	4.68	-160.05	7409	0.5123	1.61E-05	-5.71	18.04	0.004	15.59	0.003	37.87	0.008
MGL1208-31BB	20	4.68	-160.05	8534	0.5123	1.55E-05	-5.81	18.27	0.014	15.50	0.012	38.11	0.029
MGL1208-31BB	25	4.68	-160.05	9658				18.53	0.003	15.61	0.003	38.51	0.009
MGL1208-31BB	30	4.68	-160.05	10782	0.5123	1.03E-05	-7.52						
MGL1208-31BB	35	4.68	-160.05	11906	0.5123	1.71E-05	-7.09	18.05	0.001	15.59	0.001	37.86	0.002
MGL1208-31BB	40	4.68	-160.05	13030				17.99	0.001	15.60	0.001	37.81	0.002
MGL1208-31BB	45	4.68	-160.05	14207				18.53	0.009	15.49	0.007	38.46	0.017
MGL1208-31BB	50	4.68	-160.05	15383				18.73	0.002	15.65	0.002	38.85	0.005
MGL1208-31BB	55	4.68	-160.05	16560	0.5122	1.82E-05	-9.13						
MGL1208-31BB	60	4.68	-160.05	17736	0.5122	7.87E-06	-7.95	18.89	0.019	15.69	0.016	39.08	0.040
MGL1208-31BB	65	4.68	-160.05	18913	0.5122	1.69E-05	-8.58						
MGL1208-31BB	70	4.68	-160.05	20089	0.5120	9.34E-06	-11.93						
MGL1208-31BB	75	4.68	-160.05	21464	0.5122	2.66E-05	-8.37						
MGL1208-31BB	80	4.68	-160.05	22971	0.5122	9.07E-06	-7.90	18.91	0.004	15.70	0.003	39.11	0.009
MGL1208-31BB	85	4.68	-160.05	24479	0.5122	3.31E-06	-8.63						
MGL1208-31BB	90	4.68	-160.05	25986	0.5123	9.82E-05	-7.07	18.92	0.005	15.71	0.004	39.16	0.010
MGL1208-31BB	95	4.68	-160.05	27493	0.5122	2.65E-05	-8.29						
MGL1208-37BB	0	7.04	-161.63	6619	0.5123	1.55E-05	-6.59						
MGL1208-37BB	4	7.04	-161.63	8464	0.512267	6.30E-06	-7.23						
MGL1208-37BB	8	7.04	-161.63	10310	0.5122	7.81E-05	-11.76	18.77	0.006	15.68	0.005	38.99	0.014
MGL1208-37BB	12	7.04	-161.63	12155	0.512167	5.72E-06	-9.20						
MGL1208-37BB	16	7.04	-161.63	14000	0.5122	2.20E-06	-8.89	18.81	0.003	15.66	0.002	39.03	0.006
MGL1208-37BB	20	7.04	-161.63	16400	0.512117	4.36E-06	-10.16	18.83	0.003	15.69	0.002	39.09	0.006
MGL1208-37BB	23.5	7.04	-161.63	18500	0.512142	2.50E-06	-9.68	18.80	0.018	15.73	0.014	39.17	0.037
MGL1208-37BB	32	7.04	-161.63	23600	0.5121	3.17E-06	-8.73						
MGL1208-37BB	36	7.04	-161.63	26000				18.93	0.008	15.70	0.007	39.17	0.017
MGL1208-37BB	40	7.04	-161.63	28400	0.5122	7.52E-05	-11.35	18.92	0.004	15.64	0.003	39.11	0.008

a. Depth age relationship from Lynch-Stieglitz et al. (2015).

Section S2. The Equatorial Composite Core

Samples from core MGL1208-18GC (Fig. 1) at 0.59° N, were also analyzed for Pb isotope ratios. A comparison of the $^{206}Pb/^{204}Pb$ ratios for Holocene samples from 18GC and 17PC, both equatorial cores, shows that both cores record virtually identical dust Pb isotope characteristics (Figure S1). Additionally, Pb isotopes for both equatorial cores record Pb isotope ratios that are distinctly different from either core 37BB or 31BB (Fig. 2). Moreover, this comparison gives us an idea of the reproducibility of the analyses. The small detrital contents of CEP sediments (0.02-0.5% of the total sample) meant that we required large sample sizes (at least 6 grams of dried bulk sediment) to process for isotope analysis by TIMS, which limited our ability to duplicate sample analyses. Importantly, however, due to the strong consistency between the Pb isotope analyses for the two equator cores analyzed (Fig. S1), Figures 2 and 3 present the equatorial Pb data as a single composite.

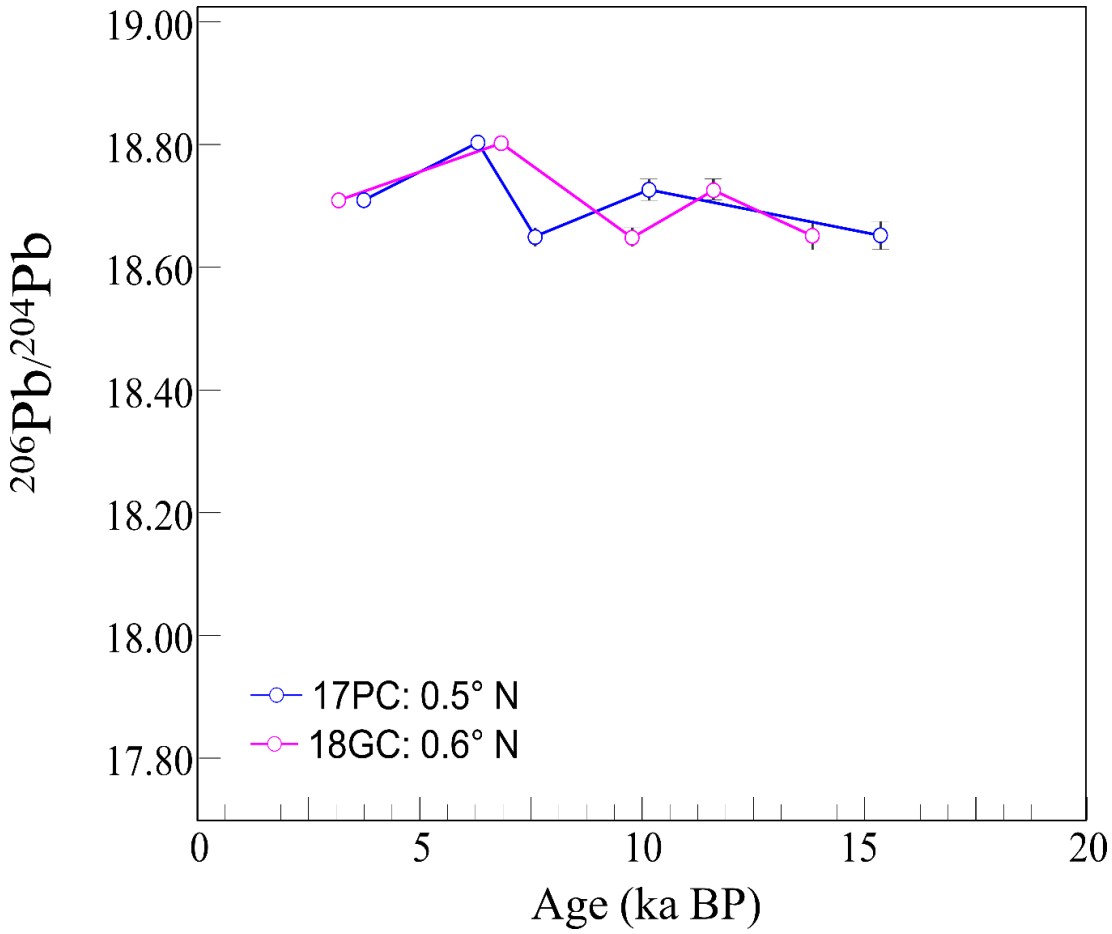

Figure A1. $^{206}Pb/^{204}Pb$ over time for core 18GC (pink), and 17PC (blue). The error bars represent standard errors.

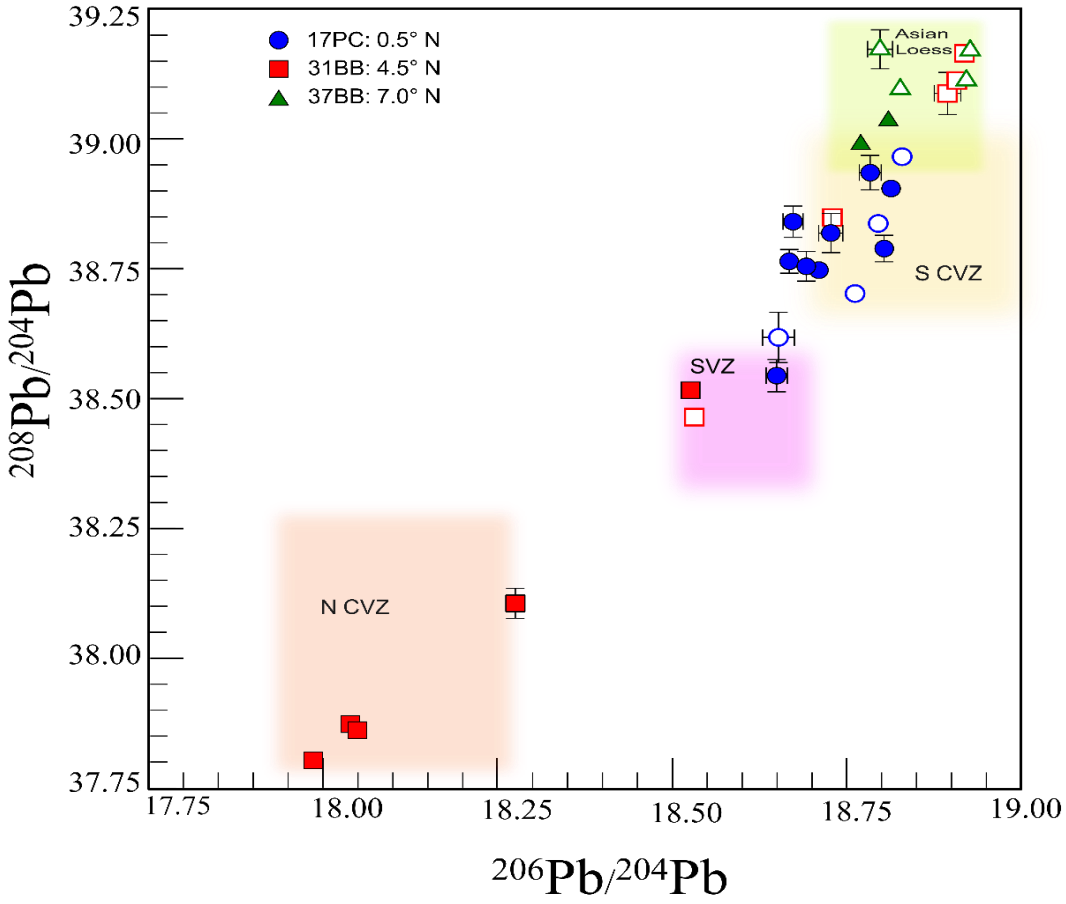

Figure A2. 208Pb/206Pb versus 206Pb/204Pb all three sites (17PC--0.5° N, blue circles; 31BB--4.5° N, red squares; and 37BB--7° N, green triangles). The error bars represent standard errors. Filled shapes are Holocene samples, and open shapes are glacial samples. Possible dust sources are marked by the shaded areas. The South Central Volcanic Zone (S-CVZ) and the North Central Volcanic Zone (N-CVZ) Pb ranges are from Mamani et al. (2008), and references therein. For the South Volcanic Zone (SVZ) the Pb isotope range is based on Pichat et al. (2014) and references therein. The Pb isotope ranges for Asian loess are from Sun and Zhu (2010).

References

LYNCH-STIEGLITZ, J., POLISSAR, P. J., JACOBEL, A. W., HOVAN, S. A., POCKALNY, R. A., LYLE, M., MURRAY, R. W., RAVELO, C. A., BOVA, S. C., DUNLEA, A. G., FORD, H. L., HERTZBERG, J. E., WERTMAN, C. A., MALONEY, A. E., SHACKFORD, J. K., WEJNERT, K. & XIE, R. C. 2015. Glacial-interglacial changes in central tropical Pacific surface seawater property gradients. *Paleoceanography*, 30**,** 423-438.

MAMANI, M., TASSARA, A. & WÖRNER, G. 2008. Composition and structural control of crustal domains in the central Andes. *Geochemistry, Geophysics, Geosystems,* 9.

PICHAT, S., ABOUCHAMI, W. & GALER, S. 2014. Lead isotopes in the Eastern Equatorial Pacific record Quaternary migration of the South Westerlies. *Earth and Planetary Science Letters,* 388.

SUN, J. & ZHU, X. 2010. Temporal variations in Pb isotopes and trace element concentrations within Chinese eolian deposits during the past 8Ma: Implications for provenance change. *Earth and Planetary Science Letters*.

APPENDIX B

Supplementary information for section 3: The Penultimate Glacial Termination and Large Migrations of the Pacific Intertropical Convergence Zone

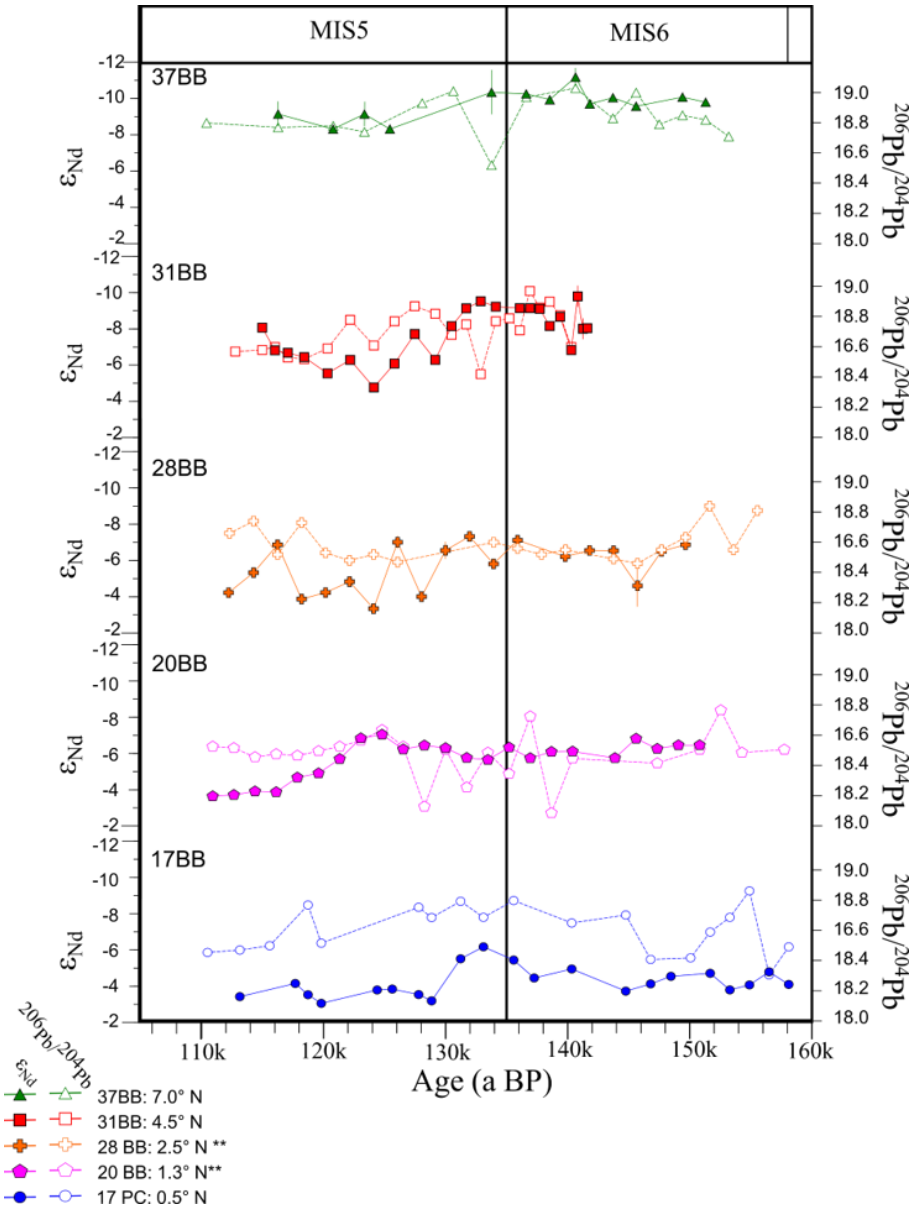

Figure B1. $^{206}Pb/^{204}Pb$ amd εNd over time for all sites (17PC--0.5° N, blue circles; 20BB--1.3° N, pink pentagons; 28BB--3.0 ° N, orange crosses; 31BB--4.5° N, red squares;

and 37BB--7° N, green triangles). The error bars represent standard errors. Filled symbols are ε_{Nd} values, and open symbols are $^{206}Pb/^{204}Pb$ ratios.

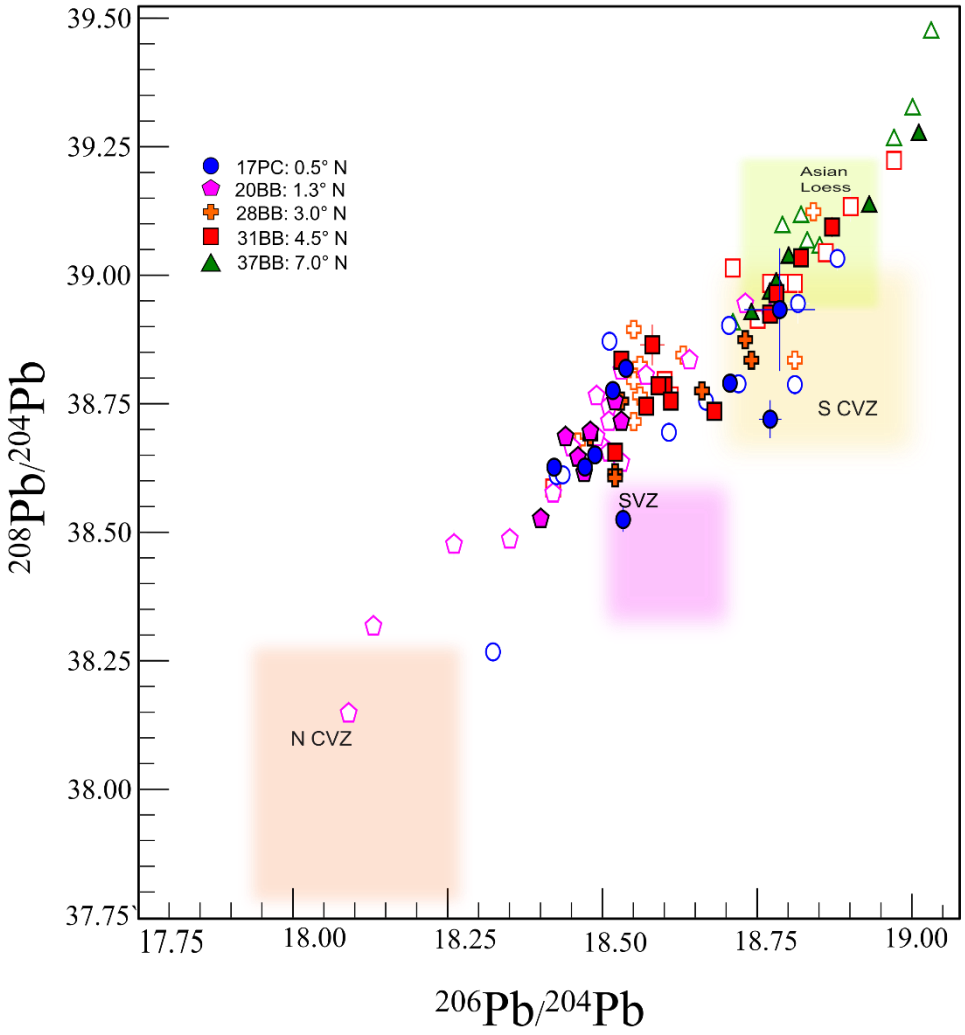

Figure B2. $^{208}Pb/^{206}Pb$ versus $^{206}Pb/^{204}Pb$ all five sites (17PC--0.5° N, blue circles; 20BB--1.3° N, pink pentagons; 28BB--3.0 ° N, orange crosses; 31BB--4.5° N, red squares; and 37BB--7° N, green triangles). The error bars represent standard errors. Filled symbols are interglacial samples (MIS 5), and open symbols are glacial samples (MIS 6). Possible dust sources are marked by the shaded areas. The South Central Volcanic Zone (S-CVZ) and North Central Volcanic Zone (N-CVZ) Pb and Nd ranges from Mamani et al. (2010), and references therein; the South Volcanic Zone (SVZ) Pb isotope range is based on Pichat et al. (2014) and references therein; Pb isotope ranges for Asian loess from (Sun and Zhu, 2010), and references therein.

Table B1. Radiogenic isotopes for core 17PC

Cruise	Core	Water Depth (r	Latitude (N)	Longitude (W)						
ML1208	17PC	2926	0.48	-156.45						
Depth (cm)	Age (ka)	Nd IC	Std error	ENd	206/204	Std error	207/204	Std error	208/204	Std error
288	110491				18.4713	0.0008	15.6586	0.0007	38.631	0.002
292	113138	0.51245509	1.83E-06	-3.57	18.4875	0.0004	15.6628	0.0003	38.655	0.001
296	115586				18.516	0.002	15.700	0.001	38.781	0.004
300	117681	0.51242173	7.87E-06	-4.22						
302	118725	0.51245355	1.99E-06	-3.60	18.7857	0.06	15.68	0.05	38.939	0.120
304	119815	0.51243464	4.44E-06	-3.97	18.53	0.01	15.63	0.01	38.53	0.024
312	124394	0.51244014	2.40E-06	-3.86						
316	125632	0.51243763	6.90E-06	-3.91						
324	127795	0.51245310	2.11E-06	-3.61	18.77	0.02	15.66	0.02	38.72	0.037
328	128856	0.51244402	5.87E-06	-3.78	18.705	0.001	15.6623	0.0009	38.795	0.002
336	131234	0.51235193	1.64E-06	-5.58	18.810	0.002	15.614	0.002	38.792	0.004
340	133105	0.51231261	3.81E-06	-6.35	18.706	0.003	15.684	0.002	38.795	0.006
344	135583	0.51235554	7.43E-06	-5.51	18.82	0.02	15.70	0.02	38.95	0.039
348	137263	0.51240625	3.64E-06	-4.52						
356	140343	0.51238206	5.98E-06	-4.99	18.667	0.001	15.667	0.001	38.760	0.003
364	144771	0.51241323	5.17E-06	-4.38	18.719	0.002	15.665	0.002	38.794	0.005
368	146807	0.51242297	2.49E-06	-4.19	18.426	0.001	15.668	0.002	38.614	0.005
372	148474	0.51240156	7.51E-06	-4.61						
376	150082				18.4354	0.0008	15.6635	0.0008	38.616	0.002
380	151691	0.51239019	3.51E-06	-4.83	18.607	0.001	15.662	0.001	38.699	0.003
384	153300	0.51239818	4.95E-06	-4.68	18.704	0.005	15.707	0.004	38.91	0.012
388	154909	0.51242585	7.13E-06	-4.14	18.88	0.01	15.704	0.009	39.039	0.024
392	156518	0.51238895	6.10E-06	-4.86	18.3230	0.0008	15.6057	0.0009	38.270	0.003
396	158126	0.51242445	1.96E-06	-4.17	18.511	0.001	15.737	0.001	38.877	0.004

Table B2. Radiogenic isotopes for core 20BB.

Cruise	Core	Water Depth (r	Latitude (N)	Longitude (W)								
ML1208	20BB	2850	1.27	-157.26								
Depth (cm)	Age (ka)	Nd IC	Std error	εNd	206Pb/204Pb	Std error	207Pb/204Pb	Std error	208Pb/204Pb	Std error	^{230}Th-derived MAR (g cm^{-2} kyr^{-1})	^{230}Th-derived ^{232}Th MAR (μg cm^{-2} kyr^{-1})
290	119878				18.442	0.001	15.688	0.001	38.693	0.003	1.23	0.36
295	122279	0.5124251	3.96E-06	-5.33	18.399	0.001	15.6429	0.0009	38.529	0.002		
300	124043	0.5124495	4.30E-06	-4.15	18.5269	0.0006	15.6796	0.0007	38.716	0.002	1.26	0.40
305	125532	0.5124458	2.62E-06	-3.68	18.519	0.001	15.6992	0.001	38.756	0.005	1.29	0.36
310	127021	0.5124358	3.32E-06	-3.75	18.456	0.001	15.6728	0.0009	38.652	0.003	1.12	0.27
315	128511	0.5124379	3.69E-06	-3.94	18.484	0.001	15.688	0.001	38.698	0.004		
320	130000	0.5123967	8.30E-06	-3.90	18.471	0.001	15.659	0.001	38.616	0.003	1.55	0.41
325	131489	0.5123848	2.22E-06	-4.94	18.5003	0.0005	15.6693	0.0005	38.671	0.002	1.92	0.48
330	132979	0.5123441	3.28E-06	-5.73	18.5286	0.0007	15.6409	0.0007	38.639	0.002	1.79	0.41
335	134468	0.5122856	1.22E-05	-6.87	18.5738	0.0008	15.6910	0.0008	38.805	0.002	2.15	0.59
340	135957	0.5122753	2.33E-06	-7.08	18.6405	0.0007	15.6834	0.0007	38.839	0.002	1.76	0.53
345	137447	0.5123168	5.65E-06	-6.27	18.531	0.002	15.708	0.002	38.818	0.005	1.83	0.62
350	138936				18.126	0.001	15.7091	0.0009	38.323	0.002	3.65	1.01
355	140426	0.5123059	8.16E-06	-6.48	18.513	0.003	15.697	0.002	38.750	0.006	1.21	0.41
360	141915	0.5123135	2.35E-06	-6.33	18.26	0.01	15.72	0.01	38.48	0.03	1.47	0.58
365	143404	0.5123411	1.87E-06	-5.79	18.494	0.001	15.705	0.001	38.771	0.003	1.25	0.44
370	144894	0.5123466	5.86E-06	-5.68	18.3462	0.0009	15.662	0.001	38.485	0.003	1.32	0.31
375	146383	0.5123116	4.77E-06	-6.37	18.7317	0.0007	15.6842	0.0006	38.951	0.002	1.90	0.52
380	147872	0.5123431	2.44E-06	-5.75	18.090	0.004	15.654	0.003	38.146	0.009	1.65	0.24
385	149362	0.5123241	3.21E-06	-6.12	18.4547	0.0006	15.6761	0.0006	38.667	0.002	1.95	0.02
390	150851	0.5123230	3.90E-06	-6.14							1.80	-0.23
395	152340										1.80	-0.39
400	153830	0.5123416	4.55E-06	-5.78							1.72	-0.54
405	155319	0.5122867	4.80E-06	-6.85	18.4212	0.0006	15.65	0.0006	38.58	0.00141		
410	156809	0.5123154	4.66E-06	-6.29							1.87	-0.43
415	158298	0.5123054	2.63E-06	-6.49	18.5125	0.0006	15.65	0.0007	38.66	0.00194	1.80	-0.67
420	159787				18.772	0.005	15.68	0.004	38.93	0.00970	1.43	-0.12
430	162766										1.69	1.07
435	164255										3.32	2.32
440	165745										7.56	3.04

Table B3. Radiogenic isotopes for core 28BB.

Cruise	Core	Water Depth (r	Latitude (N)	Longitude (W)								
ML1208	28BB	3153	2.97	-159.20								
Depth (cm)	Age (ka)	Nd IC	Std error	εNd	206Pb/204Pb	Std error	207Pb/204Pb	Std error	208Pb/204Pb	Std error	^{230}Th-derived MAR (g cm^{-2} kyr^{-1})	^{230}Th-derived ^{232}Th MAR (μg cm^{-2} kyr^{-1})
285	115470	0.5124215	3.47E-06	-4.22	18.660	0.001	15.680	0.001	38.784	0.002	0.234	0.29
290	117672	0.5123649	2.11E-06	-5.33	18.737	0.004	15.652	0.003	38.836	0.008	0.209	0.32
295	119873	0.5122860	2.55E-06	-6.87	18.5217	0.0008	15.6436	0.0008	38.620	0.002	0.178	0.32
300	122075	0.5124397	2.79E-06	-3.87	18.731	0.003	15.687	0.002	38.885	0.006	0.203	0.46
305	124800	0.5124213	3.10E-06	-4.23	18.5268	0.0007	15.6947	0.0007	38.760	0.002	0.166	0.32
310	126800	0.5123905	3.34E-06	-4.83	18.485	0.006	15.678	0.005	38.69	0.013		
315	128800	0.5124668	3.36E-06	-3.34	18.5215	0.0008	15.6547	0.0008	38.610	0.002	0.166	0.36
320	130800	0.5122789	1.8E-05	-7.01	18.4679	0.0009	15.6567	0.0010	38.629	0.003	0.142	0.27
325	132800	0.5124329	2.90E-06	-4.00							0.237	0.36
330	134800	0.5123013	2.39E-05	-6.57	18.561	0.001	15.701	0.001	38.835	0.004		
335	136800	0.5122625	2.07E-06	-7.32								
340	138800	0.5123403	3.44E-06	-5.81	18.6010	0.0006	15.6715	0.0007	38.787	0.002	0.370	0.31
345	140800	0.5122731	2.47E-06	-7.12	18.558	0.003	15.677	0.002	38.770	0.005	0.350	0.41
350	142800				18.5228	0.0006	15.6885	0.0006	38.764	0.002	0.328	0.65
355	144800	0.5123196	4.46E-06	-6.21	18.5480	0.0008	15.7283	0.0008	38.895	0.003		
360	146800	0.5123022	2.67E-06	-6.55							0.137	0.36
365	148800	0.5123029	2.31E-06	-6.54	18.4863	0.0005	15.6702	0.0004	38.676	0.001	0.338	1.10
370	150800			-4.60	18.4648	0.0007	15.6771	0.0007	38.682	0.002	0.363	1.23
375	152800	0.5123045	3.24E-06	-6.51	18.5490	0.0008	15.6925	0.0009	38.803	0.003		
380	154800	0.5122859	2.17E-06	-6.87	18.628	0.001	15.6914	0.0008	38.855	0.002	0.348	0.73
385	156800				18.844	0.007	15.729	0.006	39.13	0.016	0.363	0.65
390	158800				18.554	0.001	15.671	0.001	38.723	0.004	0.370	0.50
395	160800	0.5123057	3.12E-06	-6.48	18.809	0.002	15.664	0.002	38.845	0.005	0.384	0.43

Table B4. Radiogenic isotopes for core 31BB

Cruise	Core	Water Depth (m)	Latitude (N)	Longitude (W)						
ML1208	31BB	2857	4.68	-160.05						
Depth (cm)	Age (ka)	Nd IC	Std error	εNd	206Pb/204Pb	Std error	207Pb/204Pb	Std error	208Pb/204Pb	Std error
350	112766				18.5711	0.0007	15.6668	0.0007	38.754	0.002
360	114981	0.5122245	4.71E-06	-8.07	18.58	0.02	15.73	0.02	38.87	0.04
365	116015	0.5122886	3.46E-06	-6.82	18.598	0.007	15.677	0.004	38.79	0.01
370	117069	0.5122955	7.24E-06	-6.68	18.532	0.001	15.713	0.001	38.841	0.003
375	118415	0.5123080	4.05E-06	-6.44	18.5194	0.0008	15.6592	0.0008	38.661	0.002
380	120324	0.5123537	7.46E-06	-5.55	18.5856	0.0007	15.6872	0.0006	38.790	0.002
385	122183	0.5123155	4.98E-06	-6.29	18.783	0.002	15.672	0.002	38.973	0.005
390	124121			-4.77	18.610	0.002	15.671	0.002	38.764	0.004
395	125817	0.5123260	4.06E-06	-6.09	18.771	0.004	15.682	0.003	38.935	0.007
400	127477	0.5122424	4.31E-06	-7.72	18.869	0.009	15.701	0.007	39.10	0.02
405	129154	0.5123154	2.62E-06	-6.29	18.824	0.002	15.713	0.002	39.038	0.006
410	130492	0.5122203	4.56E-06	-8.15	18.683	0.002	15.654	0.001	38.735	0.004
415	131692	0.5121700	5.00E-06	-9.13	18.7535	0.0005	15.6650	0.0005	38.917	0.001
420	132884	0.5121497	3.60E-06	-9.52	18.417	0.002	15.664	0.001	38.590	0.003
425	134123	0.5121654	4.65E-06	-9.22	18.7741	0.0004	15.6722	0.0003	38.9938	0.0008
430	135234				18.7948	0.0009	15.6661	0.0008	38.993	0.002
435	136086	0.5121694	3.36E-06	-9.14	18.7102	0.0006	15.7065	0.0006	39.018	0.002
440	136906	0.5121696	6.63E-06	-9.14	18.972	0.001	15.716	0.001	39.225	0.003
445	137719	0.5121714	5.02E-06	-9.10	18.857	0.001	15.673	0.001	39.048	0.004
450	138539	0.5122200	5.36E-06	-8.15	18.90	0.01	15.69	0.01	39.14	0.03
455	139398	0.5121939	2.75E-06	-8.66	18.807	0.001	15.676	0.001	38.989	0.003
460	140310	0.5122879	1.57E-05	-6.83	18.6048	0.0009	15.6772	0.0008	38.796	0.002
465	140831	0.5121362	3.09E-05	-9.79						
470	141256	0.5122276	3.02E-05	-8.01						
475	141626	0.5122260	7.93E-06	-8.04	18.607	0.002	15.673	0.002	38.773	0.005

Table B5. Radiogenic isotopes for core 37BB.

Cruise	Core	Water Depth (m)	Latitude (N)	Longitude (W)						
ML1208	37BB	2798	7.04	-161.63						
Depth (cm)	Age (ka)	Nd IC	Std error	εNd	206Pb/204Pb	Std error	207Pb/204Pb	Std error	208Pb/204Pb	Std error
133	110409				18.7999	0.0009	15.6807	0.0008	39.038	0.002
137	116276	0.5121689	3.49E-05	-9.15	18.7668	0.0009	15.672	0.001	38.965	0.003
141	120784	0.5122112	3.63E-06	-8.33	18.780	0.001	15.6812	0.0009	38.988	0.003
143	123357				18.7354	0.0009	15.6802	0.0008	38.933	0.002
149	128084				18.9303	0.0028	15.704	0.002	39.141	0.006
153	130639				19.0132	0.0015	15.708	0.001	39.278	0.003
157	133770	0.5121118	3.76E-06	-10.35	18.52	0.03	15.73	0.02	38.76	0.06
161	136610	0.5121284	1.70E-06	-10.26	18.9663	0.0007	15.6915	0.0007	39.265	0.002
165	138544	0.5120644	2.58E-05	-9.94						
169.5	140653	0.5120386	2.58E-05	-11.19	19.0344	0.0008	15.7728	0.0007	39.480	0.002
172	141824	0.5121403	1.94E-06	-9.71						
176	143720	0.5121235	2.29E-06	-10.04	18.8349	0.0006	15.6709	0.0007	39.073	0.002
180	145620	0.5121467	3.67E-06	-9.58	18.999	0.004	15.715	0.003	39.332	0.007
184	147520				18.7941	0.0004	15.7161	0.0004	39.0994	0.0009
188	149421	0.5121210	4.68E-06	-10.09	18.852	0.002	15.6567	0.0021	39.058	0.005
192	151321	0.5121355	1.80E-06	-9.80	18.8158	0.0005	15.6978	0.0005	39.117	0.002
196	153221				18.707	0.001	15.669	0.001	38.908	0.004

References

MAMANI, M., WÖRNER, G. & SEMPERE, T. 2010. Geochemical variations in igneous rocks of the Central Andean orocline (13 S to 18 S): tracing crustal thickening and magma generation through time and space. *Geological Society of America Bulletin,* 122.

PICHAT, S., ABOUCHAMI, W. & GALER, S. 2014. Lead isotopes in the Eastern Equatorial Pacific record Quaternary migration of the South Westerlies. *Earth and Planetary Science Letters,* 388.

SUN, J. & ZHU, X. 2010. Temporal variations in Pb isotopes and trace element concentrations within Chinese eolian deposits during the past 8Ma: Implications for provenance change. *Earth and Planetary Science Letters*.

APPENDIX C

Supplementary information for section 4: Neodymium isotope radiogenic enrichment in authigenic phases as a function of bottom water ventilation strength in the central equatorial Pacific Ocean.

Table C1. Barium and Barium flux through time. **a.** Age model based on Jacobel et al. (2017). **b.** Thorium data from Jacobel et al. (2016, 2017a).

Depth	Age[a]	Ba (ppm)	xsBa (ppm)[b]	xsBa flux	+-
0	5.0	546	541	0.80	0.06
8	6.5	558	554	0.81	0.06
16	8.1	532	528	0.84	0.06
24	10.7	571	565	0.86	0.06
32	12.8	492	480	0.46	0.03
40	16.4	317	310	0.59	0.04
48	19.0	448	439	0.73	0.05
56	21.8	403	394	0.66	0.05
64	26.6	405	396	0.70	0.05
72	30.1	396	388	0.71	0.05
80	34.4	305	298	0.61	0.04
88	38.8	329	322	0.66	0.05
96	42.3	376	368	0.65	0.05
104	46.4	311	304	0.64	0.04
112	48.0	311	305	0.63	0.04
120	49.3	330	324	0.66	0.05
128	50.5	344	338	0.68	0.05
136	51.7	354	347	0.65	0.05
144	53.0	392	386	0.79	0.05
152	54.3	416	410	0.86	0.06
160	56.3	381	370	0.45	0.03
168	60.0	360	351	0.68	0.05
176	62.5	444	435	0.76	0.05
184	65.2	381	371	0.53	0.04
192	71.1	355	349	0.57	0.04
200	77.5	434	428	0.67	0.05

Table C1. (continued)

Depth	Age[a]	Ba (ppm)	xsBa (ppm)[b]	xsBa flux	+-
208	81.7	507	502	0.87	0.06
216	84.1	487	480	0.73	0.05
224	86.8	442	436	0.74	0.05
232	90.0	421	414	0.66	0.05
240	93.6	394	388	0.59	0.04
248	96.1	536	531	0.84	0.06
256	98.5	496	491	0.82	0.06
264	102.5	326	321	0.50	0.04
272	105.3	474	469	0.78	0.05
280	107.0	233	227	0.37	0.03
288	110.0	418	412	0.69	0.05
296	115.6	416	410	0.58	0.04
316	125.6	667	662	1.07	0.07
372	148.5	384	376	0.68	0.05
400	180.0	364	364		

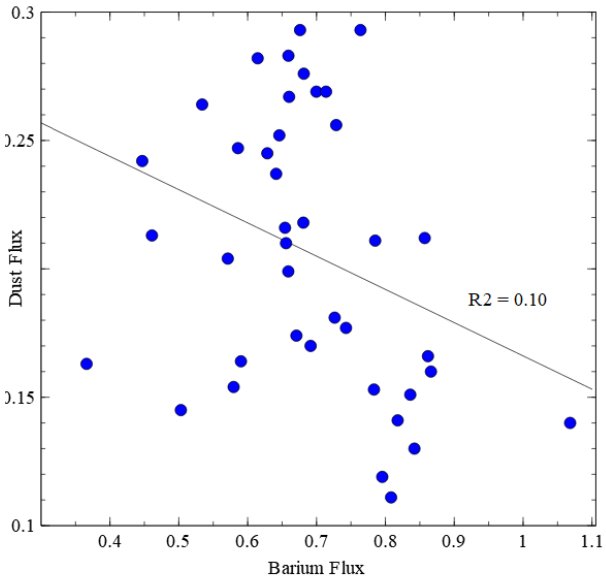

Figure C1. Barium versus Thorium dust flux.

Table C2. Core tops locations and water depths

Core	Latitude (°N)	Longitude (° E)	Water Depth (m)
MV1014-MC01F	5.82	274.27	1760
MV1014-MC06F	6.17	273.85	1257
MV1014-MC09F	0.69	274.69	2452
MV1014-MC16F	0.17	274.13	2846
MV1014-MC20F	-8.5	272.97	4407

References

JACOBEL, A. W., MCMANUS, J., ANDERSON, R. & WINCKLER, G. 2016. Large deglacial shifts of the Pacific Intertropical Convergence Zone. *Nature Communications,* 7.

JACOBEL, A. W., MCMANUS, J. F., ANDERSON, R. F. & WINCKLER, G. 2017. Climate-related response of dust flux to the central equatorial Pacific over the past 150 kyr. *Earth and Planetary Science Letters,* 457**,** 160-172.